
# Collective Strong Coupling of Cold Potassium Atoms in an Optical Ring Cavity

by

Robert Culver

A thesis submitted to
The University of Birmingham
for the degree of
DOCTOR OF PHILOSOPHY

Ultracold Atoms Group
School of Physics and Astronomy
College of Engineering and Physical Sciences
The University of Birmingham

February 2017

**Abstract**

This thesis describes an experiment which studies a cloud of magneto-optically trapped potassium-39 atoms inside an optical ring cavity. The potassium atoms are firstly cooled in a two-dimensional magneto-optical trap (MOT) and are then transferred into a three-dimensional MOT which overlaps with the cavity mode. In this thesis, the optimisation of the MOT systems and the characterisation and construction of the optical ring cavity are discussed.

After exploring these two systems independently, the two systems are then coupled together to provide an atom-cavity system, which exhibits collective strong coupling. The system is shown to exhibit normal-mode splitting, with a collective Rabi splitting of $G = 2\pi \cdot (6.25 \pm 0.50)$MHz, corresponding to $(4.7 \pm 0.6) \times 10^3$ atoms in the cavity. Whilst collective strong coupling has been achieved before in other experiments, we believe this is the first experiment to achieve this with potassium.

The next goal in the experiment is to control the group refractive index of the atoms inside the cavity. The modification of the group index using electromagnetically-induced transparency (EIT) on hot atoms inside a vapour cell has already been previously demonstrated by this experiment; and using the same laser system we aim to demonstrate EIT on the cold intra-cavity atoms as well. Gain mechanisms could also be used to create a ring laser with a controllable group index. These techniques could lead to a range of applications such as enhanced-sensitivity laser ring gyroscopes and active optical clocks.

# Contents

# List of Figures

# List of Tables

# CHAPTER 1

# Introduction

The question of how light and matter interact with one another has been fascinating physicists for some time, and since the discovery of the photon and the advent of quantum mechanics, physicists have gained considerable ground in finding answers to this question. In 1946, Purcell pointed out that the rate of spontaneous emission from an excited atom can be modified by placing the atom in a resonant cavity, due to the modification of the density of final states [1, 2]. This discovery gave birth to the field of cavity quantum electrodynamics [3, 4] which has since found a myriad of applications [5, 6, 7].

In 1963, Jaynes and Cummings [8] produced a theoretical description of a two-level atom interacting with a single mode of a cavity. This model (which will be discussed in detail later) showed that the atom and cavity exchange excitation coherently at a rate $g$. If this rate $g$ is fast compared to the rates of decoherence due to mirror losses $\kappa$ and spontaneous emission $\gamma$, then the atom-cavity system is dominated by the interaction [9]. This regime, where $g \gg \kappa, \gamma$ is known as the strong coupling regime. A few years later in 1968, Tavis and Cummings [10] provided a theoretical model for $N$ atoms interacting with the cavity, which showed that the single-atom coupling rate $g$ was increased to the $N$-atom coupling rate $g\sqrt{N}$, and hence strong coupling can also be achieved in the collective sense where $g\sqrt{N} \gg \kappa, \gamma$.

Achieving collective strong coupling with a cloud of cold potassium-39 atoms is the main focus of this thesis. The future goals of this experiment are to incorporate coherent control of the the refractive index of the intra-cavity atoms to produce a modified group velocity within the cavity to produce either fast or slow light [11]. A controllable intra-cavity group index could have a range of applications, such as active optical clocks [12, 13] and enhanced rotation sensors [14, 15] - where the ring cavity geometry is required. Slow light and fast light have been of interest to the scientific community for some time, even without the presence of a cavity, and this experiment has already demonstrated slow light using electromagnetically induced transparency [16, 17] outside of the cavity, using warm potassium atoms [18]. Since my departure from the laboratory, work is ongoing to establish electromagnetically-induced transparency on the cold atoms inside the cavity.

## Thesis Outline

This thesis presents an experiment which demonstrates collective strong coupling between potassium atoms and an optical ring cavity [19]. In Chapter 2, the physics of this atom-cavity interaction are described theoretically. Chapter 2 then ends by discussing the physics of group index and intra-cavity electromagnetically-induced transparency (EIT). Although this experiment has not yet demonstrated intra-cavity EIT, the topic is interesting and is necessary for understanding some of the experimental design considerations.

Chapters 3 and 4 focus mostly on the cold-atom aspects of this experiment. In Chapter 3, I start by briefly discussing the operational principles of magneto-optical trapping. This experiment uses a three-dimensional magneto-optical trap which is loaded by an atomic beam generated from a two-dimensional magneto-optical trap, and the aim of this chapter is to describe the laser system and vacuum system used to achieve this. Then, in Chapter 4, the laser cooling system is characterised and optimised.

The next part of this thesis consists of Chapters 5 and 6, which focus mostly on the (empty) optical cavity aspects of this experiment. In Chapter 5, I start by discussing the theory relevant to optical resonators, such as the theoretical transmission spectrum and mode structure. Chapter 5 continues with discussions of the physical realisation of the cavity, and ends with a description of the laser system used to probe and stabilise the cavity length. Chapter 6 then focuses on characterising this cavity.

Finally, in Chapter 7, collective strong coupling is demonstrated, and Chapter 8 gives an experimental outlook.

# CHAPTER 2

# Atoms and Cavities

The purpose of this chapter is to introduce the main physical concepts regarding the interaction of atoms and cavities. Firstly, we will look at the Jaynes-Cumming Hamiltonian and extend this to include losses. Then, the collective effects of $N$ atoms will be discussed.

After this, the group velocity and intra-cavity electromagnetically-induced transparency (EIT) will be discussed. Although this experiment does not yet exhibit intra-cavity EIT, a theoretical understanding of EIT is necessary for understanding some of the design considerations in this experiment. This theory will also be called upon in the experimental outlook in Chapter 8.

## 2.1 Interactions Between Cavities and Atoms

### 2.1.1 The Jaynes-Cummings Hamiltonian

When atoms are positioned inside the cavity mode, the atoms can absorb photons from the cavity mode, as well as emit photons into it. In this atom-cavity system, the atoms and cavity no longer act independently and are coupled. To understand this coupling, this section considers the Jaynes-Cummings model where a simple two-level atom with states $|g\rangle$ and $|e\rangle$ interacts with a single mode of the cavity in a closed system [8]. The Hamiltonian for this system takes the form,

$$H = H_A + H_C + H_I \,, \tag{2.1}$$

where $H_A$ and $H_C$ are the Hamiltonians for the bare atom and the empty cavity. $H_I$ is the interaction Hamiltonian, which describes how the atom and cavity are coupled. Firstly, if the atom's excited state $|e\rangle$ has energy $\hbar\omega_a$, then $H_A$ is given by,

$$H_A = \hbar\omega_a \sigma^+ \sigma^- \,, \tag{2.2}$$

where $\sigma^+ = |e\rangle\langle g|$ and $\sigma^- = |g\rangle\langle e|$ are the raising and lowering operators for the atomic state. $H_C$ for a cavity containing $n$ photons with energy $\hbar\omega_c$ will be

$$H_C = \hbar\omega_c \left( a^\dagger a + \frac{1}{2} \right), \tag{2.3}$$

where $a^\dagger |n\rangle = \sqrt{n+1}\,|n+1\rangle$ and $a\,|n\rangle = \sqrt{n}\,|n-1\rangle$ are the well-known raising and lowering operators for the Fock states [20]. The $\frac{\hbar\omega_c}{2}$ term is the zero-point energy and can be ignored. Finally, the interaction Hamiltonian $H_I$ is described by,

$$H_I = -\vec{d} \cdot \vec{E}(t) \,, \tag{2.4}$$

where $\vec{d}$ is the dipole moment operator, and $\vec{E}$ is the electric field [21]. This interaction Hamiltonian has made the dipole approximation, which assumes that the atom is small compared to the wavelength of the electric field, and so spatial dependence of $\vec{E}$ can be ignored. The dipole operator should have only off-diagonal terms, and can be written as

$$\vec{d} = \vec{d}_{eg}\sigma^+ + \vec{d}_{ge}\sigma^- . \tag{2.5}$$

The electric field operator for a single mode of the cavity is given by

$$\vec{E} = \vec{\epsilon}\sqrt{\frac{\hbar\omega_c}{2\epsilon_0 V}} \left( a e^{-i\omega_c t} + a^\dagger e^{+i\omega_c t} \right), \tag{2.6}$$

where $\vec{\epsilon}$ is the polarisation operator and $V$ is the volume of the cavity mode. Finally, Equation 2.4 becomes,

$$H_I = -g\hbar \left( \sigma^+ + \sigma^- \right) \left( a e^{-i\omega_c t} + a^\dagger e^{+i\omega_c t} \right), \tag{2.7}$$

where

$$g = \sqrt{\frac{\omega_c \left|\mu_{eg}\right|^2}{2\hbar\epsilon_0 V}} \qquad \text{and} \qquad \mu_{eg} = \langle e|\, \vec{d} \cdot \vec{\epsilon}\, |g\rangle \,.$$

The interaction Hamiltonian can be simplified by making a unitary transformation of the form $H \to U^\dagger H U$ where $U = e^{-i\sigma^+\sigma^-\omega_a t} = |e\rangle\langle e| e^{-i\omega_a t} + |g\rangle\langle g|$. After this transformation, there are a pair of terms in $H_I$ which have frequencies $\pm(\omega_c + \omega_a)$ and a pair which have frequencies $\pm(\omega_c - \omega_a)$. When the cavity is near resonance with the atoms ($\Delta_{ac} = \omega_c - \omega_a \approx 0$), each pair of terms evolve according to vastly different timescales. On the timescale of the slowly-evolving terms, the quickly-evolving terms average to zero, and can be ignored. This is known as the rotating-wave approximation [21], and is valid when $\Delta_{ac} << \omega_c + \omega_a$. The resulting Hamiltonian is,

$$H_I = -g\hbar\left(a\sigma^+ e^{-i\Delta_{ac}t} + a^\dagger\sigma^- e^{+i\Delta_{ac}t}\right). \tag{2.8}$$

By making another unitary transformation of the form $H \to U^\dagger H U$ where $U = e^{-i\sigma^+\sigma^-\Delta_{ac}t} = |e\rangle\langle e| e^{-i\Delta_{ac}t} + |g\rangle\langle g|$, the time dependence in the interaction Hamiltonian can be removed completely. The interaction Hamiltonian now has the form,

$$H_I = -g\hbar\left(a\sigma^+ + a^\dagger\sigma^-\right). \tag{2.9}$$

Finally, putting $H_A$, $H_C$ and $H_I$ into Equation 2.1 results in the well-known Jaynes-Cummings Hamiltonian [8],

$$H = \hbar\omega_a\sigma^+\sigma^- + \hbar\omega_c a^\dagger a - g\hbar\left(a\sigma^+ + a^\dagger\sigma^-\right). \tag{2.10}$$

Using a subset of the tensor product basis $|g, n+1\rangle$ and $|e, n\rangle$, this can be written,

$$H = \hbar\begin{pmatrix} n\omega_c & -g\sqrt{n} \\ -g\sqrt{n} & n\omega_c - \Delta_{ac} \end{pmatrix}, \tag{2.11}$$

which has the eigenvalues,

$$\frac{E_{\pm,n}}{\hbar} = n\omega_c - \frac{\Delta_{ac}}{2} \pm \sqrt{\left(\frac{\Delta_{ac}}{2}\right)^2 + g^2 n}\,, \tag{2.12}$$

and eigenstates (using the method outlined in [22]),

$$\begin{aligned} |+, n\rangle &= +\cos\theta\,|g, n+1\rangle + \sin\theta\,|e, n\rangle\,, \\ |-, n\rangle &= -\sin\theta\,|g, n+1\rangle + \cos\theta\,|e, n\rangle\,, \end{aligned} \tag{2.13}$$

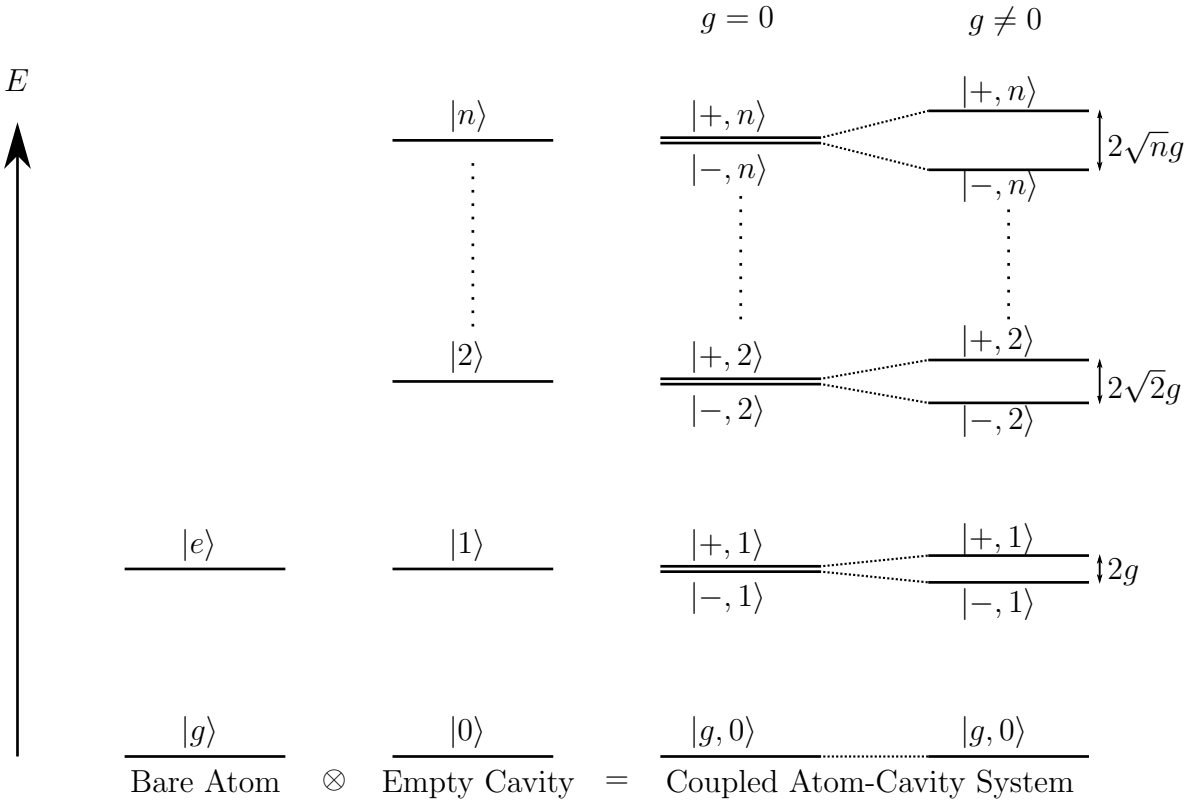


Figure 2.1: When the bare atom and empty cavity are coupled, the Jaynes-Cummings ladder of dressed states is formed. In the figure, the atom-cavity detuning is zero. When the coupling $g$ is zero, the dressed state doublets are degenerate. As the coupling $g$ increases, the doublets separate in energy by $2\sqrt{n}g$.

where

$$\tan 2\theta = \frac{2\sqrt{n}g}{\Delta_{ac}}.$$

At $\Delta_{ac} = 0$ and $g = 0$, $|g, n+1\rangle$ and $|e, n\rangle$ eigenstates are degenerate. However, as the atom-cavity coupling $g$ increases, the system divides into the new dressed eigenstates $|+, n\rangle$ and $|-, n\rangle$. Figure 2.1 shows the ladder of doublet states produced by this system, and the splitting produced when $g$ is non-zero. This splitting is known as normal-mode splitting (also known as vacuum field Rabi Splitting), and was first experimentally observed in 1989 [23, 24, 25]. It should be noted that the frequency by which the doublets are split is also the frequency at which the atom and cavity exchange excitation [26, 27], and hence the coupling constant $g$ is often referred to as the single-photon, single-atom Rabi frequency.

### 2.1.2 Introducing Losses

The last section focused on a two-level atom coupled to a cavity without losses. This is an unrealistic model, and so the focus of this section will be on extending this model to retrieve a theoretical spectrum for the cavity transmission. The theoretical results in this section will be important when interpreting the main results of the experiment in Chapter 7.

In reality, the system will experience losses due to spontaneous emission from the atoms and leakage of light from the cavity due to the mirror losses. The atomic excitation will decay at a rate given by the HWHM natural linewidth $\gamma$, and the cavity excitation will decay due to losses from the mirrors at a rate given by the HWHM linewidth $\kappa$. In addition to losses, the cavity will be driven by a probe laser of frequency $\omega_p$ at a rate $\eta$.

Incorporating these factors into Equation 2.10 gives the non-Hermitian Hamiltonian,

$$\begin{aligned} H = \hbar\omega_a\sigma^+\sigma^- + \hbar\omega_c a^\dagger a - g\hbar\left(a\sigma^+ + a^\dagger\sigma^-\right) \\ - i\hbar\gamma\sigma^+\sigma^- - i\hbar\kappa a^\dagger a - i\hbar\eta(ae^{+i\omega_p t} + a^\dagger e^{-i\omega_p t}). \end{aligned} \tag{2.14}$$

This Hamiltonian can be transformed into a frame rotating at the probe frequency by transforming twice, with $\hat{U}^\dagger H\hat{U} - \hat{h}$ where $\hat{U} = \exp(-i\hat{h}t)$, firstly with $\hat{h} = \hbar\omega_p\sigma^+\sigma^-$ and then with $\hat{h} = \hbar\omega_p a^\dagger a$, resulting in the time-independent form [28]

$$\begin{aligned} H = \hbar\Delta_{ap}\sigma^+\sigma^- + \hbar\Delta_{cp}a^\dagger a - g\hbar\left(a\sigma^+ + a^\dagger\sigma^-\right) \\ - i\hbar\gamma\sigma^+\sigma^- - i\hbar\kappa a^\dagger a - i\hbar\eta(a + a^\dagger), \end{aligned} \tag{2.15}$$

where $\Delta_{ap} = \omega_a - \omega_p$ and $\Delta_{cp} = \omega_c - \omega_p$. Assuming a weak probe intensity and restricting ourselves to $|g,0\rangle$, $|g,1\rangle$ and $|e,0\rangle$, the time-dependent state of the coupled system can be written as

$$|\Psi(t)\rangle = c_0(t)\,|g,0\rangle + c_g(t)\,|g,1\rangle + c_e(t)\,|e,0\rangle\,. \tag{2.16}$$

Putting this Hamiltonian and state vector into the Schrödinger equation,

$$H\,|\Psi(t)\rangle = i\hbar\frac{\partial}{\partial t}\,|\Psi(t)\rangle\,, \tag{2.17}$$

and taking $c_0 \approx 1$ since the probe intensity is weak, yields the equations

$$\begin{aligned} \dot{c_g} &= igc_e - (\kappa + i\Delta_{cp})c_g + \eta, \\ \dot{c_e} &= igc_g - (\gamma + i\Delta_{ap})c_e. \end{aligned} \tag{2.18}$$

The cavity transmission will be proportional to the average number of photons inside the cavity $\langle n \rangle$. This quantity is given by the probability of the system $|\Psi\rangle$ being in state $|g, 1\rangle$, which is given by $|c_g|^2$. This quantity can be found in the steady state by solving Equations 2.18 where $\dot{c_g} = \dot{c_e} = 0$,

$$\begin{aligned} \langle n \rangle = |c_g|^2 &= \left| \frac{-i\eta \left(\Delta_{ap} - i\gamma\right)}{g^2 - \left(\Delta_{ap} - i\gamma\right)\left(\Delta_{cp} - i\kappa\right)} \right|^2 , \\ &= \frac{\eta^2 \left(\Delta_{ap}^2 + \gamma^2\right)}{\left(\Delta_{cp}\gamma + \Delta_{ap}\kappa\right)^2 + \left(g^2 + \gamma\kappa - \Delta_{ap}\Delta_{cp}\right)^2} . \end{aligned} \tag{2.19}$$

The mean number of photons on resonance ($\Delta_{ap}, \Delta_{cp} = 0$) in an empty cavity ($g = 0$) will be $\eta^2/\kappa^2$. Given a resonant, empty cavity transmission of $T_0$, the transmission of the detuned atom-cavity system will therefore be

$$\frac{T}{T_0} = \left(\frac{\kappa}{\eta}\right)^2 \langle n \rangle = \frac{\kappa^2 \left(\Delta_{ap}^2 + \gamma^2\right)}{\left(\Delta_{cp}\gamma + \Delta_{ap}\kappa\right)^2 + \left(g^2 + \gamma\kappa - \Delta_{ap}\Delta_{cp}\right)^2} . \tag{2.20}$$

Equation 2.20 is plotted in Figure 2.2 for a range of cavity-atom and probe-atom detunings. It can be seen that when atoms are introduced, the cavity transmission splits into two peaks around where the empty cavity and bare atom eigenvalues (represented by dashed lines) cross one another. This image is known as the avoided crossing [29] and a slice across this shows the normal-mode splitting at a given cavity-atom detuning.

### 2.1.3 Collective Coupling of N Atoms to the Cavity

So far this chapter has only considered a single atom interacting with the cavity mode. When many atoms are in the cavity mode, they can act collectively and coherently [30]. This extension to the Jaynes-Cummings model is known as the Tavis-Cummings model [10, 31, 32]. In this extension, the Jaynes-Cumming Hamiltonian (Equation 2.10) becomes,

$$H = \hbar\omega_a S^z + \hbar\omega_c a^\dagger a - g\hbar \left(aS^+ + a^\dagger S^-\right) , \tag{2.21}$$

where $S^{\pm,z}$ are the collective atomic spin operators for an ensemble of $N$ two-level atoms,

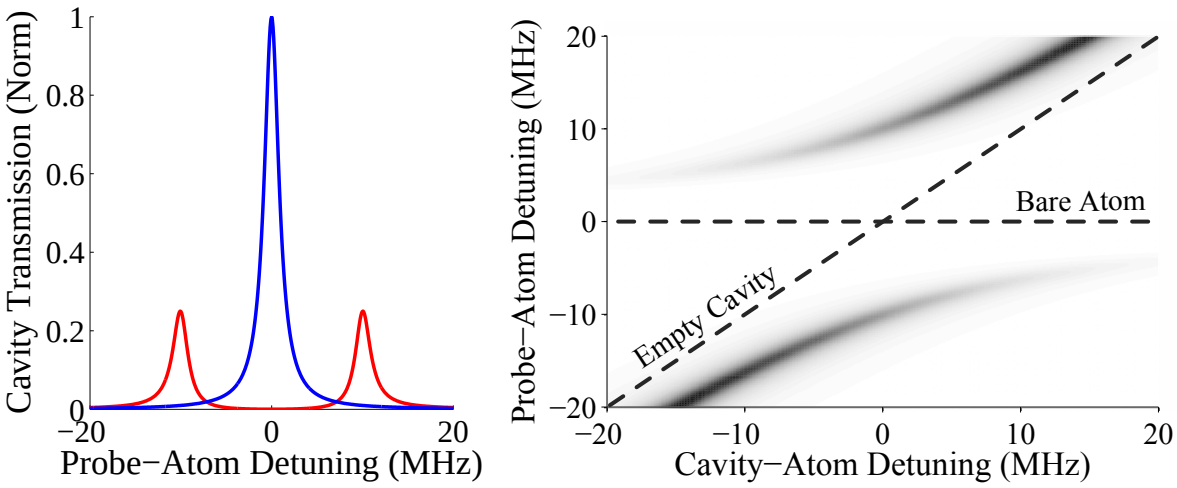


(a) Normal-mode splitting (b) Avoided crossing

Figure 2.2: Transmission of the cavity for $\kappa = 2\pi \cdot 1\,\text{MHz}$ and $\gamma = 2\pi \cdot 3\,\text{MHz}$. (a) shows the cavity transmission for $\Delta_{ac} = 0$ with the atom ($g = 2\pi \cdot 10\,\text{MHz}$, red) and without the atom ($g = 0$, blue). (b) shows the transmission for $g = 2\pi \cdot 10\,\text{MHz}$ with respect to the cavity-atom and probe-atom detunings. The empty cavity and bare atom eigenvalues are represented as dashed lines.

which take the form

$$\begin{aligned} S^+ &= \sum_{i=1}^{N} |e_i\rangle \langle g_i| , \\ S^- &= \sum_{i=1}^{N} |g_i\rangle \langle e_i| , \\ S^z &= \sum_{i=1}^{N} \frac{|e_i\rangle \langle e_i| - |g_i\rangle \langle g_i|}{2} , \end{aligned} \tag{2.22}$$

where $|e_i\rangle$ and $|g_i\rangle$ represent the excited state and ground state for each atom. For the case of weak probing, the number of excitations $n$ in the system is less than the number of atoms in the system ($n \ll N$), the energies for each eigenstate can be approximated by [33]

$$\frac{E(n,j)}{\hbar} \approx \left(n - \frac{N}{2}\right)\omega_a - \frac{n}{2}\Delta_{ac} + j\sqrt{4g^2N + \Delta_{ac}^2}, \tag{2.23}$$

where $0 \leq n \ll N$ and the integer $j$ where $-n/2 \leq j \leq +n/2$ denotes the total atomic excitation. For a transition between $|n, j\rangle$ and $|n+1, j'\rangle$, the transition energy will be

$$\frac{\Delta E(j,j')}{\hbar} = \frac{\omega_a + \omega_c}{2} + (j - j')\sqrt{4g^2N + \Delta_{ac}^2}, \tag{2.24}$$

If a single photon is absorbed per transition, $j - j' = \pm 1/2$, and thus the normal-mode splitting around $\Delta_{ac} = 0$ for $N$ atoms becomes $2g\sqrt{N}$. Hence the single atom Rabi frequency $g$ becomes the $N$-atom Rabi frequency $G = \sqrt{N}g$, which can be substituted directly for $g$ in the cavity transmission spectrum obtained in Equation 2.20 to produce an $N$-atom spectrum.

### 2.1.4 Collective Strong Coupling and Cooperativity

Not only is the transmission spectrum modified by increasing the atom number to $N$, but the exchange rate of excitation between the cavity and atoms is also modified from $g$ to $G = g\sqrt{N}$. At this point, it is useful to discuss the meaning of 'strongly' coupled atom-cavity systems.

A cavity and single atom are said to be strongly coupled if the rate at which the atom and cavity coherently exchange excitation is fast compared to the dissipation rates from the system $\kappa$ and $\gamma$. The single atom cooperativity is given by

$$C = \frac{g^2}{\kappa\gamma}, \tag{2.25}$$

and if $C > 1$, the system is dominated by the atom-cavity interaction and the two systems are said to be strongly coupled. One method of achieving single atom strong coupling is to use very small cavities known as micro-cavities [34], which have a length of a few hundred microns. The short length results in a very small mode volume and thus a large Rabi frequency $g$. The short length however increases the cavity loss rate $\kappa$, and thus micro-cavities are usually required to have ultrahigh finesse [35]. When working in the microwave regime, the use of long-lived Rydberg excited states can also be used to obtain a small spontaneous emission rate $\gamma$ [36].

In an $N$-atom system, the rate of coherent exchange is enhanced from $g$ to $g\sqrt{N}$. The collective cooperativity is given by

$$C_N = \frac{Ng^2}{\kappa\gamma} = \frac{G^2}{\kappa\gamma}, \tag{2.26}$$

where if $C_N > 1$, the system is said to be collectively strongly coupled. In this case, strong coupling can be achieved with larger cavities of a few centimetres at significantly lower finesse. This approach is the approach taken in this work, where we have $(g, \kappa, \gamma) = 2\pi(0.09, 0.92, 2.98)$MHz. For these parameters, an intra-cavity atom number of $N > 350$ is required to enter the collective strong coupling regime.

## 2.2 Slow Light and Electromagnetically-Induced Transparency In an Optical Cavity

The purpose of this section is to theoretically discuss the phenomenon of slow light and how this can arise from electromagnetically-induced transparency (EIT) from a lambda-style atomic system placed inside an optical cavity. Firstly, the group index and group velocity will be introduced, and then EIT will be considered.

### 2.2.1 Group Refractive Index

The phase of a plane-wave light beam with frequency $\omega$ propagating along $z$ is given by

$$\phi = kz - \omega t\,, \tag{2.27}$$

where the wave number in a medium with refractive index $n$ is given by $k = \omega n/c$. A wavefront (a plane of constant phase) will travel a distance $\Delta z$ during a time $\Delta t$, and hence the velocity of wavefronts (the phase velocity) is given by

$$v_p = \frac{\Delta z}{\Delta t} = \frac{\omega}{k} = \frac{c}{n}\,. \tag{2.28}$$

If we are instead concerned with the speed of propagation of a pulse of light, this monochromatic treatment is inadequate since a pulse is described by the sum of its many Fourier components, at many different frequencies. In this case, the 'pulse' is actually a traveling point where the Fourier components tend to constructively interfere. The pulse $E(z,t)$ can be described by [37]

$$E(z,t) = \int_{-\infty}^{\infty} \frac{dk}{2\pi} \tilde{E}(k) e^{i(kz - \omega(k)t)}\,, \tag{2.29}$$

and Taylor expanding $\omega(k)$ around a central wave number $k_0$ up to first order gives,

$$\omega(k) \approx \omega(k_0) + (k - k_0)\frac{d\omega}{dk}\Big|_{k=k_0}\,. \tag{2.30}$$

Putting this into Equation 2.29, and using $\omega_0 = \omega(k_0)$ and $v_g \equiv (d\omega/dk)\big|_{k=k_0}$

$$\begin{aligned} E(z,t) &= \int_{-\infty}^{\infty} \frac{dk}{2\pi} \tilde{E}(k) e^{i(k(z-v_g t)+k_0 v_g t-\omega_0 t)}\,, \\ &= e^{i(k_0 z-\omega_0 t)} \int_{-\infty}^{\infty} \frac{dk}{2\pi} \tilde{E}(k) e^{i(k-k_0)(z-v_g t)}\,, \\ &= e^{i(k_0 z-\omega_0 t)} E(z-v_g t, 0)\,, \end{aligned} \tag{2.31}$$

and so it can be seen that the wave packet of a pulse $E(z,t)$ travels at the group velocity $v_g$, whilst the individual Fourier components still propagate at the phase velocity. It is then useful to define the group refractive index as,

$$\begin{aligned} n_g &= \frac{c}{v_g} = c\frac{dk}{d\omega}\,, \\ &= n + \omega \frac{dn}{d\omega}\,. \end{aligned} \tag{2.32}$$

It can be seen that the group index can potentially be vastly different from $n$, depending on the sign and magnitude of the dispersion $dn/d\omega$ [38]. Although group velocities greater than $c$ are possible, this does not violate causality, due to the distortion of the pulse [39, 40, 41].

In this project, the work is currently focused on establishing EIT and using its effects to modify the group index of the intra-cavity medium. The modified group index will then modify the cavity decay rate.

### 2.2.2 Refractive Index and Susceptibility

It is useful to separate the refractive index into its real and imaginary parts using,

$$n = n' + in'' = \sqrt{1+\chi} \approx 1 + \frac{\chi'}{2} + i\frac{\chi''}{2}\,, \tag{2.33}$$

where $\chi$ is the susceptibility, which has real and imaginary parts $\chi'$ and $\chi''$. Note that the wave number inside a medium $k$ relates to the vacuum number $k_v$ as $k = nk_v$, and so the electric field is affected like so,

$$\begin{aligned} E(z,t) &= E_0 e^{i(kz-\omega t)}\,, \\ &= E_0 e^{i(k_v z-\omega t)} e^{i\frac{k_v z}{2}\chi'} e^{-\frac{k_v z}{2}\chi''}\,. \end{aligned} \tag{2.34}$$

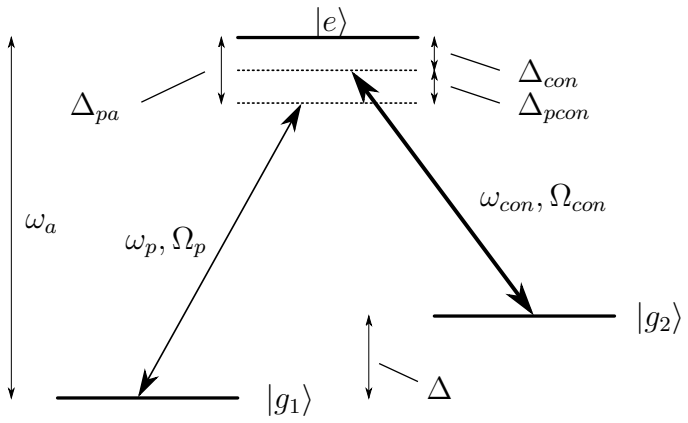


Figure 2.3: An EIT lambda-style system. The atom experiences strong pumping on the $|g_2\rangle \rightarrow |e\rangle$ transition due to the EIT coupling beam with frequency $\omega_{con}$ and Rabi frequency $\Omega_{con}$. The atom is also probed weakly on the $|g_1\rangle \rightarrow |e\rangle$ transition using a beam with frequency $\omega_p$ and Rabi frequency $\Omega_p$.

It can be seen that the refractive index (or susceptibility) affects the field in two ways. The real part $\chi'$ describes a phase shift, and the imaginary part $\chi''$ describes absorption along $z$. This information will be useful when deriving a term for the cavity transmission, where the round-trip phase and losses inside the cavity are modified when $n \neq 1$.

### 2.2.3 Electromagnetically-Induced Transparency in an Optical Cavity

EIT is a phenomenon which arises in a three-level atom, whereby a narrow transparency window in the absorption spectrum of the atom appears when the atom is subject to a weak probe beam and an intense control beam. The purpose of this section is to find an expression for the the transmission spectrum of a cavity containing an EIT medium. Here, the three level atom will be considered as a lambda-style system with two ground states $|g_1\rangle$ and $|g_2\rangle$ and one excited state $|e\rangle$, as shown in Figure 2.3. The low intensity cavity-atom probe beam at frequency $\omega_p$ addresses the $|g_1\rangle \rightarrow |e\rangle$ transition and an intense EIT control beam at frequency $\omega_{con}$ addresses the $|g_2\rangle \rightarrow |e\rangle$ transition. At first, a semi-classical approach will be taken where both of these fields will be considered classically, whilst the atom is considered quantum mechanically. After this, a fully quantum mechanical model will be considered and compared with the semi-classical model.

### 2.2.4 The Semi-Classical Model

The refractive index of the atomic medium $n$ is related to the susceptibility of the atoms $\chi(\omega_p)$ by,

$$n = \sqrt{1+\chi}\,, \tag{2.35}$$

Since we will only be using a weak cavity field, it is useful to only consider the linear component of the susceptibility, $\chi^{(1)}(\omega_p)$. The linear susceptibility relates atomic polarisation to the electric field by,

$$P = \epsilon_0 \chi E\,, \tag{2.36}$$

where

$$P = \mathcal{N}\mu_{g_1 e}\rho_{g_1 e}e^{i(kz-\omega_p t)}\,, \tag{2.37}$$

$$E = E_0 e^{i(kz-\omega_p t)}\,. \tag{2.38}$$

Where $\mathcal{N}$ is the density of atoms in the cavity mode, and $\mu_{g_1 e}$ and $\rho_{g_1 e}$ are the dipole matrix and density matrix elements for the $|g_1\rangle \leftrightarrow |e\rangle$ transition [16, 42, 43].

Using Equation 2.7 to relate $\mu_{g_1 e}$ to $g$,

$$|\mu_{e g_1}|^2 = \frac{2g^2\hbar\epsilon_0 V}{\omega_p}\,, \tag{2.39}$$

and using $E_0 = \hbar\Omega_p/\mu_{e g_1}$ and $\mathcal{N} = N/V$ where $\Omega_p$ is the Rabi frequency for the probe beam, $N$ is the effective number of atoms in the cavity mode and $V$ is the cavity mode volume; $\chi^{(1)}$ can be shown to be,

$$\chi^{(1)} = \frac{2Ng^2}{\omega_p\Omega_p}\rho_{g_1 e}\,. \tag{2.40}$$

The coherence $\rho_{g_1 e}$ must be calculated quantum mechanically from a three-level atom in the presence of the two classical fields. The corresponding Hamiltonian for this system is

$$\begin{aligned}\frac{\hat{H}}{\hbar} = \omega_e |e\rangle\langle e| + \Delta |g_2\rangle\langle g_2| - \Omega_c\Big(|g_2\rangle\langle e| + |e\rangle\langle g_2|\Big)\cos(\omega_{con}t) \\ -\Omega_p\Big(|g_1\rangle\langle e| + |e\rangle\langle g_1|\Big)\cos(\omega_p t)\,.\end{aligned} \tag{2.41}$$

Where the frequencies are shown on Figure 2.3. Making two transformations of the form $\hat{H} \rightarrow \hat{U}^{\dagger}\hat{H}\hat{U} - \hat{h}$ where $\hat{U} = e^{-i\hat{h}t}$ with $\hat{h} = \omega_p \left|e\right\rangle \left\langle e\right|$ and $(\omega_p - \omega_{con}) \left|g_2\right\rangle \left\langle g_2\right|$, and making the rotating wave approximation, this Hamiltonian can be simplified to

$$\begin{aligned}\frac{\hat{H}}{\hbar} = -\Delta_{pa} \left|e\right\rangle \left\langle e\right| - (\Delta_{pcon} - \Delta) \left|g_2\right\rangle \left\langle g_2\right| \\ - \frac{\Omega_c}{2}\Big( \left|g_2\right\rangle \left\langle e\right| + \left|e\right\rangle \left\langle g_2\right| \Big) - \frac{\Omega_p}{2}\Big( \left|g_1\right\rangle \left\langle e\right| + \left|e\right\rangle \left\langle g_1\right| \Big),\end{aligned} \tag{2.42}$$

with $\Delta_{pa} = \omega_p - \omega_a$ representing the detuning between the probe and the $\left|g_1\right\rangle \rightarrow \left|e\right\rangle$ transition, and $\Delta_{pcon} = \omega_p - \omega_{con}$.

The Lindblad master equation [16, 21, 44] for this system will be,

$$\begin{aligned}\frac{d\hat{\rho}}{dt} = -\frac{i}{\hbar}\left[\hat{H}, \hat{\rho}\right] - \gamma_{eg_1}\Big( \left|e\right\rangle \left\langle e\right| \hat{\rho} + \hat{\rho} \left|e\right\rangle \left\langle e\right| - 2 \left|g_1\right\rangle \left\langle e\right| \hat{\rho} \left|e\right\rangle \left\langle g_1\right| \Big) \\ - \gamma_{eg_2}\Big( \left|e\right\rangle \left\langle e\right| \hat{\rho} + \hat{\rho} \left|e\right\rangle \left\langle e\right| - 2 \left|g_2\right\rangle \left\langle e\right| \hat{\rho} \left|e\right\rangle \left\langle g_2\right| \Big),\end{aligned} \tag{2.43}$$

which can be solved to first order in the probe Rabi frequency $\Omega_p$ to yield

$$\rho_{g_1 e} = \Omega_p \frac{1}{-\Delta_{pa} + \frac{\Omega_{con}^2}{4\Delta_{pcon} + 2i\gamma_{deph}} - i\gamma}. \tag{2.44}$$

Where $\gamma_{deph}$ is a phenomenological parameter which accounts for decoherence between the two groundstates due to technical limitations of the experiment. Throughout the rest of this section, $\gamma_{deph}$ is taken to be zero. This completes the expression for the susceptibility from Equation 2.40,

$$\chi^{(1)} = \frac{2Ng^2}{\omega_p} \frac{1}{-\Delta_{pa} + \frac{\Omega_{con}^2}{4\Delta_{pcon}} - i\gamma}. \tag{2.45}$$

In Section 2.2.2, it was shown that the phase shift of the field due to the presence of the EIT medium is given by the real part of the refractive index $n'$, whilst the imaginary part $n''$ describes the attenuation of the light. When a medium with refractive index $n$ is placed into a cavity of empty free spectral range $\omega_{\mathrm{FSR}} = 2\pi \times c/L$, the modified phase accumulation per round-trip becomes,

$$\begin{aligned}\Phi' &= \Phi_0 \left(1 + \frac{\chi'}{2}\right), \\ &= \Phi_0 + 2\pi \frac{\omega_p}{\omega_{\mathrm{FSR}}} \frac{\chi'}{2},\end{aligned} \tag{2.46}$$

where $\Phi_0(\omega_p)$ is the empty cavity round-trip phase for probe frequency $\omega_p$.

The fraction of power remaining in the cavity will be determined by the mirror reflectivities, as well as the transmission through the EIT medium. The fractional power remaining after one round-trip for a ring-cavity[1] will be

$$\rho' = \rho_0 T_m \,, \tag{2.47}$$

where $\rho_0$ is the fractional remaining power due to the mirrors (discussed in more detail later, in Section 5.1.1) and $T_m$ is the fractional power transmission through the atomic medium. Assuming that the atomic absorption is small, $T_m$ will be described by,

$$\begin{aligned} T_m &= \left( \exp\left\{ -kl\frac{\chi''}{2} \right\} \right)^2 , \\ &\approx 1 - kl\chi'' , \end{aligned} \tag{2.48}$$

where $l$ is the length of the absorption medium. Since we are working with a homogeneous atomic density $\mathcal{N}$ spread across the volume of a ring cavity[2], we can say that $l$ is equal to the full round-trip length, and hence $kl = kL = \Phi_0$, and

$$\rho' = \rho_0(1 - \Phi_0\chi'') = \rho_0 \left( 1 - 2\pi \frac{\omega_p}{\omega_{\text{FSR}}} \chi'' \right) . \tag{2.49}$$

With expressions for the phase accumulation and remaining power after one round-trip, we can use the method outlined in Section 5.1.1 to get an expression for the cavity transmission, analogous to Equation 5.4,

$$\frac{I_t}{I_0} = \frac{T_1 T_2 T_m}{(1 - \sqrt{\rho'})^2 + 4\sqrt{\rho'} \sin^2\left(\frac{\Phi'}{2}\right)} , \tag{2.50}$$

where $T_{1,2}$ are the transmission coefficients for the input and output mirrors. If $T = T_1 = T_2$ and the transmission coefficient of the third mirror is significantly smaller than $T$, then $\rho_0 \approx (1 - T)^2$. This leads to, $T_1 T_2 \approx (1 - \sqrt{\rho_0})$. Finally, Equation 2.50 becomes

$$\frac{I_t}{I_0} = \frac{T_m(1 - \sqrt{\rho_0})}{(1 - \sqrt{\rho'})^2 + 4\sqrt{\rho'} \sin^2\left(\frac{\Phi'}{2}\right)} . \tag{2.51}$$

[1]Note that for a Fabry-Pérot cavity the light passes through the atomic medium twice, and so the round-trip loss will be $\rho' = \rho_0 T_m^2$.

[2]Note that in the case of a Fabry-Pérot cavity, the length of the absorption medium $l$ is equal to half of the round-trip length, and so $kl = \Phi_0/2$.

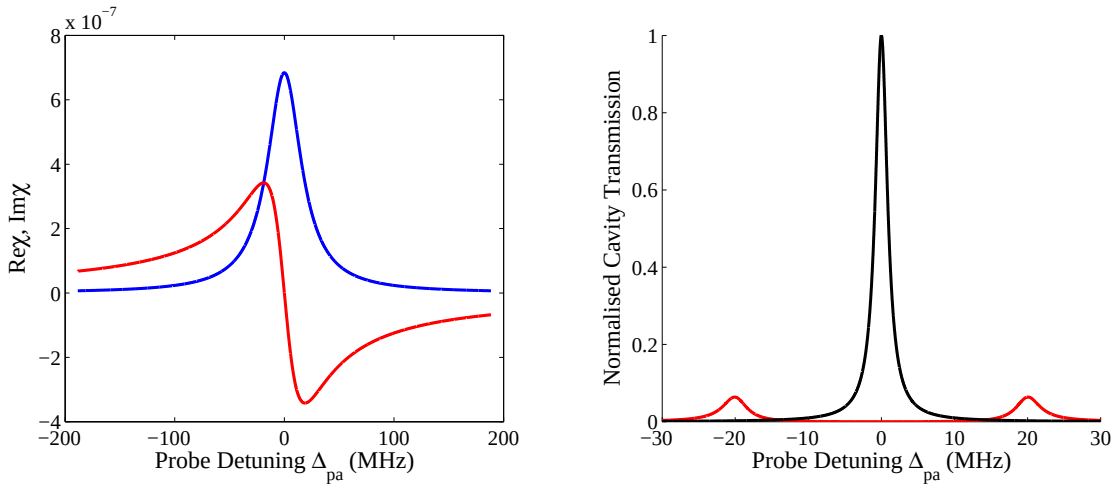


(a) (b)

Figure 2.4: (a) Calculation of real and imaginary parts of the susceptibility (red and blue lines) and (b) the cavity transmission with and without the two-level atom (red and black lines). Here, $\Omega_{con} = 0$, $g = 2\pi \cdot 20\,\text{MHz}$, $\kappa = 2\pi \cdot 1\,\text{MHz}$ and the atom-cavity detuning is zero.

To compare this semi-classical approach to a quantum mechanical approach, it's necessary to write $\rho_0$ in terms of the cavity field loss rate $\kappa$ (the HWHM linewidth). From Equations 5.7 and 5.8, $\rho_0$ can be written as.

$$\rho_0 = 1 - 4\pi \frac{\kappa}{\omega_{\text{FSR}}}\,, \tag{2.52}$$

where $\kappa$ has been written in units of angular frequency. It is also useful to write $\Phi_0$ in terms of $\Delta_{pc}$ with,

$$\begin{aligned} \Phi_0 &= 2\pi \frac{\omega_p}{\omega_{\text{FSR}}} = 2\pi \left( \frac{\omega_p - \omega_c}{\omega_{\text{FSR}}} + \frac{\omega_c}{\omega_{\text{FSR}}} \right)\,, \\ &= 2\pi \frac{\Delta_{pc}}{\omega_{\text{FSR}}}\,. \end{aligned} \tag{2.53}$$

Where $\omega_c/\omega_{\text{FSR}}$ is equal to the longitudinal mode number (an integer) and can be ignored. A quick comparison between this semi-classical approach and a fully quantum mechanical approach can be made in the two-level case by removing the EIT coupling beam by setting $\Omega_c = 0$ and thus removing the third level. The results agree perfectly with Equation 2.20,

$$\frac{I_t}{I_0} = \frac{\kappa^2 \left(\Delta_{pa}^2 + \gamma^2\right)}{\left(\Delta_{pc}\gamma + \Delta_{pa}\kappa\right)^2 + \left(g^2 + \gamma\kappa - \Delta_{pa}\Delta_{pc}\right)^2}\,, \tag{2.54}$$

and are plotted on Figure 2.4. This is interesting, because normal-mode splitting (or vacuum Rabi splitting) is often perceived to be a consequence of quantum optics (where an atom and cavity are exchanging a photon) rather than the simple classical effect of putting a dispersive medium inside an optical cavity [24].

In the three-level case ($\Omega_c \neq 0$), the transmission spectrum will take the form,

$$\frac{I_t}{I_0} = \frac{\kappa^2}{\left(\Delta_{pc} + \frac{\omega_p \chi'}{2}\right)^2 + \left(\kappa + \frac{\omega_p \chi''}{2}\right)^2}, \tag{2.55}$$

and an example spectrum is shown in Figure 2.5. It can be seen that the inclusion of the EIT coupling beam causes the absorption $\chi''$ to vanish around $\Delta_{pa} = 0$, where a narrow window of transparency appears and the dispersion of $\chi'$ changes slope.

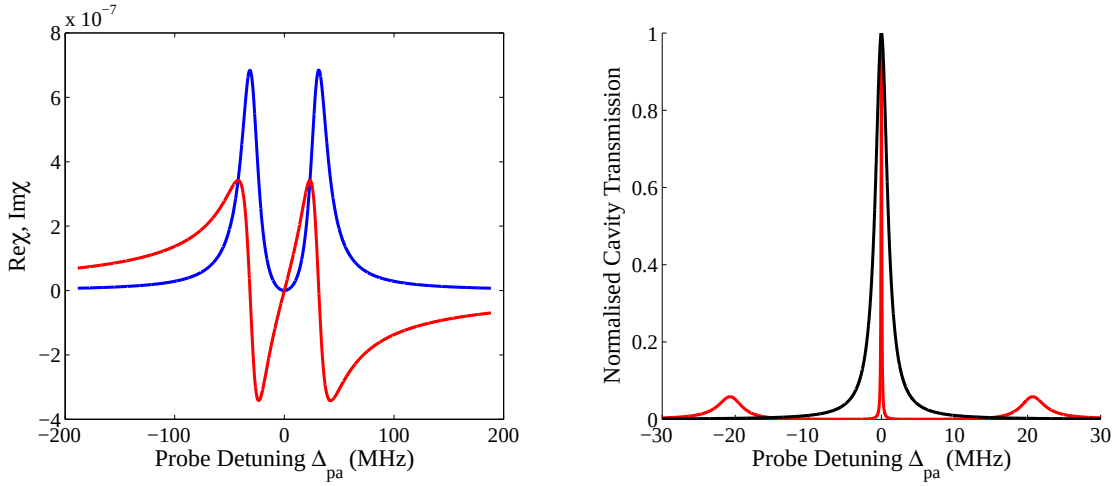


(a) (b)

Figure 2.5: (a) Calculation of real and imaginary parts of the susceptibility (red and blue lines) and (b) cavity transmission (black line shows empty cavity) in the three-level atom case where $\Omega_{con} = 2\pi \cdot 10\,\text{MHz}$. Here, $g = 2\pi \cdot 20\,\text{MHz}$, $\kappa = 2\pi \cdot 1\,\text{MHz}$, and $\Delta_{con} = \Delta_{ca} = 0$.

### 2.2.5 Fully Quantum Model

For a fully quantum mechanical treatment, we must extend the Hamiltonian for the bare three-level atom (Equation 2.42) to include terms for the cavity field and interaction

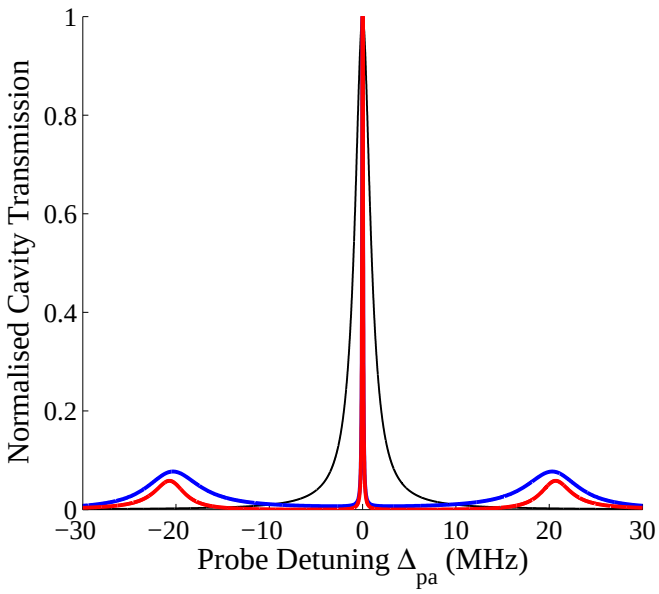


Figure 2.6: Comparison of the cavity transmission given by the semi-classical model (red) and fully quantum model (blue) for $(g, \kappa, \gamma, \Omega_c) = 2\pi \cdot (20, 1, 3, 10)$MHz. The black line shows empty cavity transmission.

terms. Using methods similar to those in Section 2.1, the non-Hermitian Hamiltonian becomes,

$$\frac{\hat{H}}{\hbar} = -\Delta_{pc} a^\dagger a - \Delta_{pa} |e\rangle\langle e| - (\Delta_{pcon} - \Delta) |g_2\rangle\langle g_2| - \frac{\Omega_c}{2}\Big(|g_2\rangle\langle e| + |e\rangle\langle g_2|\Big) - \frac{\Omega_p}{2}\Big(|g_1\rangle\langle e| + |e\rangle\langle g_1|\Big) - g\Big(|g_1\rangle\langle e| a^\dagger + |e\rangle\langle g_1| a\Big) - i\hbar\eta(a + a^\dagger), \quad (2.56)$$

and the Lindblad master equation will now be,

$$\begin{aligned}\frac{d\hat{\rho}}{dt} = -\frac{i}{\hbar}\left[\hat{H}, \hat{\rho}\right] &-\gamma_{eg_1}\Big(|e\rangle\langle e|\hat{\rho} + \hat{\rho}|e\rangle\langle e| - 2|g_1\rangle\langle e|\hat{\rho}|e\rangle\langle g_1|\Big) \\ &-\gamma_{eg_2}\Big(|e\rangle\langle e|\hat{\rho} + \hat{\rho}|e\rangle\langle e| - 2|g_2\rangle\langle e|\hat{\rho}|e\rangle\langle g_2|\Big) \\ &-\kappa\Big(a^\dagger a\hat{\rho} + \hat{\rho}a^\dagger a - 2a\hat{\rho}a^\dagger\Big),\end{aligned} \quad (2.57)$$

which was solved numerically for the steady state ($d\hat{\rho}_{ss}/dt = 0$) using the quantum optics Python module, QuTiP [45] for a range of probe-atom detunings. The normalised cavity transmission is then given by,

$$\frac{I_t}{I_0} = \left(\frac{\kappa}{\eta}\right)^2 \mathrm{Tr}(a^\dagger a \rho_{ss}). \quad (2.58)$$

The results are compared with the results of the semi-classical model in Figure 2.6 where it can be seen that the two models approximately agree.

# Part I

# Magneto-Optical Trapping with Potassium-39

CHAPTER 3

# Realisation of Magneto-Optical Trapping with $^{39}$K

This chapter details how the atoms are incorporated into the experiment using magneto-optical trapping. In this experiment, the atoms are held in a three-dimensional $^{39}$K magneto-optical trap (MOT) which is then spatially overlapped with the cavity mode.

## 3.1 Magneto-Optical Trapping

In 1975 and 1979, Hänsch and Schawlow [46] and Wineland and Itano [47] proposed the idea of cooling neutral atoms by Doppler cooling them with laser light. During 1985, laser cooling was demonstrated experimentally in one dimension [48], two dimensions [49], and finally in three dimensions [50]. The technique used is known today as the optical molasses technique, and uses a laser which is red-detuned from an atomic resonance. Due to the Doppler shift, the absorption rate is higher for atoms counter-propagating with the laser beam than those which are co-propagating with it. Once a photon is absorbed, the atom will spontaneously emit this photon in a random direction, and since the direction is random, this force will eventually average out to zero after many scattering events. This leads to a velocity-dependent net force which causes the counter-propagating atoms to lose momentum faster than the co-propagating atoms gain momentum. Adding a second beam counter-propagating to the first causes both velocity classes to lose momentum, and a cooling effect is achieved. Extending this to three dimensions, using three orthogonal pairs of counter-propagating beams, atoms can be cooled in three dimensions. This technique is limited however, since although the atoms are cooled, the atoms are not spatially confined.

To introduce spatial confinement, a quadrupole magnetic field is required. The Zeeman effect causes the atomic energy levels to split in the presence of a magnetic field according to the sign of the angular momentum of the energy level, causing the transition energy change also. A magnetic quadrupole is useful, since there is zero magnetic field at the

centre, and thus there is no Zeeman splitting. However, at small deviations from the centre, there becomes a position-dependent transition energy [51, 52]. A one-dimensional example is shown in Figure 3.1. Since selection rules apply to atomic transitions, only transitions with $\Delta m_J = 0, \pm 1$ are allowed, where $J$ is the total electronic angular momentum of the energy level, and $m_J$ is the projection of this value along the $z$ axis. Considering a stationary atom, it can be seen that if a pair of red-detuned laser beams are being used, the Zeeman splitting will match this detuning at two points away from the field zero. Since at these points the sign of $\Delta m_J$ is opposite, a restoring force can be achieved by using $\sigma^+$ polarisation for one beam and $\sigma^-$ polarisations for the other. This gives rise to a spatially-dependent force and confines the atoms close to the field zero. This can be extended to three dimensions to generate cooling and trapping in three dimensions.

This combination of velocity-dependent cooling and spatially-dependent trapping is known as the magneto-optical trap (MOT) and was first achieved in 1988 [53]. Several years later in 1997, the Nobel prize was awarded to Chu, Cohen-Tannoudji and Phillips for their work on laser cooling [54, 55, 56].

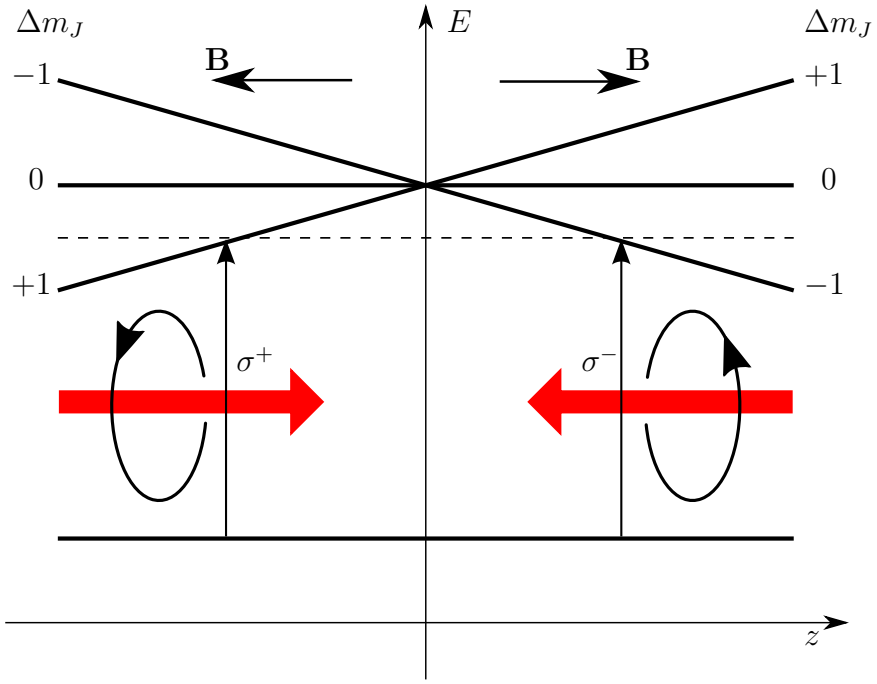


Figure 3.1: Operational principle of magneto-optical trapping in one dimension.

### 3.1.1 Trapping in Two Dimensions

In addition to confining atoms to a point of zero magnetic field in a 3D MOT, magneto-optical trapping can be used to confine atoms along a line of zero magnetic field generated by a two-dimensional magnetic quadrupole. This system is known as a 2D MOT [57]. In this experiment, a 2D MOT is used to generate an atomic beam. This atomic beam is then used to load the 3D MOT.

### 3.1.2 Trapping Potassium-39

In this experiment, $^{39}$K is being trapped. The main benefit for using potassium is that it has a narrow ground state splitting compared to other alkali metals. Since this splitting is narrow (460 MHz), it is easy to create a coherent pair of EIT probe and coupling beams using acousto-optical modulators, allowing us to avoid more technologically challenging techniques such as injection-locking, which must be used when using larger ground state splittings. Another reason for using potassium is that it has both bosonic ($^{39}$K, $^{41}$K) and fermionic ($^{40}$K) isotopes, which may provide interesting topics for study in the future.

The cooling and trapping occurs on the $D_2$ line of $^{39}$K, the structure of which appears in Figure 3.2. As with the commonly used $^{87}$Rb, the cooling and trapping is primarily done on the $F = 2 \rightarrow F' = 3$ transition with a red-detuned beam and in order to avoid optically pumping the atoms into the $F = 1$ ground state, the atoms are repumped on the $F = 1 \rightarrow F' = 2$ transition. In contrast to $^{87}$Rb however, potassium has relatively small hyperfine splitting with respect to the natural atomic linewidth ($\Gamma = 2\pi \cdot 6.04\,\text{MHz}$ for the $D_2$ line [58]). This means that in potassium, all $F = 2 \rightarrow F' = 1, 2, 3$ and $F = 1 \rightarrow F' = 0, 1, 2$ transitions are being addressed; no cycling transition exists and a six-level model is required to describe the system. In our $^{39}$K MOT, this leads to a requirement for the repump beam to also play a role in cooling, meaning the repumping beam must also be red-detuned and of comparable intensity to the cooling beam.

## 3.2 MOT Laser System

This section details the laser system required for achieving laser cooling and trapping so that atoms can be placed into the cavity mode. To do this, atoms are suspended in a 3D MOT which is spatially overlapped with the cavity mode. The laser system used

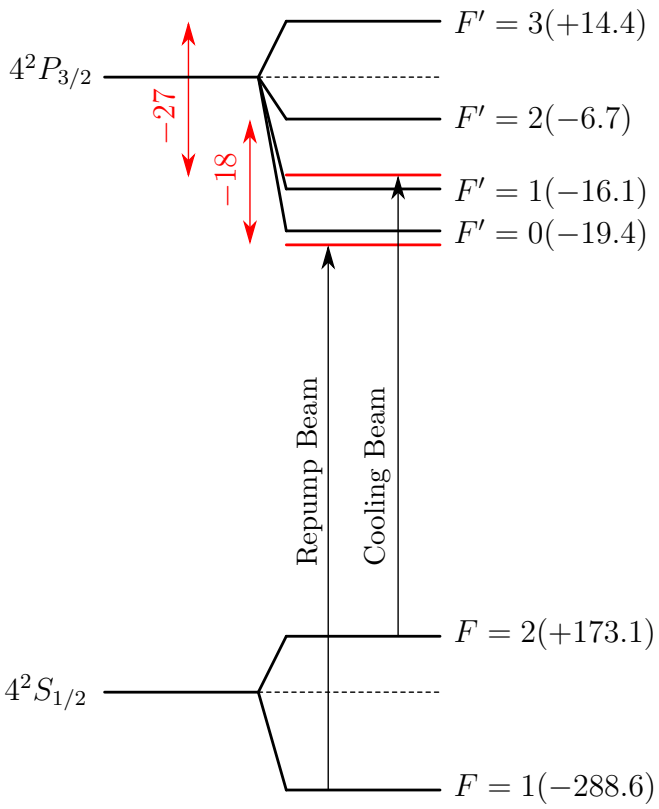


Figure 3.2: Transition diagram for the $D_2$ line of $^{39}$K, with cooling and repump frequencies shown in red. Numbers in brackets show the values of the hyperfine splittings for each energy level. All frequencies are in units of MHz.

in probing the cavity and achieving EIT is discussed in Section 5.3. In the previous generation of the experiment, there was a problem with the cavity mirrors getting dirty from dispenser usage [59, 60]. In order to circumvent this problem, the experiment has recently been updated to load the 3D MOT from an atomic beam generated from a 2D MOT, rather than loading directly from the potassium dispensers. For simplicity, the cooling and repump frequencies for the 3D MOT are the same as those used in the 2D MOT. In addition to the cooling and repump beams, a pushing beam is required to push atoms from the 2D MOT into the the 3D MOT.

The laser system used is outlined in Figure 3.3. The laser system consists of three homemade extended-cavity diode lasers (ECDLs) operating on the $D_2$ line of $^{39}$K. The first laser is the master laser, which provides a frequency reference for the other two lasers. The master laser frequency is stabilised to the potassium spectrum using a magnetically-induced dichroism lock [61].

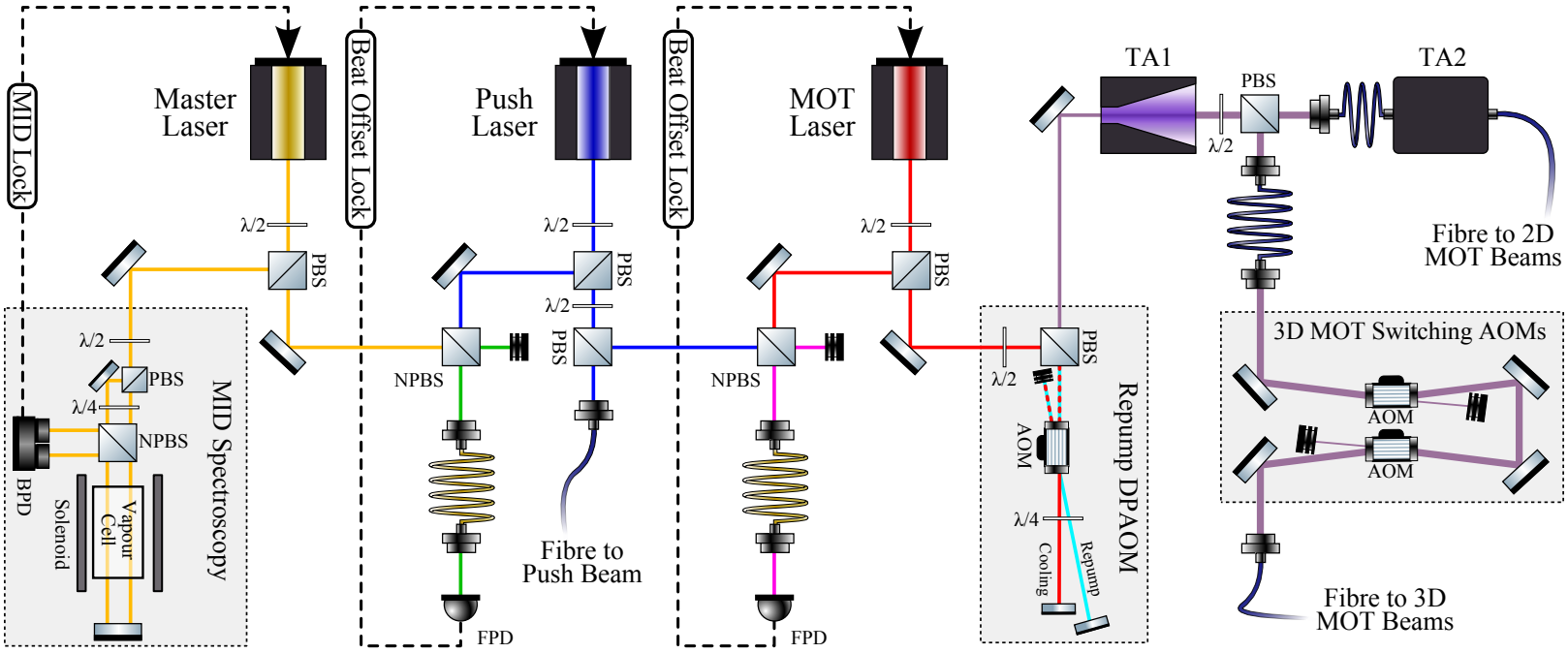


Figure 3.3: Simplified schematic of the laser system used to generate the pushing, 2D MOT and 3D MOT beams. Acronyms used are PBS (polarising beam-splitter), NPBS (non-polarising beam-splitter), FPD (fast photodiode), BPD (balanced photodetector), AOM (acousto-optical modulator) and TA (tapered amplifier).

The second laser is locked to the master using a beat-offset lock [62]. This laser is used as the pushing laser, which has the sole purpose of pushing the atoms from the 2D MOT into the 3D MOT. The third laser is beat-offset locked to the pushing laser and is used as the MOT laser, which provides the cooling and repump beams. The MOT laser operates at the cooling frequency, and the repump beam is generated from the repump double-pass acousto-optical modulator (DPAOM). Both cooling and repump beams are then amplified using tapered amplifiers (TAs) before being sent to the 2D and 3D MOTs.

It is often useful to pump the 3D MOT atoms into the $F = 1$ ground state before probing the cavity by completely switching off the repump light. This can be done by switching off the RF to the repump AOM. It is also useful to switch the 3D MOT beams on and off. This can be done by switching the 3D MOT switching AOMs. This pair of AOMs operate at the same frequency, with one increasing the frequency of the MOT beams, and the other decreasing the frequency by the same amount. In principal, the frequency of the 3D MOT beams could be tuned with respect to the 2D MOT beams using these AOMs, which may be a future avenue for optimisation for the system.

### 3.2.1 Magnetically-Induced Dichroism Spectroscopy Lock

A spectrum for standard Doppler-free saturation spectroscopy is shown in Figure 3.4(a). As the figure shows, there are not many features where locking is possible due to the small hyperfine splitting compared to the natural linewidth of the atoms. In order to generate frequencies useful for the MOT, it is useful to stabilise a 'master laser' using spectroscopy, and use more flexible beat-offset locks to generate the correct frequencies required for the MOT.

The method of spectroscopy used to lock the master laser is a form of magnetically-induced dichroism spectroscopy. A solenoid wrapped around the vapour cell creates a longitudinal magnetic field, which causes the hyperfine levels of the atom to split according to their $m_F$, due to the Zeeman effect. Two probe beams are used to probe the vapour cell, each polarised circularly, with opposite handedness. Since the longitudinal magnetic field is in place, these polarisations correspond to $\sigma^+$ and $\sigma^-$ polarisations. These beams are then retro-reflected to form a type of Doppler-free spectroscopy. Each of these probes are then measured on separate photodiodes of a balanced photodetector, which outputs the difference signal between each photodiode.

In the case of zero magnetic field, the $\sigma^+$ and $\sigma^-$ probes experience the same absorption and the difference signal is zero. As the magnetic field strength is increased, the $m_F$ levels

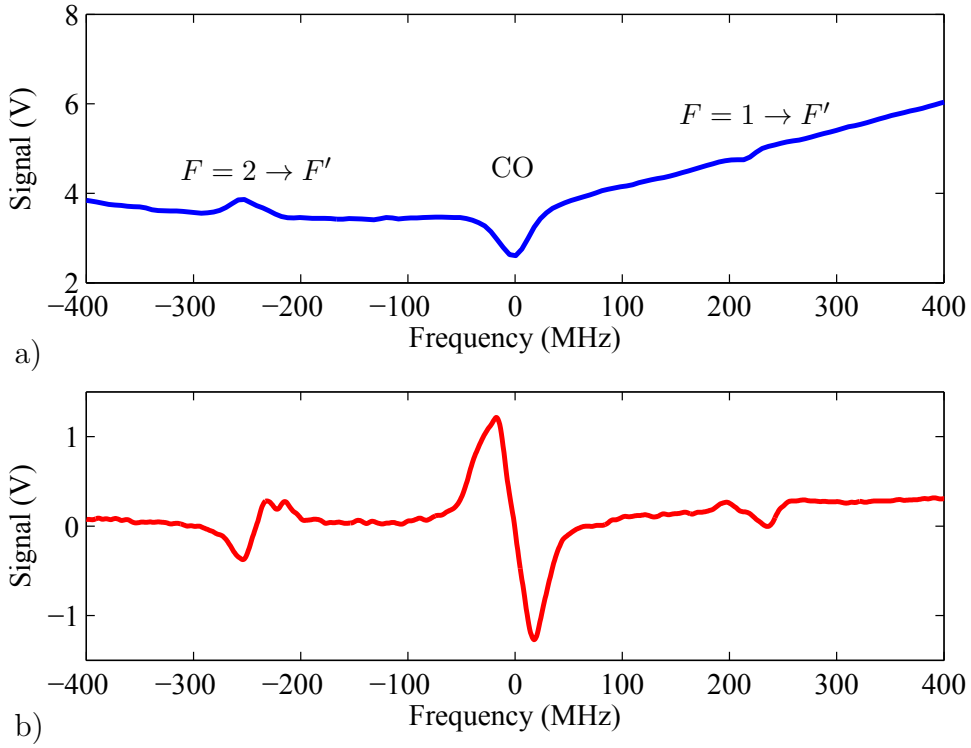


Figure 3.4: (a) shows the Doppler-free saturated absorption spectroscopy of the potassium $D_2$ line. The leftmost of the three main features corresponds to the $F = 2 \rightarrow F' = 1, 2, 3$ transitions, the rightmost corresponds to the $F = 1 \rightarrow F' = 0, 1, 2$ transitions, and the central feature is the crossover (CO) between the six transitions. The probe absorption is enhanced at the crossover due to hyperfine pumping between the two ground states. (b) shows the error signal obtained from the magnetically-induced dichroism method.

split, with positive $m_F$ levels increasing in energy and negative $m_F$ levels decreasing in energy. This causes the $\sigma^+$ and $\sigma^-$ absorption spectra to shift in frequency in opposite directions, and thus a dispersive signal is created at the difference signal, as shown in Figure 3.4(b). For a good error signal to be obtained, the Zeeman splitting should be comparable to the width of the spectral feature.

In this experiment, the master laser is locked to the ground state crossover feature, where $F, |m_F| = 1 \rightarrow F', |m'_F| = 2$ and $F, |m_F| = 2 \rightarrow F', |m'_F| = 3$ are the dominant transitions. With the solenoid producing a field of 14 G, the corresponding Zeeman shifts for these transitions are 19 MHz and 35 MHz respectively, which are both comparable to the width of the crossover feature. This provides a lock with a large capture range, and a lock stability of approximately 0.80 MHz. This is most likely limited by the poor bandwidth of the feedback electronics.

### 3.2.2 Beat-Offset Locking

The push and MOT lasers are frequency stabilised to the master laser using a method known as beat-offset locking [62]. This method works by beating two lasers together and stabilising the beat note between them to a desired value. This method is very flexible, since the desired beat note can be specified using an arbitrary reference frequency.

As can be seen from Figure 3.3 and 3.5, a beat note $\omega_B$ between the two lasers is established by coupling both beams into a single mode fibre to maximise spatial overlap. This light is then sent to a fast photodiode, which has a high bandwidth. The photodiode signal is mixed with the reference frequency $\omega_R$, to create signal components oscillating at $|\omega_B \pm \omega_R|$. The high frequency component is filtered off using a low-pass filter (LPF) leaving only the low frequency component oscillating at $|\omega_B - \omega_R|$. This signal is then split into two separate arms. One arm is sent through a high-pass filter (HPF), which has a 3 dB point at $\omega_F$. After the HPF, the signal passes through a positive rectifier. The second arm contains a 3 dB attenuator and a negative rectifier.

When these two arms are added together, an error signal is produced, as appears in Figure 3.5. It can be seen that when $|\omega_B - \omega_R| = \omega_F$, the attenuation from both arms is the same, thus the error signal is equal to zero at four points. Two of these points occur at $\omega_B = \omega_R \pm \omega_F$, and two points occur at $\omega_B = -(\omega_R \pm \omega_F)$.

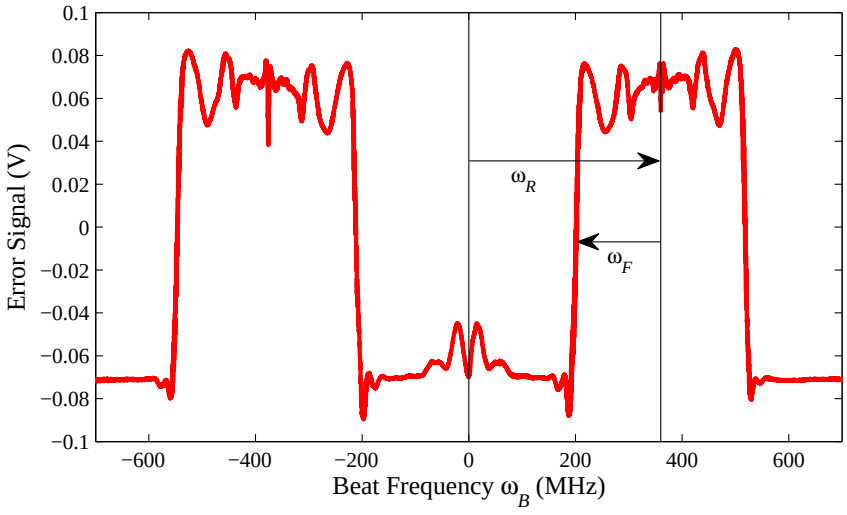


Figure 3.5: Error signal for the beat-offset lock between the master and pushing laser. The lock-point used is the zero-crossing around 205 MHz.

Using this method, the pushing laser is locked roughly to the vicinity of the repump transition, and the MOT laser is locked to the cooling frequency, with lock stabilities

of approximately 0.95 and 0.89 MHz respectively. The frequencies used to achieve these locks are summarised in Table 3.1.

| Beat-Offset Lock | Desired $\omega_B$ | HPF frequency $\omega_F$ | Reference frequency $\omega_R$ |
|---|---|---|---|
| Pushing to Master | +205 | 164 | 368 |
| MOT laser to Pushing | −450 | 164 | 286 |

Table 3.1: Summary of frequencies used in the beat-offset locks. All units are in MHz.

### 3.2.3 Repump AOM

The MOT laser stabilised at the cooling transition frequency, and then passes through a double-pass acousto-optical modulator (DPAOM) setup. The DPAOM operates around $+2 \times 227$ MHz, and generates light at the repump transition frequency. Unlike most DPAOM setups, the zeroth-order diffraction mode of the AOM is reflected back though the AOM, and overlapped with the doubly-shifted repump beam. This way, a beam containing both cooling and repump frequencies is generated.

As mentioned earlier, the intensity balance between cooling and repump beams is an important factor in potassium MOTs. This DPAOM setup allows some intensity control by changing the AOM efficiency with the driving RF power. For an incident beam with intensity $I_0$ diffracting with single-pass efficiency $\epsilon$ into the first diffraction order, the power in the cooling and repump of the combined beam after the DPAOM will be,

$$I_C = (1-\epsilon)^2 I_0 \quad \text{and} \quad I_R = \epsilon^2 I_0 \,,$$

and so the DPAOM single-pass efficiency $\epsilon$ is deliberately set to around 45%, to give a cooling-repump ratio of around 3:2. This method is inefficient in that a fraction of $2\epsilon(1-\epsilon)$ of the incident optical power is wasted at the AOM; however the combined cooling-repump beam is sent to a tapered amplifier for amplification, and so the power here is not important provided that the optical power is high enough to saturate the tapered amplifier. Furthermore, alternative methods of overlapping two beams so that they share the same polarisation always come at the cost of efficiency. A non-polarising (50:50) beam splitter, for example is less efficient than our DPAOM setup.

The RF can also be turned off completely, to direct all power into the cooling beam, which is useful for pumping the atoms in the MOT into the $F = 1$ ground state, which is where the cavity-atom system is probed.

### 3.2.4 Light Amplification System

Once a beam containing both repump and cooling frequencies is obtained, the total beam power is only around 10 mW. This optical power is insufficient for laser cooling [63], and thus amplification is required. The amplification is done using two tapered amplifiers (TAs).

Firstly, the beams from the repump DPAOM are amplified using a home-built TA system, using an M2K TA-0765-100043 chip. The design of this TA system is detailed in Komal Pahwa's thesis [60]. From here, the light is divided for use at the 2D MOT and the 3D MOT.

The output beam from the home-built TA occupies a variety of high-order spatial modes, which can be difficult to align with. For this reason, it is helpful to couple the 3D MOT beam through a single mode polarisation-maintaining (PM) fibre to filter off these high-order modes, leaving only the $TEM_{00}$ mode. This beam is then passed through a pair of AOMs, both operating at 110 MHz, the first shifts the light into the +1 diffraction mode, and the second shifts the light into the -1 diffraction mode, resulting in zero net frequency shift. The 3D MOT light can then be switched on and off using these AOMs, with a switching time of 250 ns. After the switching AOMs, the light is coupled into two PM fibres for the vertical and horizontal beams for the 3D MOT. This setup provides roughly 15 mW per 3D MOT beam.

Since the 2D MOT requires significantly more optical power than the 3D MOT, the 2D MOT light is passed through to a second fibre-coupled commercial TA (New Focus TA-6713-P) which provides 100 mW per beam at the 2D MOT.

This method of amplifying both repump and cooling beams together is limited by the fact that the home-built TA is very sensitive to alignment, and so correctly overlapping the beams from the repump AOM is critical. To check that both beams are being amplified correctly, the MOT beam fibres can be injected into a fibre ring resonator, which can be used to spectrally analyse the light and confirm that both repump and cooling frequencies are present, and occur with the desired intensity ratios.

## 3.3 Vacuum System

Collisions between MOT atoms and the background gas lead to heating and loss of atoms from the MOT. For this reason, it is not possible to create a MOT at atmospheric

pressure, and so the experiment takes place inside an ultra-high vacuum (UHV) system. The vacuum system is shown in Figure 3.6 and has been updated from the the original design (discussed in References [59, 60]) in order to eradicate the problem of the cavity mirrors becoming dirty from dispenser usage (discussed in Section 5.2.1). The new setup loads the 3D MOT from a 2D MOT, as opposed to loading directly from the background pressure produced by the potassium dispensers.

The potassium dispensers are located near to the 2D MOT chamber. This 2D MOT chamber consists of a six-way cross and four viewports. These viewports allow optical access for the two pairs of 2D MOT beams. The pushing beam is shone through a fifth viewport, onto the 2D MOT, which causes the atoms to be pushed along the direction of the pushing beam, and an atomic beam is formed. This atomic beam is directed along a graphite tube into the science chamber. The science chamber has eight viewports, six allowing access for the three pairs of orthogonal MOT beams, and two for coupling light into and out of the cavity. Once the atomic beam emerges from the graphite tube, it continues to travel into the 3D MOT capture region, where the 3D MOT is formed. The system has been designed so that the 3D MOT region spatially overlaps with the cavity mode. Small adjustments to the position of the 3D MOT can be made by adjusting the alignment of the 3D MOT beams and the position of the 3D magnetic field. The science chamber is pumped by an Agilent Starcell ion pump, which has a pumping rate of $20\,\mathrm{L\,s^{-1}}$.

### 3.3.1 Potassium Dispensers

The dispensers used in this experiment are K/NF/4.5/25/FT10 dispensers available from SAES Getters. These dispensers are trapezoidal strips encasing potassium salt and reducing agent. These salt-based dispensers were chosen over a purer ampoule-based solution in order to reduce the complexity of the vacuum system.

The strips are connected to an electrical feed-through (as shown in Figure 3.7) and are heated by passing a current of 5 A through them. As the strips heat up, the metal casing expands and a narrow slit opens up, allowing potassium to evaporate into the vacuum. These slits are directed towards the inner walls of an extension nipple. This nipple and the dispenser cross (15 and 16 on Figure 3.6) are heated from the outside using a flexible silicon heating strip to prevent the potassium from condensing before it reaches the 2D MOT region.

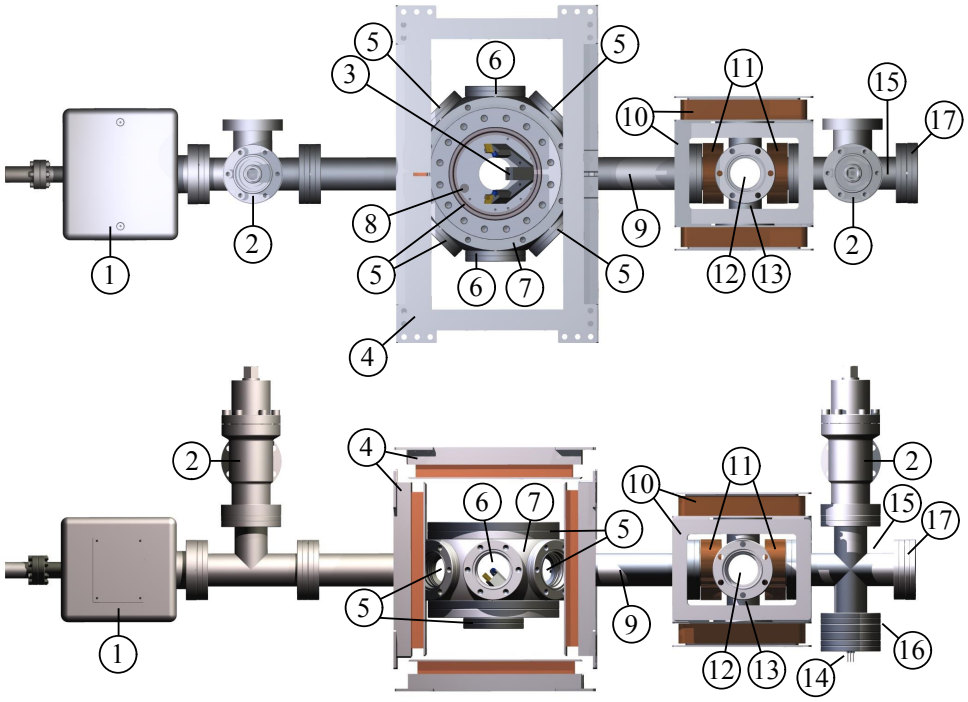


(a) Top view and side view.

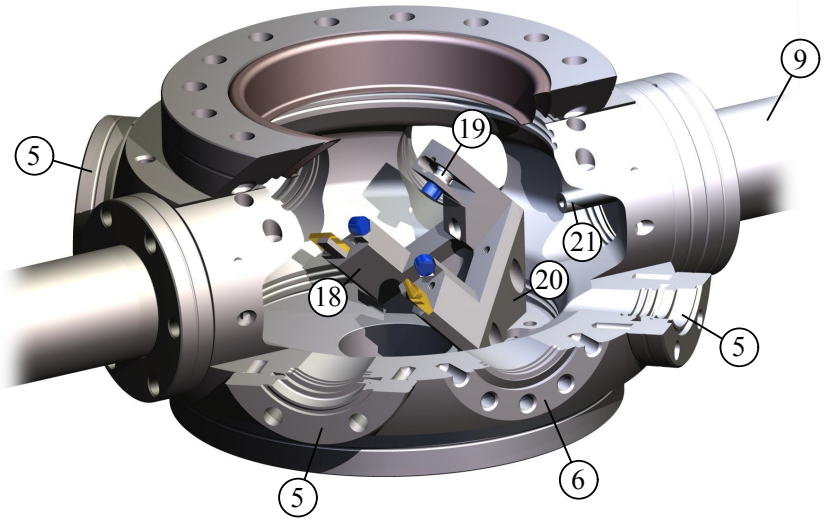


(b) Cutaway view of science chamber.

Figure 3.6: The layout of the vacuum system.(1) Ion Pump, (2) Valve, (3) Cavity, (4) 3D MOT coils, (5) 3D MOT viewports, (6) Cavity input/output viewports, (7) Science chamber, (8) Cavity piezo feed-through, (9) Nipple housing graphite tube, (10) 2D MOT coils, (11) 2D MOT correction coils, (12) 2D MOT viewport, (13) Six-way cross used for 2D MOT chamber, (14) Dispenser feed-through, (15) Dispenser cross, (16) Dispenser extension, (17) Push beam viewport, (18) Cavity frame, blue mirrors are cavity mirrors, gold mirrors are steering mirrors, (19) Flexure mount with piezo and ceramic spacers, (20) 45° wedge piece, (21) Steel pipe housing graphite tube.

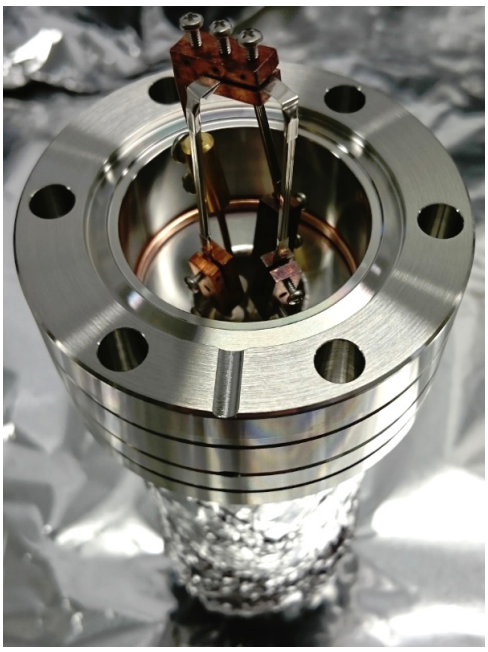

Figure 3.7: Photograph of dispensers. The dispensers are connected to an electrical feed-through using custom-built copper screw terminals.

### 3.3.2 The Graphite Tube

The graphite tube (purchased from GoodFellow) is 10 cm long, with outer and inner diameters of 6 mm and 3 mm. This tube has a very low vacuum conductance, and was chosen to keep the pressure in the science chamber as low as possible. The primary intention of keeping the science chamber pressure low is to keep the cavity mirrors as clean as possible, but a low pressure is also beneficial for reducing collisions between background gas and atoms in the MOT, and thus extending the 3D MOT lifetime and atom number. The tube is held in a 12 cm steel pipe welded into a modified Kurt J. Lesker double-blank DN40CF flange. To avoid machining the delicate graphite tube, the tube is held in place using a steel split-cylinder retainer.

### 3.3.3 The Cavity-Mounting Flange

The cavity is mounted onto a modified Kurt J. Lesker zero-length DN100CF-DN40CF reducer flange. The modifications include the addition of an electrical feed-through for the piezo and three tapped holes for mounting the cavity frame. There are additional tapped holes for metal straps, to restrict movement of the piezo wires. Figure 3.8 shows

the cavity, mounted on the mounting flange. The piezo wires attach to the feed-through using copper screw terminals.

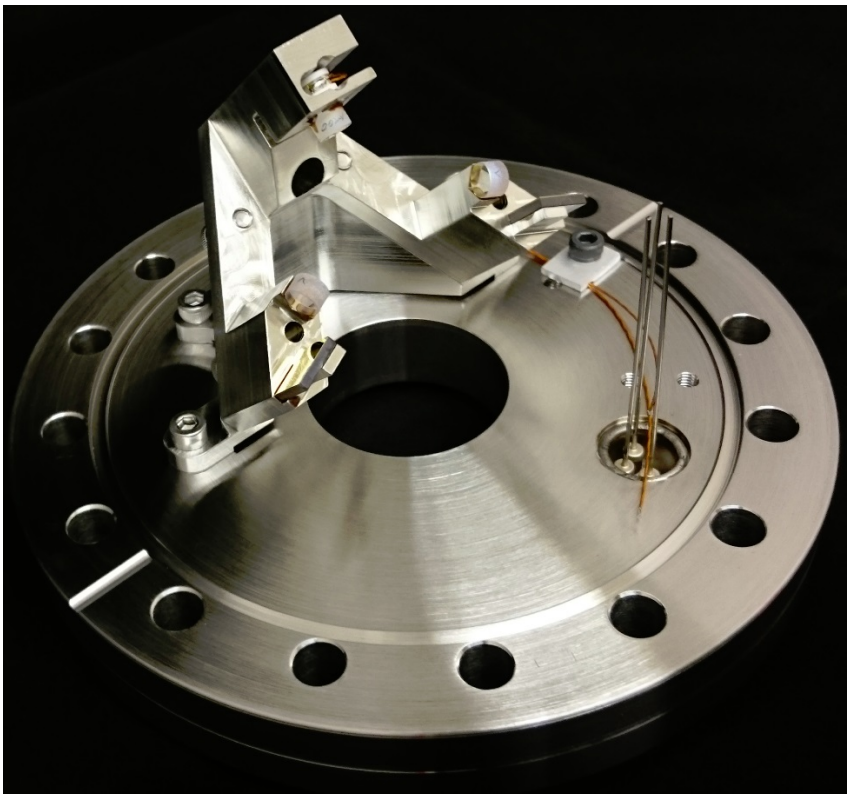

Figure 3.8: Photograph of the cavity mounting flange.

### 3.3.4 Estimating the Pressure in Each Chamber

In order to have some estimate of the pressure difference between the science chamber and the 2D MOT chamber, it is necessary to consider a vacuum conductance calculation [64]. The vacuum throughput $Q$ is proportional to the mass flow rate. Since our vacuum system only has one pump, the vacuum throughput will have the same value throughout all parts of the vacuum system. From Figure 3.9, the throughput at the pump will be,

$$Q = S_0 P_0 \,, \tag{3.1}$$

where $P_0$ is the pressure measured at the pump, and $S_0$ is the pumping speed of the pump. This pump is connected to the science chamber by two straight nipples. The throughput here is given by

$$Q = C_1 \left( P_1 - P_0 \right) , \tag{3.2}$$

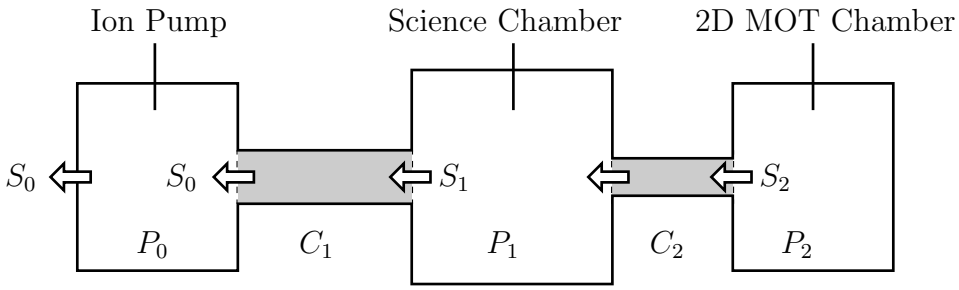


Figure 3.9: Symbolic representation of vacuum system for vacuum conductance calculation. Grey sections represent conducting tubes of vacuum conductances $C_{1,2}$ which connect the three main regions of the vacuum system which have pressures $P_{0,1,2}$.

where $P_1$ is the pressure in the science chamber, and $C_1$ is the vacuum conductance of the nipples. This vacuum conductance is analogous to electrical conductance, and tubes with low vacuum resistance will have high vacuum conductance. At low vacuum pressures, vacuum dynamics operate in the molecular-flow regime. In this regime, the vacuum conductance $C$ of a cylinder of inner diameter $D$ and length $L$ (in centimetres) is given by [65]

$$C = \frac{D^3 \bar{v}}{L} \times 2.6 \times 10^{-4} \mathrm{L\,s^{-1}}\,, \tag{3.3}$$

where $\bar{v}$ is the mean atomic velocity. For $^{39}$K at room temperature, $\bar{v} \approx 4 \times 10^4 \mathrm{cm\,s^{-1}}$. For these nipples, the diameter $D$ is 3.5 cm and the total length $L$ is 25 cm, leading to a vacuum conductance $C_1$ of roughly $18\,\mathrm{L\,s^{-1}}$. The conductivity of the science chamber will be neglected, since it has a very large relative diameter. The vacuum throughput at the science chamber will be

$$Q = S_1 P_1\,, \tag{3.4}$$

where $S_1$ is the volume flow rate at the science chamber. Equating Equations 3.1 and 3.2, it can be seen that for a pump rate $S_0$ of $20\,\mathrm{L\,s^{-1}}$,

$$\frac{P_1}{P_0} = \frac{S_0 + C_1}{C_1} \approx 2\,, \tag{3.5}$$

and so the pressure in the science chamber is roughly two times higher than the pressure measured at the ion pump. Using this result with Equations 3.1 and 3.4 gives that $S_1 \approx S_0/2$. The vacuum throughput at the graphite tube will be

$$Q = C_2 \left(P_2 - P_1\right)\,, \tag{3.6}$$

where $P_2$ is the pressure at the 2D MOT chamber. $C_2$ can be calculated using Equation 3.3, and with a length of 10 cm and diameter 0.3 cm, $C_2$ is roughly $2.8 \times 10^{-2} \mathrm{L\,s^{-1}}$.

The vacuum throughput at the 2D MOT chamber will be given by

$$Q = S_2 P_2 \,, \tag{3.7}$$

and equating Equations 3.6 and 3.7, and using that $S_1 \approx S_0/2$,

$$\frac{P_2}{P_1} = \frac{(S_0/2) + C_2}{C_2} \approx 340 \,, \tag{3.8}$$

and so it can be seen that by using the graphite tube, the pressure in the science chamber will be kept at much lower pressures than the 2D MOT chamber and is indeed significantly isolated from the potassium dispensers. This is advantageous in that it should help keep the cavity mirrors clean, however, it also means that the 2D MOT chamber is also significantly isolated from the ion pump, and the pressure in the 2D MOT chamber is limited by $P_2/P_0 \approx 700$. Ideally, we would use ion pumps on both sides, but due to financial limitations, this was not possible at the time of construction. In practice, the only pressure measurable to us is $P_0$ using the ion pump. The pressure readout here is usually below detection threshold, which is around $10^{-10}$mbar.

### 3.3.5 Vacuum Pump-Down and Bakeout

Once the Vacuum system was assembled, the system was pumped down and baked. The system was pumped down from both the science chamber side and the 2D MOT side, by connecting a turbo pump to both valves in the system. These valves were positioned so that each is either side of the graphite tube, allowing both sides of the chamber to be pumped down directly. The vacuum system was baked at 150 °C for two weeks. The pressure and temperature profile of this bake is shown in Figure 3.10.

## 3.4 Magnetic Field System

In order to generate a spatially-dependent trapping force, a magnetic quadrupole is required. This experiment requires two magnetic quadrupoles, one for each 2D and 3D MOT. Each quadrupole is generated by a set of four rectangular coils, as shown in Figures 3.6 and 3.11.

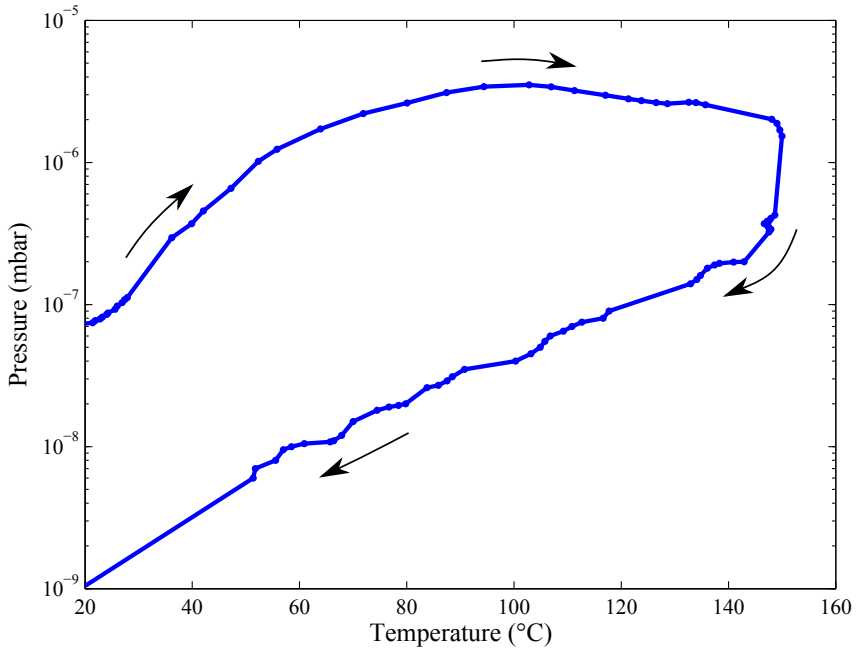


Figure 3.10: Pressure and temperature of the vacuum system over the course of the two week long bakeout. The bakeout improved the pressure by two orders of magnitude.

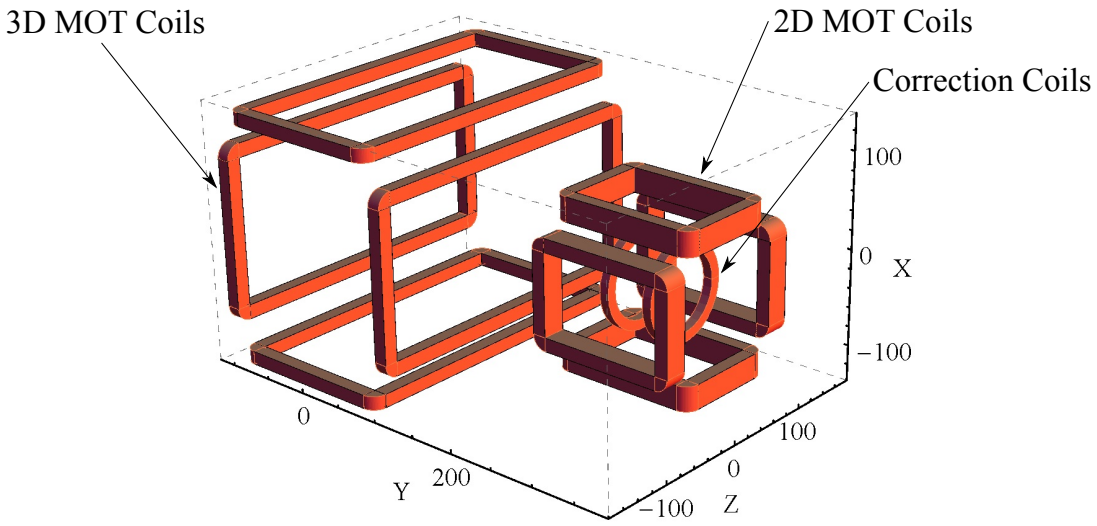


Figure 3.11: Geometry of magnetic coils used in the experiment. In total, three sets of coils are used. One set is used for each 2D and 3D MOT, whilst the third coil removes the field created by the 3D MOT coils at the position of the 2D MOT.

### 3.4.1 Magnetic Field Geometry of the 2D MOT

The magnetic field geometry for the 2D MOT is a two-dimensional quadrupole field generated by four rectangular coils. This field geometry creates a line of zero magnetic field along the longitudinal axis of the coil setup ($y$-axis), creating an axis along which atoms can be cooled and trapped. The two pairs of MOT beams are orthogonal to this axis.

Each coil has 222 turns and creates a gradient of $4\,\mathrm{G\,cm^{-1}}$ per amp. Since these coils are not cooled, the current in the coils is limited to 2.5 A, creating a total gradient of $10\,\mathrm{G\,cm^{-1}}$ at the 2D MOT region.

### 3.4.2 Magnetic Field Geometry of the 3D MOT

Since this experiment is concerned with overlapping the MOT atoms with the cavity mode, we have somewhat unconventionally chosen to use a two-dimensional magnetic quadrupole rather than a three-dimensional quadrupole to create the 3D MOT [66]. The 2D magnetic quadrupole has a line rather than a point of zero magnetic field and thus creates a cigar-shaped atomic cloud rather than the roughly spherical cloud generated by a three-dimensional quadrupole. This is potentially beneficial, since if the cloud is elongated along the cavity axis, more atoms can be overlapped with the cavity mode. In practice however, we did not find elongation to be advantageous.

This setup differs from a 2D MOT setup in that there are three pairs of orthogonal beams, rather than just two. In a regular, four-beam 2D MOT system, the two effects which result in magneto-optical trapping (Doppler cooling and spatially-dependent trapping) are only present in two directions. The inclusion of the third pair of orthogonal beams introduces Doppler cooling in the third direction, which is enough to form a stable 3D trap. This setup also differs from a standard six-beam 2D MOT in that two of the orthogonal beam pairs are incident at 45° to the longitudinal axis of the magnetic field. The reason for this is that it allows optical access to the longitudinal axis of the MOT, which is required for the cavity probe beam. It is believed that this unconventional 45° angle of incidence is not required to maintain a stable trap [66].

The field is generated from four rectangular coils wound onto hollow copper frames, which are water-cooled. Each coil is made from 40 turns, and generate $0.3\,\mathrm{G\,cm^{-1}}$ per amp. The coils are connected in series and are driven using a single current supply. The coils are operated at 30 A, creating $9\,\mathrm{G\,cm^{-1}}$ at the centre of the 3D MOT. The simulated

magnetic field along each axis is shown in Figure 3.12, it can be seen that the magnetic field gradient generated along the axis of the cavity is small, and thus elongation is expected along this axis.

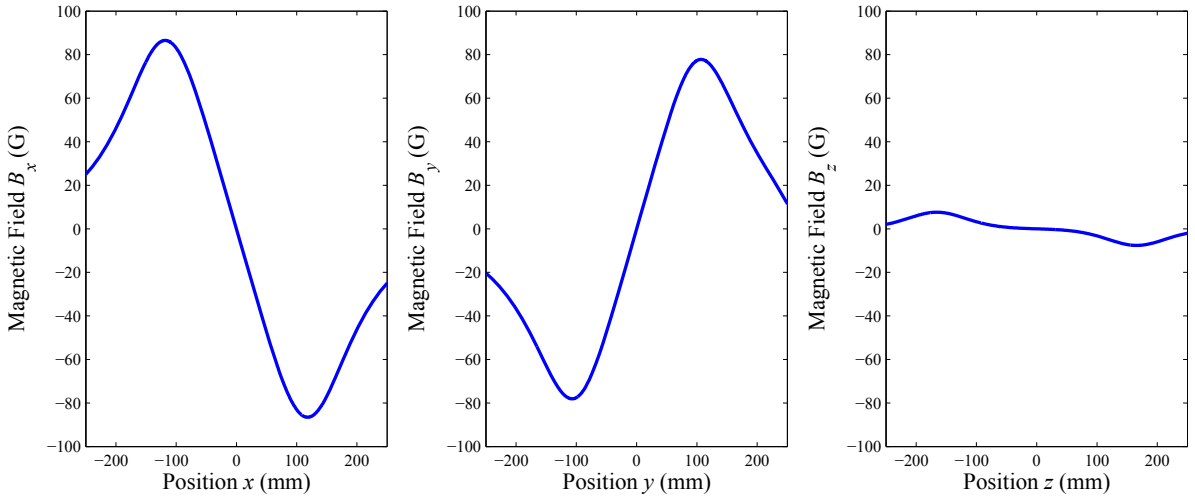


Figure 3.12: Magnetic field components along each axis. With the geometry shown in Figure 3.11, $z$ is the axis which is along the cavity mode, and in the direction that MOT elongation is expected.

Due to reasons discussed in Section 4.2.5, these coils have recently been replaced with more conventional anti-Helmholtz style coils, generating a three-dimensional magnetic quadrupole field, however all results in this thesis were generated using these elongated coils.

### 3.4.3 Correction Coils

Due to the large physical size of the 3D MOT coils, the magnetic field created by these coils extends over a relatively large distance. This creates a problem at the 2D MOT whereby the longitudinal magnetic field is non-zero due to components from the 3D MOT coils. For this reason, it was not possible to create a 2D MOT without the addition of a third set of 'correction' coils. These correction coils are wound around the six-way cross as shown in Figure 3.6, and create a magnetic field along the $y$ axis which cancels out the problematic field from the 3D MOT coils. Each coil consists of 20 turns and operate at 1.05 A and 0.45 A.

These correction coils were designed and simulated using Radia[1], and the results are

[1]Radia is a free software developed by the European Synchrotron Radiation Facility which interfaces with Mathematica [67]

plotted in Figure 3.13. The simulation shows that without the correction coils, the magnetic field at the centre of the 2D MOT is 11.5 G, which can be reduced to effectively zero with a relatively flat gradient when the correct correction coil currents are used. The correction coils are small and thus the field created by these coils is very small at the position of the 3D MOT.

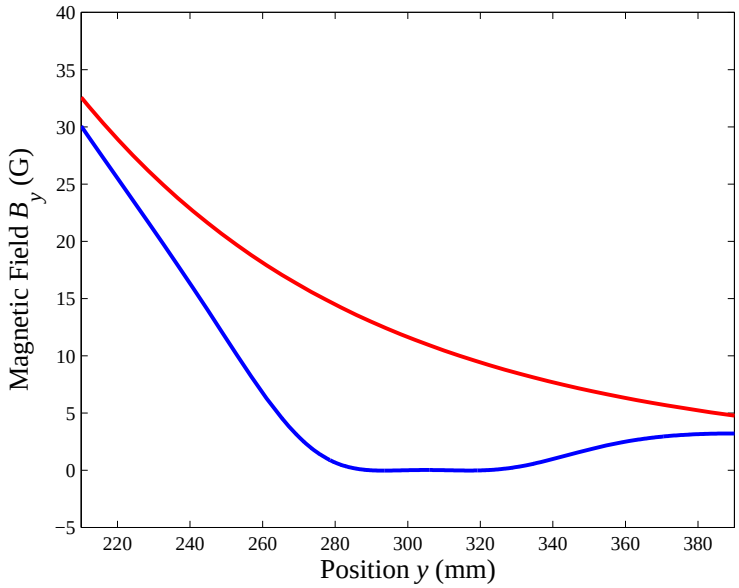


Figure 3.13: Simulated results for the longitudinal magnetic field $B_y$ at the 2D MOT. The centre of the 2D MOT lies at $y = 300$ mm. The blue and red curves indicate the field with and without the correction coils.

CHAPTER 4

# Measurements and Characterisation of the $^{39}$K MOT

## 4.1 Procedure for Measuring the Number of Atoms

To measure the number of atoms, a fluorescence image of the MOT is taken and the number of atoms is inferred. The number of atoms $N_a$ can be related to the number of photons $N_p$ detected at the camera during an exposure time of $t_{exp}$ by,

$$N_a = \frac{N_p}{R \cdot t_{exp} \cdot (d\Omega/4\pi)}, \tag{4.1}$$

where $R$ is the fluorescence rate per atom and $d\Omega/4\pi$ is the fractional solid angle being sampled by the camera.

Obviously, the number of photons cannot be measured directly. The camera will convert the photon number $N_p$ to pixel values (or 'counts') $N_c$. These quantities are be related by a calibration constant $\eta$,

$$\eta = \frac{N_c}{N_p}. \tag{4.2}$$

The fractional solid angle was estimated using,

$$\frac{d\Omega}{4\pi} \approx \frac{1}{4}\left(\frac{r}{d}\right)^2, \tag{4.3}$$

where $r$ is the radius of the lens aperture and $d$ is the distance from the camera lens to the MOT.

### 4.1.1 Fluorescence Rate and the Six-Level Model

The final quantity to be understood is the fluorescence rate $R$ per atom in the MOT. For most alkali metals used in cold atom experiments, a two-level model of the atom is usually adequate to deduce $R$ [68]. In potassium however, the narrow hyperfine splitting of the $D_2$ line means that the two-level atom is inadequate, and a full six-level model must be used. Williamson has an excellent description of this six-level model in his thesis [69], which can be used to deduce the steady-state population fraction for each level for given cooling and repump powers and detunings. A brief outline of this model is given in Appendix B, along with the relevant strength coefficients and branching ratios for $^{39}$K.

In Figure 4.1, the excited state fraction is obtained from simulations of the six-level model for a variety of total intensities and cooling-repump ratios. In this simulation, the detunings of the repump and cooling beams were set to the values used in the experiment ($-18$ and $-27$ MHz respectively).

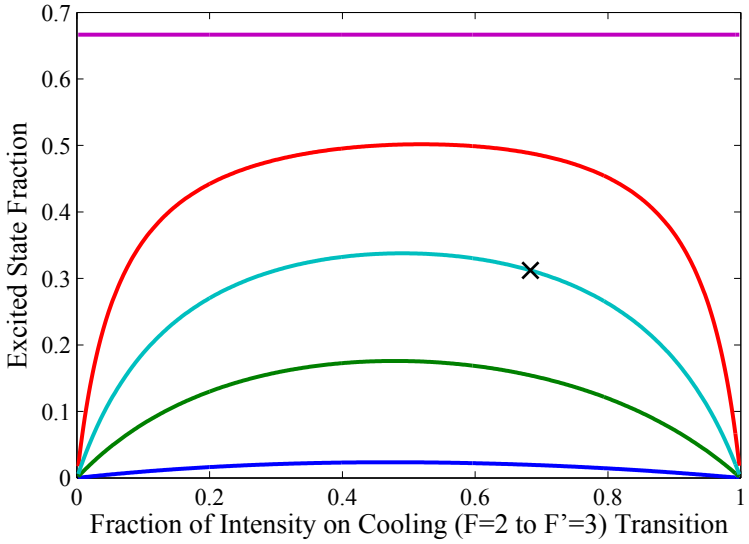


Figure 4.1: Excited state fractions obtained from the six-level model, plotted for total intensities of $(1, 10, 30, 100$ and $\infty)$ saturation intensities (blue, green, cyan, red and pink). The detunings used here are $-18$ and $-27$ MHz for the repump and cooling beams. The black cross shows where this experiment operates.

In the limit of infinite total intensity, all levels become equally populated, and so the maximum excited state fraction becomes $2/3$, rather than the more-familiar value of $1/2$ obtained from the two-level model. At the intensities used in our experiment, the excited state fraction is usually around 0.3.

Once the excited state fraction $f_{ex}$ has been estimated, the expected fluorescence rate will be,

$$R = f_{ex}\Gamma\,, \tag{4.4}$$

where $\Gamma = 2\pi \cdot 6.035\,\mathrm{MHz}$ is the natural linewidth of $D_2$ line [58].

### 4.1.2 Fitting the MOT Image

The camera used in this experiment is a Pike F-145B from Allied Vision Technologies. It observes the MOT from the large viewport on the top-side of the science chamber. The camera views the MOT along a line perpendicular to the axis of zero magnetic field created by the 3D MOT coils.

The image of the MOT is fit to a 2D Gaussian using Matlab,

$$I(y,z) = A \cdot \exp\left\{ \frac{\left[(y-y_0)\cos\theta - (z-z_0)\sin\theta\right]^2}{2\sigma_y^2} + \frac{\left[(y-y_0)\sin\theta + (z-z_0)\sin\theta\right]^2}{2\sigma_z^2} \right\}, \tag{4.5}$$

where $A$ is the amplitude, $y_0$ and $z_0$ are the centroids, $\sigma_{y,z}$ are the RMS widths in each direction, and $\theta$ is the angular rotation of the MOT with respect to the image. From this, the total number of camera counts can be deduced and thus, the number of atoms in the MOT.

For each image of the MOT, a background image is taken with the magnetic field turned off, which is then subtracted from the MOT image. An example fit is shown in Figure 4.2.

## 4.2 Elongation of 3D MOT

As described in Section 3.4.2, in order to maximise the number of atoms inside the cavity, the 3D MOT uses a 2D quadrupole field rather than a more conventional 3D quadrupole. The intention is to achieve elongation of the MOT along the cavity mode, and potentially place more atoms inside the cavity.

In this section, the effects of magnetic field gradient and beam size on the aspect ratio of the MOT and estimated intra-cavity atom number are discussed. After this, the elongated

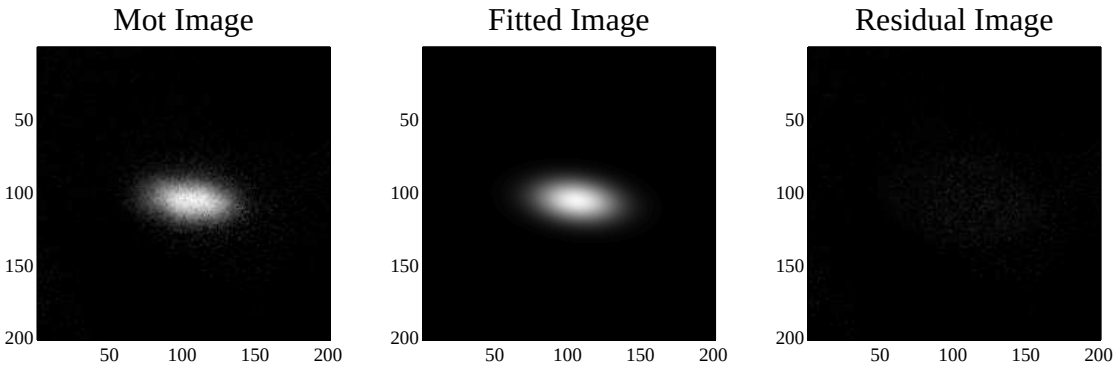


Figure 4.2: An example of MOT fitting. The image on the left has already undergone background subtraction.

four-coil setup is compared with an elongated two-coil setup (using the same coils, but removing two of them). The reason for the interest in the two-coil system is due to the unfortunate and significant thermal damage incurred by two of the coils when a problem with the water cooling system occurred. Although the coils are repairable, the elongated coils have been replaced completely for a conventional 3D quadrupole since my departure from the laboratory. The section will conclude by discussing the benefits and drawbacks of an elongated system, and explain our move towards a more conventional system.

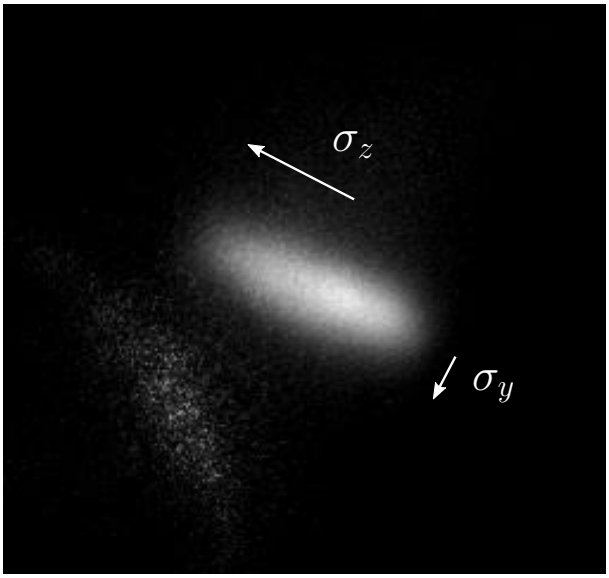


Figure 4.3: A photograph of an elongated MOT. The RMS widths $\sigma_{y,z}$ are shown. The $x$ direction is perpendicular to the page.

### 4.2.1 Estimating the Number of Atoms Inside the Cavity

An elongated MOT is shown in Figure 4.3. It can be seen that the width in one direction is significantly longer than the other. Using the analysis described earlier, the RMS sizes $\sigma_{y,z}$ for each direction can be found. There is obviously a third width $\sigma_x$ which cannot be measured from the 2D image, so we assume cylindrical symmetry around the axis of zero magnetic field, and hence assume that $\sigma_x$ and $\sigma_y$ are equal.

The number of atoms overlapping with the cavity mode can be estimated by taking the ratio between the cross-sectional areas of the cavity mode and MOT perpendicular to the zero-field axis. If the cavity mode is parallel to the zero-field axis, the number of atoms in the MOT multiplied by this ratio should be roughly equal to the number of atoms in the cavity,

$$N_{\text{cav}} = N_{\text{MOT}} \frac{A_{\text{cav}}}{A_{\text{MOT}}} = \frac{N_{\text{MOT}}}{4} \frac{w_x w_y}{\sigma_x \sigma_y}, \tag{4.6}$$

where the factor of 4 arises from comparing Gaussian RMS widths $\sigma_{x,y}$ to $1/e^2$ widths $w_{x,y}$. This method not only assumes that $\sigma_x$ and $\sigma_y$ are equal, but it also assumes that the zero-field axis and MOT are aligned and overlap perfectly with the cavity in all four degrees of freedom. Since we are not using the cavity in this section this is not an issue, however when the cavity is being used, alignment will be critical. For this reason, the estimated intra-cavity atom number given here is an upper-limit, which may be difficult to achieve in practice.

### 4.2.2 Elongation due to Magnetic Field Gradient

Measurements of the MOT were taken for a range of coil currents. The coil currents were converted into magnetic field gradient using a previous calibration. Since the experiment does not have a dedicated set of coils to compensate for the Earth's field, the experiment experiences significant difficulty when changes to the field strength of the coils are made. The coils were positioned and the 3D MOT beams were aligned such that movement of the centre of the MOT was minimal as the coil current was varied. Across the range, the total movement of the MOT centre was deduced to be 1.5 mm which is significantly smaller than the size of the MOT beams. The results are shown in Figure 4.4.

The results show that the MOT does not operate well below $5\,\text{G}\,\text{cm}^{-1}$, however as the field gradient increases beyond $8\,\text{G}\,\text{cm}^{-1}$, the total number of atoms in the MOT is affected negatively. The results also show that the aspect ratio can be doubled by increasing

the field gradient from 3 to 9 G cm$^{-1}$. The increased aspect ratio in turn, increases the estimated number of atoms in the cavity. At high field gradient, the negative effect on total MOT number and positive effect on aspect ratio appear to counteract one another, resulting in an optimal intra-cavity atom number at 9 G cm$^{-1}$.

### 4.2.3 Elongation Due to Beam Size

Irises were positioned in front of each 3D MOT beam, and the aperture size was varied. Images of the MOT were taken, and aspect ratio, total MOT number and the number of atoms in the cavity were estimated for each beam size. The results are shown in Figure 4.4.

The results show that there is a clear benefit for having larger beams. There is only a small improvement between the aspect ratio and the beam size, but there is a vast improvement in the number of atoms in the MOT, which benefits the number of intra-cavity atoms. No optimum was reached as the beam size is limited to 2 cm by the cavity frame.

### 4.2.4 Two-Coil Setups vs Four-Coil Setups

In addition to the four-coil configuration, two additional two-coil configurations were investigated. These two configurations are shown in Figure 4.5. In the first configuration, the coils were at the top and bottom of the chamber, and in the second configuration, the coils were placed either side. In each configuration, the separation of the coils was set to achieve maximum field gradients along $x$ and $y$. In the case of the top-bottom geometry, this was limited by the chamber size to be 110 cm. In the side-side geometry, this was set to be 85 cm.

The MOTs created by these field geometries are shown in Figure 4.6, and it was found that the aspect ratios achievable with each configuration were significantly different. The average aspect ratios achievable were 3.94, 1.94 and 5.14 for the four-coil, top-bottom and side-side geometries respectively.

A possible explanation for the different aspect ratios could be the difference in magnetic field gradients along the $z$ axis for each configuration. In the ideal four-coil configuration, the $x$ and $y$ magnetic field gradients are equal, and so the gradient in $z$ is zero. In the two-coil configurations, the $x$ and $y$ gradients are no longer identical, and thus a gradient

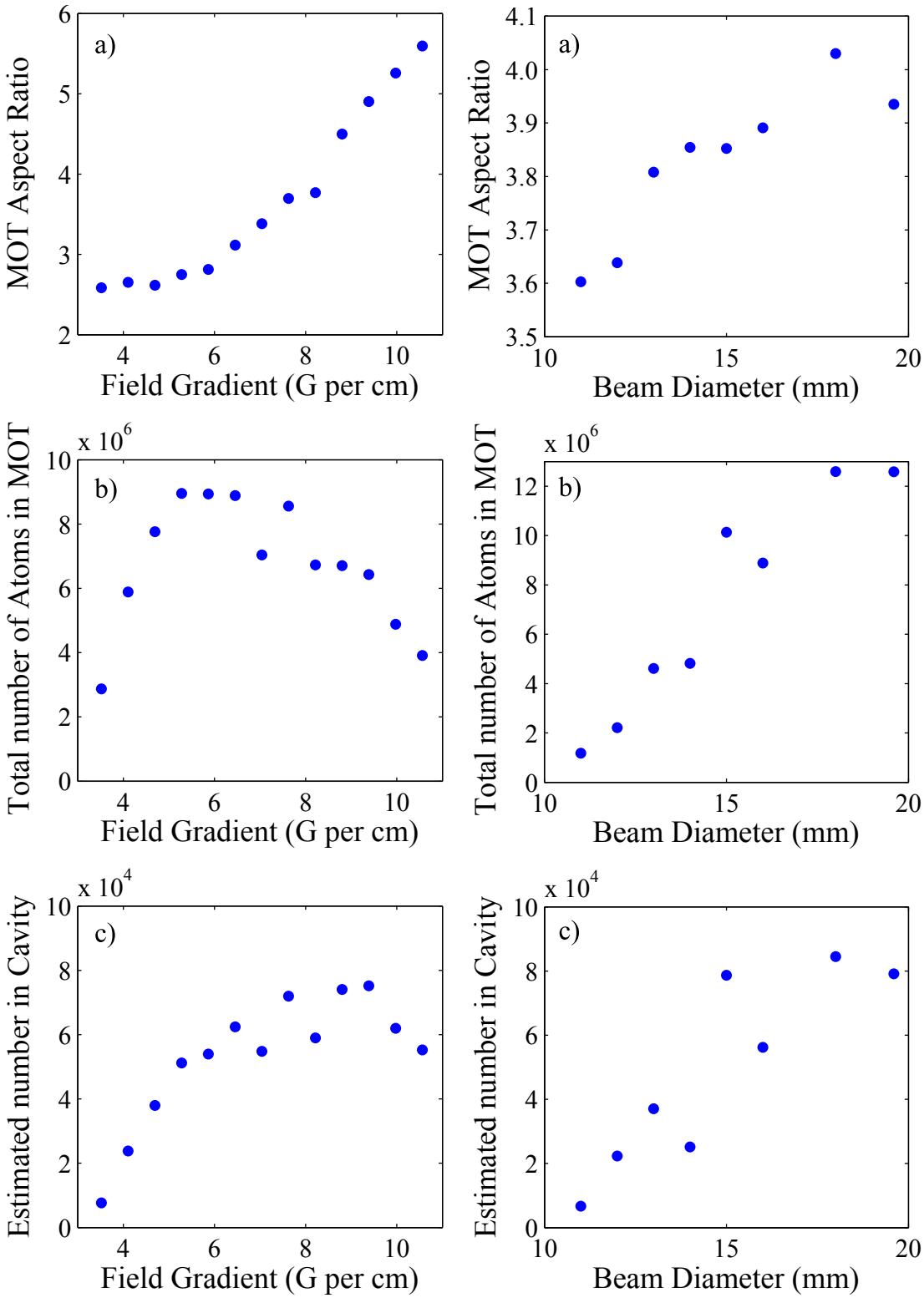


Figure 4.4: The effect of the field gradient (left) and 3D MOT beam size (right) on (a) the MOT aspect ratio ($\sigma_z/\sigma_y$), (b) MOT atom number and (c) estimated number of atoms in the cavity.

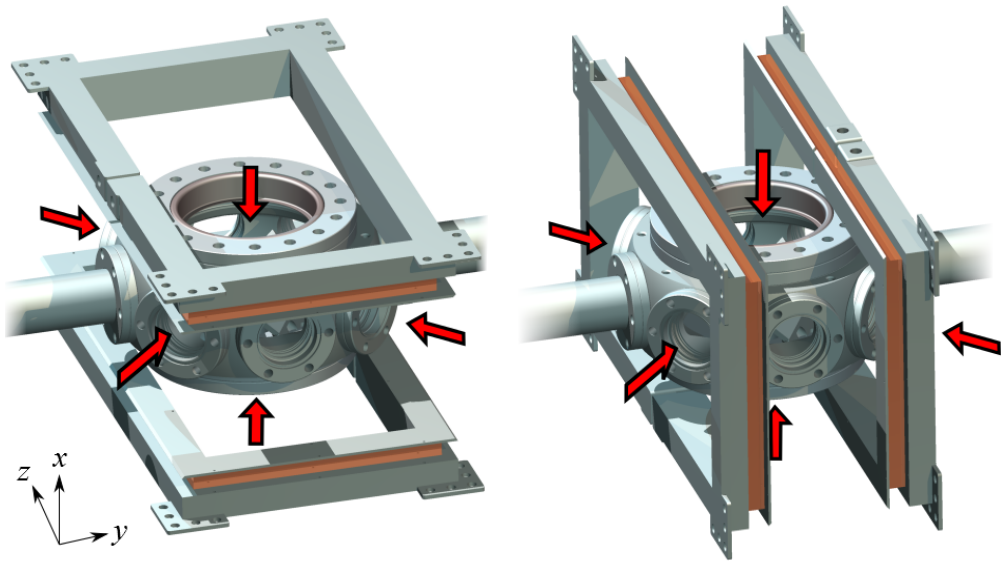


(a) Top-bottom configuration (b) Side-side configuration

Figure 4.5: Two-coil magnetic field configurations. Red arrows show positions of the 3D MOT beams. The cavity mode lies along the $z$ -axis.

| | Field Gradient G cm$^{-1}$ | |
|---|---|---|
| Axis | Top-Bottom | Side-Side |
| $x$ | $-9.13$ | $-8.29$ |
| $y$ | $+7.90$ | $+9.39$ |
| $z$ | $+1.24$ | $-1.10$ |

Table 4.1: Simulated magnetic field gradients for each two-coil configuration.

along $z$ arises. Simulated gradients along each axis for each configuration are summarised in Table 4.1.

It can be seen that the sign of the gradient along $z$ is opposite for each geometry. In a conventional MOT setup using a conventional 3D quadrupole, the sign of the $y$ and $z$ gradients should be identical to produce a restoring force along each direction. This is the case with the top-bottom configuration, and may explain why the aspect ratio is smaller for this configuration. In the side-side configuration however, the gradient along $z$ is opposite, which potentially causes a small amount of anti-trapping, causing the MOT to be elongated along this direction, increasing the aspect ratio of the cloud.

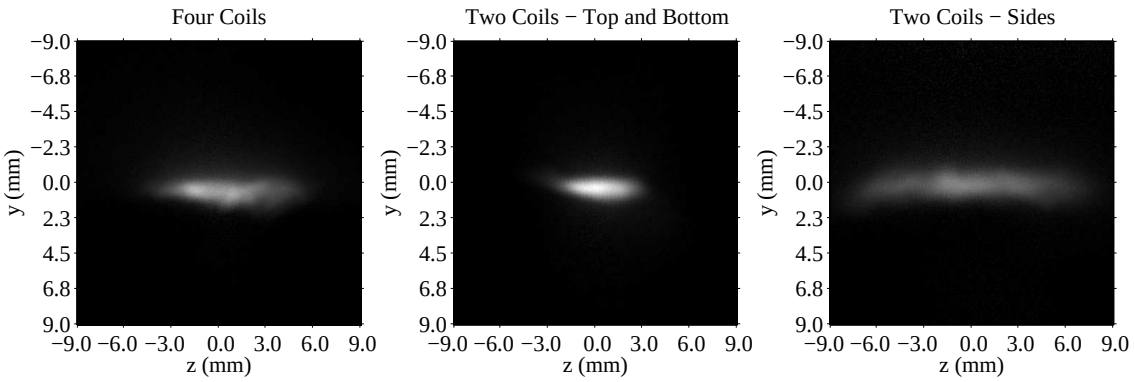


Figure 4.6: Images of the different MOTs created by each magnetic field configuration.

### 4.2.5 Conclusions on Elongation

It has been shown that the elongated field can potentially place more atoms into the cavity mode, however, there are concerns that the elongated field can potentially reduce the total number of atoms in the MOT. At the time of investigation, temperature measurements of the MOT were unavailable, and so no conclusions of the temperature can be drawn, but there is reason to believe that a conventional field geometry would produce lower temperatures.

Furthermore, the elongated MOT is significantly more difficult to overlap with the cavity mode, since it requires alignment in four degrees of freedom $(x, y, \theta_x, \theta_y)$, rather than the two degrees of freedom $(x, y)$ required with a non-elongated cloud.

For these reasons, the elongated coils were considered counter-intuitive and difficult to work with, and have been replaced with an anti-Helmholtz style geometry since my departure from the laboratory.

## 4.3 2D MOT Characterisation

In this section, optimisation of the loading rate from the 2D MOT into the 3D MOT is attempted. Firstly, the effects of 2D MOT beam intensity is considered, and secondly, the detuning of the pushing beam is considered.

### 4.3.1 Effects of Beam Intensity

The effects of the 2D MOT beam intensity on the loading rate of the 3D MOT was investigated. For this measurement, the intensity of each 2D MOT beam was set by mounting a polariser and quarter-wave plate together at a locked relative rotation of 45°. The polariser and quarter-wave plate were then rotated together to adjust the beam intensity, without changing the circular polarisation of each beam.

Using the computer control (described in Appendix A), the push beam shutter was opened and the camera was set to acquire at 10 Hz. From these images, the loading time was deduced. The final atom number after extrapolating the loading curve divided by the loading time gives the loading rate. The results are shown in Figure 4.7. It can be seen that the loading rate significantly improves with increased beam power, and the data show that we are far from being able to optimise this with the level of beam power available to us. This result agrees with those found in References [70] and [71].

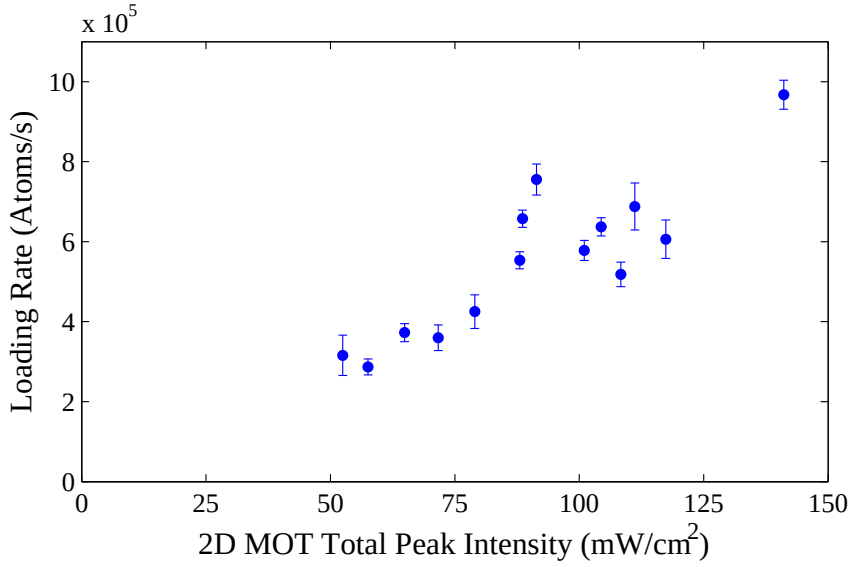


Figure 4.7: The effect of the total peak 2D MOT beam intensity (both pairs of orthogonal beams) on the 3D MOT loading rate. The error bars represent the standard error on a set of three loading rate measurements at each value of intensity.

### 4.3.2 Push Beam Detuning Optimisation

The effect of the push beam frequency on the total number of atoms in the 3D MOT was investigated. This involved changing the frequency of the VCO used in the beat-offset

lock between the master and the pushing laser. The VCO used in the lock between the pushing and MOT lasers was then changed also, to keep the frequency of the MOT beams unchanged. The results are shown in Figure 4.8.

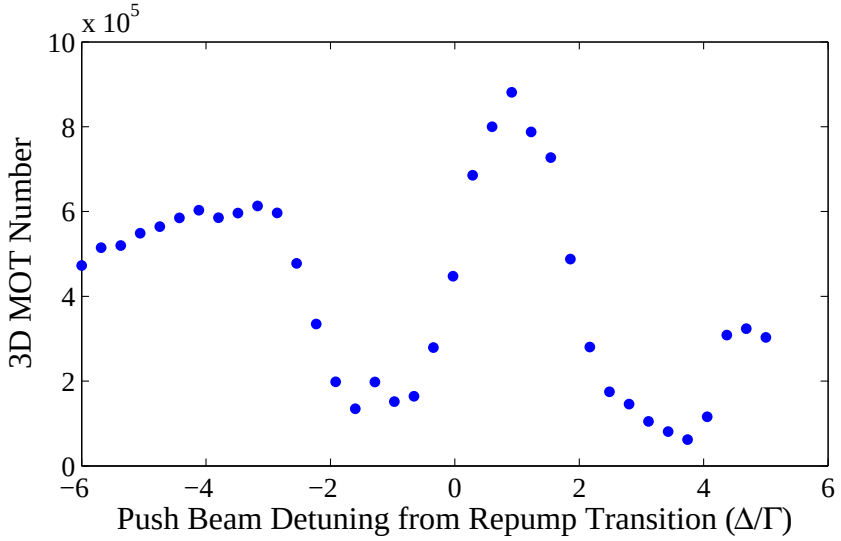


Figure 4.8: The effect of the push beam frequency on the total number of atoms in the 3D MOT. For this measurement, the push beam intensity was 24 W cm$^{-2}$ and was linearly polarised.

The results show that the pushing is optimal when the pushing frequency is approximately one natural linewidth blue-detuned from the repump transition. The pushing efficiency is also adequate at three natural linewidths red-detuned. In between these two peaks, there is a sharp dip in efficiency.

These results are not entirely understood but roughly agree with the results found in other potassium experiments [72, 73], and may partially be explained by the following considerations. A red-detuned pushing beam could improve the 3D MOT number by preventing atoms escaping the 2D MOT in the backward direction, thus the pushing beam acts as a kind of 'plug', only allowing atoms to leave the 2D MOT in a forward direction. A near-resonant beam could improve the 3D MOT by pushing any near-stationary atoms out of the 2D MOT cloud. And finally, a blue-detuned pushing beam could also improve the 3D MOT number by increasing the velocity of the already forward-moving atoms, which would reduce the divergence of the atomic beam, allowing more atoms to pass through the transfer tube without colliding with the walls of the tube. Also, the detuning of the pushing beam will roughly set the velocity of the atoms during the transfer. If the beam is too far blue-detuned, it is possible to push the atoms too quickly, whereby the atoms are travelling beyond the capture velocity of the 3D MOT. If the beam is too far

red-detuned, the atoms could be pushed too slowly, whereby a ballistic trajectory of the atoms between the 2D MOT and 3D MOT is not permitted by the transfer tube.

## 4.4 Measuring the Temperature

In order to probe the atom-cavity physics that we are primarily interested in, it is required that the 3D MOT beams are pulsed off during the cavity probing interval of the experiment. For this reason, it is necessary to know the temperature of the MOT, so that we can be assured that there is no significant change in atom number due to thermal expansion of the MOT whilst the cavity is being probed.

In this section, two temperature measurements are described and compared. Firstly, the release and recapture method, whereby the 3D MOT beams are pulsed off for a short duration $\Delta t$ and the cloud is allowed to expand. When the 3D MOT beams are turned back on, the beams recapture the fraction of atoms which remain in the capture region. The fraction of atoms inside this capture region decreases as the release time $\Delta t$ increases. By repeating this measurement for a range of $\Delta t$ and measuring the recaptured fraction as a function of $\Delta t$, a temperature measurement can be made.

The second method used is the time-of-flight (ToF) measurement. Here, the 3D MOT beams and the 3D magnetic field are turned off and after a short time $\Delta t$, an image of the expanding could is taken by switching the beams back on and quickly taking a fluorescence image. From the fluorescence image, the size of the cloud can be deduced. This measurement is repeated for a range of $\Delta t$, and the expansion rate results in a temperature measurement.

### 4.4.1 Release and Recapture

Before explaining our implementation of the release and recapture method and showing the results, it is necessary to give the following short theoretical prelude.

#### Theoretical Release and Recapture

The release-recapture method involves switching off the 3D MOT beams for a short duration and allowing the atomic cloud to expand and leave the capture region [74]. This

capture region will primarily be set by the volume of the overlap between the 3D MOT beams. In order for the atoms to be recaptured, the speed of the atoms must be less than the recapture speed,

$$v_R(\Delta t) = \frac{R_c}{\Delta t}, \tag{4.7}$$

where $R_c$ is the radius of the capture volume and $\Delta t$ is the expansion time. Atoms with speed greater than $v_R$ will travel beyond the recapture radius during $\Delta t$ and will not be recaptured when the MOT beams are switched back on. Using a Maxwell-Boltzmann distribution, the most probable thermal speed of the atoms is given by [75]

$$v_T(T) = \sqrt{\frac{2k_BT}{m}}, \tag{4.8}$$

where $T$ is the temperature of the cloud and $m$ is the mass of a potassium atom. The fraction of atoms with velocities between 0 and $v_R$ will be,

$$\begin{aligned} F &= 4\pi \int_0^{v_R} f(v)dv\,, \\ &= \frac{4}{\sqrt{\pi}} \int_0^{v_R} \frac{dv}{v_T} \left(\frac{v}{v_T}\right)^2 e^{-(v/v_T)^2}\,, \\ &= \frac{4}{\sqrt{\pi}} \int_0^{\xi} \xi'^2 e^{-\xi'^2} d\xi'\,. \end{aligned} \tag{4.9}$$

As seen above, this fraction can be written purely in terms of the ratio between velocity $v$ and the the thermal velocity $v_T$. This has the solution,

$$\begin{aligned} F &= \mathrm{erf}\,(\xi) - 2\frac{\xi}{\sqrt{\pi}} e^{-\xi^2}\,, \\ \xi &\equiv \frac{v_R}{v_T} = \sqrt{\frac{m}{2k_B\Delta t^2}} \frac{R_c}{\sqrt{T}}\,. \end{aligned} \tag{4.10}$$

With the recaptured fraction in this form, an obvious drawback with this technique becomes apparent. Since Equation 4.10 is purely a function of $\xi$, this measurement depends heavily on a good estimation for the capture radius $R_c$. If the estimation for $R_c$ is too large, there will be an over-estimate of the MOT temperature. Here, $R_c$ was taken to be the radius of the MOT beams (1.25 cm), which is an upper-limit. Using an upper-limit value for $R_c$ will result in a measured upper-limit for the temperature.

Whilst this technique is obviously limited, it benefits from being easier to implement than a time-of-flight measurement, since here it is not necessary to turn off the magnetic field. Also, the recaptured fraction can be measured purely from the total MOT fluorescence (which can be performed using a photodiode), with no need for measurements of the cloud size (which requires a camera).

### Implementation of Release and Recapture

Each measurement consisted of a MOT loading interval of 5 s. At the end of this loading interval, a fluorescence image was taken to determine the initial number of atoms in the 3D MOT. After this, the MOT beams were switched off using the 3D MOT switching AOMs, and the 2D MOT push beam was blocked using a mechanical shutter. After a duration of $\Delta t$, the 3D MOT beams were turned back on, a fluorescence image was taken, and the push beam was unblocked. All magnetic fields remained turned on throughout.

This procedure was repeated for a range of values for $\Delta t$. The order in which each $\Delta t$ was executed was randomised to negate any potential long-term effects.[1]

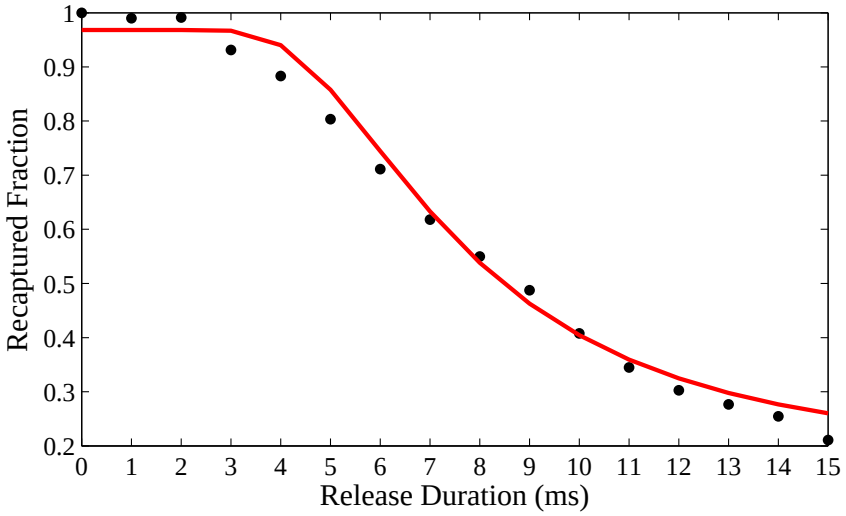


Figure 4.9: A release and recapture temperature measurement. The data (black points) were fitted using Equation 4.10 (red line). From the fit, the temperature was deduced to be 4.3 mK for this data set.

The results are displayed in Figure 4.9 and were fit to Equation 4.10 to give a value for $T$. For a set of four measurements using $R_c = 1.25$ cm, the mean value for the upper-limit temperature was deduced to be $(4.1 \pm 0.4)$ mK, where the error is the standard error.

## 4.4.2 Time of Flight

In contrast to the release and recapture method, the time of flight (ToF) measurement works by mapping out the RMS size of the cloud as a function of time [76].

[1] Long-term effects which may occur are changes in the partial pressure of potassium in the 2D MOT chamber, or changes laser frequencies, intensity drift, et cetera.

The 3D MOT beams and magnetic field are turned off and the cloud is allowed to expand for a time $\Delta t$. After $\Delta t$, a fluorescence image is taken and the RMS sizes are measured. If the initial RMS sizes were $\sigma_{0_{y,z}}$, then after $\Delta t$, the RMS size due to thermal expansion can be described by,

$$\sigma_{y,z}(\Delta t) = \sqrt{\sigma_{0_{y,z}}^2 + \frac{k_B T_{y,z}}{m} (\Delta t)^2}, \tag{4.11}$$

where $T_{y,z}$ is the temperature of the cloud in the $y, z$ directions[2], and $m$ is the mass of one potassium atom. In reality, the cloud potentially has different temperatures for all three dimensions, but from fluorescence images, only two directions can be measured.

Each measurement consisted of a loading interval of 5 s. After loading, the 3D MOT beams and the 2D MOT pushing beam are turned off, and the magnetic field is turned off using a relay switch. After a time $\Delta t$, the beams are turned back on, and the camera is exposed for 1 ms. This measurement was repeated for several $\Delta t$, where the order of $\Delta t$ was shuffled to remove any spurious effects from long-term experimental drifts.

In Figure 4.10, the values of $\sigma_{y,z}$ are plotted as a function of $\Delta t$ where the solid lines are the fits to Equation 4.11. The results show a temperature of $(580 \pm 16)$ and $(643 \pm 37)$ µK in each direction, where the error is the standard error from three sets of ToF measurements.

### 4.4.3 Conclusions on Temperature Measurements

The reliability of the release and recapture method is questionable due to the difficulty of estimating the capture radius $R_c$. The time of flight method however should be reliable. If we accept the value given by the time of flight method, we can infer $R_c$ to be approximately 2.4 mm.

Knowledge of the temperature is important, because later, when we probe the cavity, we are required to turn the MOT beams off. The method we use is to load a MOT for a few seconds, turn the MOT beams off, scan the probe beam using an AOM, and then turn the MOT beams back on. The maximum duration of the scan is limited by thermal expansion of the cloud. At the temperature measured in the time of flight method, the line density along the MOT is expected to reduce to 0.995 times its initial value after a release duration of 100 µs, which is the probe interval duration used. This change in density is negligible over this short scan period, however at longer scan periods it can become significant (after 1 ms, the line density will have decreased to 0.63 times the initial value).

[2]Here, the idea of different temperatures along different directions refers to the spread of kinetic energies along each direction.

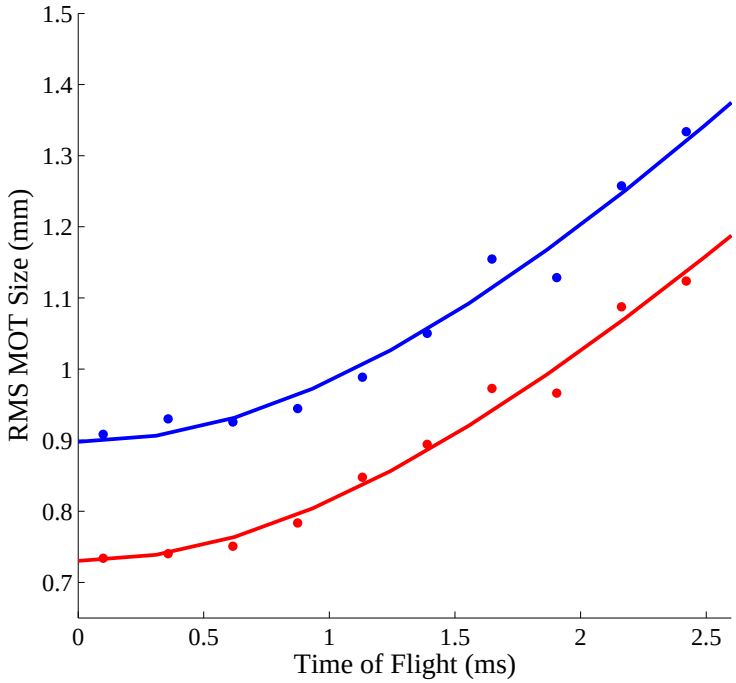


Figure 4.10: A time of flight measurement to deduce MOT temperature. The points show $\sigma_{y,z}$, and the solid lines show fits to Equation 4.11. The red and blue data represent measurements along the $y$ and $z$ directions respectively.

## 4.5 Laser Detuning Optimisation

The frequencies of the cooling and repump beams were optimised to give the highest number of atoms in the 3D MOT. In order to achieve this, the computer control was used to vary the detunings across a range of frequencies (in two dimensions), and after a loading period of 6 s for each detuning set, an image of the MOT was taken along with a background image and the atom number was deduced using the analysis described in Section 4.1. Note that since the laser detunings are changing, the excited state fraction (and thus the fluorescence rate per atom) changes also. In this case, the change was significant, where the excited state fraction from the six-level model has been found to vary from 25 to 40% across the ranges tested.

Due to the large number of points, the data were acquired over a relatively long timescale (approximately 12 minutes), and so the order of each set of detunings was shuffled to remove any long-term fluctuations. The results are shown in Figure 4.11.

The optimum detunings were found to be at $-27.3$ and $-17.5$ MHz for the cooling and

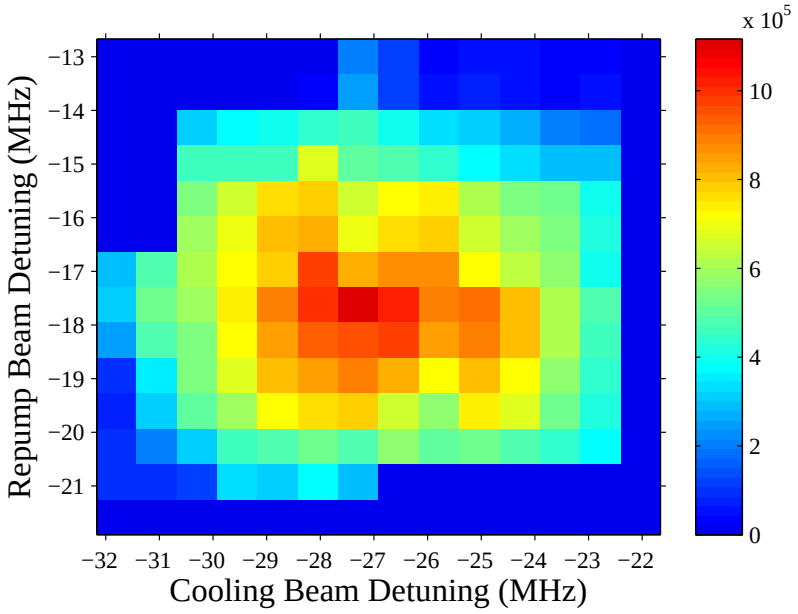


Figure 4.11: Number of atoms in the 3D MOT as a function of the two MOT beam frequencies. Regions showing zero atom number show where the MOT was too dim for the camera with the value of exposure time used here.

repump beams respectively, which roughly agree with other potassium experiments [69, 71]. It is worth noting again that due to the limitations of our setup, the frequencies used for the cooling and repump beams are the same in both the 2D MOT and the 3D MOT. Other experiments operating with the freedom to optimise each MOT separately have indeed found that the optimum frequencies for each MOT differ slightly [69, 71]. A future avenue of investigation would be to operate the pair of 3D MOT switching AOMs at slightly different frequencies to one another to shift the 3D MOT beam frequencies with respect to the 2D MOT beam frequencies, to see whether the system can be optimised further. Using this method, it is only possible to offset the two frequencies in the 3D MOT by the same amount, and independent control remains unavailable.

It is also worth noting that only the number of atoms in the 3D MOT has been optimised here. It is likely that the optimal frequencies for minimal temperature are very different from those found here and is also an avenue of future investigation [77, 78].

## 4.6 Magneto-Optical Trapping Summary

Whilst Chapter 3 detailed the vacuum apparatus and laser system required to realise magneto-optical trapping and overlap cold atoms with the cavity mode, this chapter has focused on the techniques required to optimise and characterise the MOT system.

This chapter began by discussing the techniques required to deduce the number of atoms in the 3D MOT and thus infer the number of intra-cavity atoms, which will be important when estimating the expected normal mode splitting in the upcoming chapters. This chapter also described the effects of beam size, beam detunings, and the gradient and geometry of the magnetic field on the elongated 3D MOT setup, as well as the 2D MOT setup, such that the intra-cavity atom number can be maximised, thus maximising the collective coupling rate $G = \sqrt{N}g$ between the atoms and cavity.

This chapter has also compared two different techniques for measuring the temperature of the 3D MOT. The release and recapture method was shown to be beneficial in that it allows a temperature measurement when fast switching of the magnetic field is unavailable. It can also be implemented with a photodiode and an oscilloscope, with no camera required. The release and recapture method suffers from the obvious drawback that a reliable measurement of the temperature $T$ is difficult if the capture radius $R_c$ is not known, since the recaptured fraction depends only on a parameter $\xi$ which is directly proportional to $R_c/\sqrt{T}$. Thus, an estimation of the capture radius $R_c$ is tantamount to an estimation of the temperature $T$. The time of flight method yields a much more reliable temperature measurement, however this method does require fast magnetic field switching as well as a camera which can be triggered.

Note that both techniques can be used together to infer the capture radius, where the time of flight method can be used to measure $T$, and thus scale $\xi$ with respect to $R_c$ so that the release and recapture method can be used to accurately measure the capture radius. This is potentially interesting, since the relationship between the capture radius and other MOT parameters (for example the beam radius, magnetic field gradient and laser detunings) is not well understood in the Cold Atoms community.

Now that the cold atom aspects of this thesis have been explored in detail, the remainder of this thesis focuses on the optical cavity elements.

# Part II

# Potassium Atoms in an Optical Ring Cavity

CHAPTER 5

# Theory and Setup of the Optical Cavity

This chapter begins by discussing the general theory of optical resonators, which will be very important for the remaining chapters in this thesis. After this theory, the design and realisation of the cavity are discussed. This chapter ends by describing the laser system used to probe and stabilise the cavity.

## 5.1 Optical Cavity Theory

### 5.1.1 Transmission, Reflection and Finesse

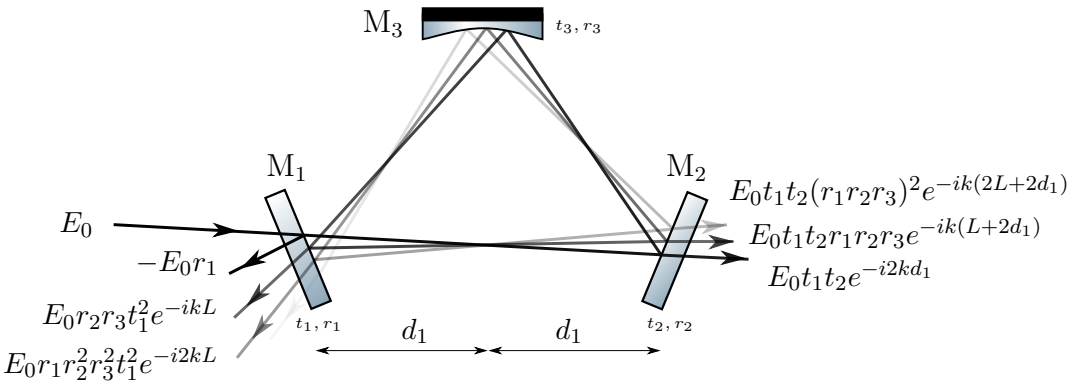


Figure 5.1: Incident, reflected and transmitted fields from a triangular ring cavity. The triangular cavity is formed from three mirrors $M_{1,2,3}$ with field reflection and transmission coefficients $r_{1,2,3}$ and $t_{1,2,3}$ respectively.

A triangular ring cavity with an incident field $E_0$ is shown in Figure 5.1. The mirrors M each have a field reflectivity $r_M$ and transmission $t_M$, where $r_M^2 + t_M^2 = 1$ for lossless mirrors. The total reflected field is an infinite sum of components from each pass. Here, the

first term has a minus sign due to the Stokes relations [79] for reflection and transmission across a boundary,

$$\begin{aligned} E_r &= E_0 \left[ -r_1 + \frac{t_1^2}{r_1} \sum_{n=1}^{\infty} \left( r_1 r_2 r_3 e^{-ikL} \right)^n \right], \\ &= E_0 \left[ \frac{r_2 r_3 e^{-ikL} - r_1}{1 - r_1 r_2 r_3 e^{-ikL}} \right], \end{aligned} \tag{5.1}$$

where $L$ is the round-trip-length of the cavity, and $k$ is the wavenumber of the cavity probe. This gives reflected intensity from mirror $M_1$,

$$I_r = I_0 \frac{\left(r_1 - r_2 r_3\right)^2 + 4 r_1 r_2 r_3 \sin^2(kL/2)}{\left(1 - r_1 r_2 r_3\right)^2 + 4 r_1 r_2 r_3 \sin^2(kL/2)}. \tag{5.2}$$

Similarly, the total transmitted field from $M_2$ is an infinite sum of transmitted components from each pass,

$$\begin{aligned} E_t &= E_0 e^{-i2kd_1} t_1 t_2 \sum_{n=0}^{\infty} \left( r_1 r_2 r_3 e^{-ikL} \right)^n, \\ &= E_0 e^{-i2kd_1} \frac{t_1 t_2}{1 - r_1 r_2 r_3 e^{-ikL}}, \end{aligned} \tag{5.3}$$

where $2kd_1$ is the phase shift incurred by traveling from $M_1$ to $M_2$. From this, the transmitted intensity will be

$$I_t = \frac{I_0}{\left(1 - \sqrt{\rho}\right)^2} \frac{T_1 T_2}{1 + \frac{4\sqrt{\rho}}{\left(1 - \sqrt{\rho}\right)^2} \sin^2(kL/2)}, \tag{5.4}$$

where $\sqrt{\rho} = r_1 r_2 r_3$ is the fractional field amplitude remaining after each round-trip and $T_{1,2} = t_{1,2}^2$.

The circulating intensity is easy to obtain, since $I_c = I_t / T_2$,

$$I_c = \frac{I_0}{\left(1 - \sqrt{\rho}\right)^2} \frac{T_1}{1 + \frac{4\sqrt{\rho}}{\left(1 - \sqrt{\rho}\right)^2} \sin^2(kL/2)}. \tag{5.5}$$

Examples of the transmission and reflection spectra are shown in Figure 5.2. The resonances are approximate to the Lorentzian function for highly reflective mirrors and occur when $kL$ is equal to integer multiples of $2\pi$ and thus, are separated in frequency by the free-spectral range,

$$\mathrm{FSR} = \frac{c}{L}. \tag{5.6}$$

The linewidth in phase units $\delta_{1/2}$ (HWHM) can be found by setting the denominator in Equation 5.4 equal to 2, and taking $\delta_{1/2}$ to be small so that $\sin(\delta_{1/2}/2) \approx \delta_{1/2}/2$,

$$1 + \frac{4\sqrt{\rho}}{\left(1-\sqrt{\rho}\right)^2}\left(\frac{\delta_{1/2}}{2}\right)^2 = 2,$$
$$\delta_{1/2} = \frac{1-\rho^{1/2}}{\rho^{1/4}}.$$

Taking the ratio of the resonance separation ($2\pi$) with the FWHM width ($2\delta_{1/2}$) gives the quantity known as the cavity finesse $\mathcal{F}$,

$$\mathcal{F} = \frac{2\pi}{2\delta_{1/2}} \approx \frac{\pi}{1-\sqrt{\rho}}, \tag{5.7}$$

and frequency units, this becomes

$$\mathcal{F} = \frac{\mathrm{FSR}}{\Delta\nu_{\mathrm{FWHM}}}. \tag{5.8}$$

It can be seen that the cavity finesse $\mathcal{F}$ is a useful quantity for characterising the cavity losses due to the mirror reflectivities, and is easily measured by measuring the cavity linewidth and free spectral range.

### 5.1.2 Hermite-Gaussian Modes

Understanding the shape of the intensity profile of the cavity mode is important for understanding how the optical cavity works. A useful tool for this is Hermite-Gaussian modes, sometimes called transverse electromagnetic (TEM) modes [80, 81]. The field $E(x, y, z) = \psi(x, y, z)e^{-ikz}$ must satisfy the paraxial Helmholtz wave equation,

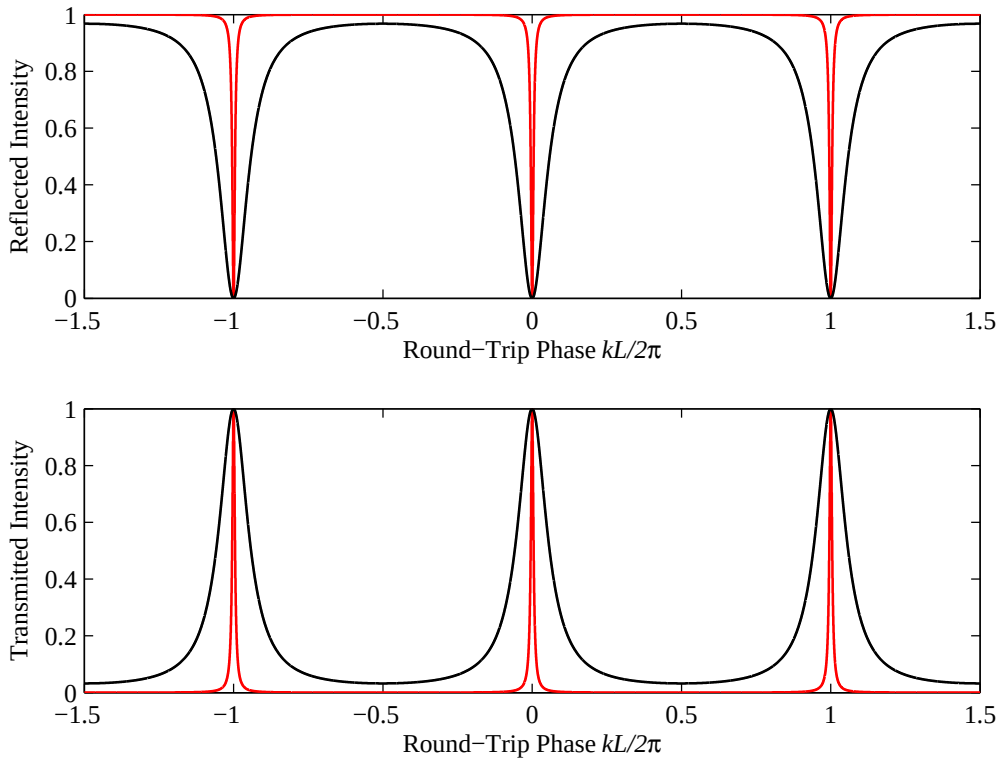


Figure 5.2: Theoretical reflected and transmitted spectra. Black and red curves show finesse of 5 and 50 respectively.

$$\frac{\partial^2\psi}{\partial x^2} + \frac{\partial^2\psi}{\partial y^2} - i2k\frac{\partial\psi}{\partial z^2} = 0, \tag{5.9}$$

which assumes that $\psi(x, y, z)$ varies slowly with $z$. A set of solutions to this equation is

$$E_{m,n}(x,y,z) = AH_m\left(\frac{\sqrt{2}x}{w_x(z)}\right)H_n\left(\frac{\sqrt{2}y}{w_y(z)}\right)\exp\left[-\frac{x^2}{w_x^2(z)} - \frac{y^2}{w_y^2(z)}\right] \times \exp\left[-ikz + i\Phi_{G_{m,n}}(z) - ik\left(\frac{x^2}{2R_x(z)} + \frac{y^2}{2R_y(z)}\right)\right], \tag{5.10}$$

with

$$w_{x,y}(z) = w_{0_{x,y}}\sqrt{1 + \left(z/z_{R_{x,y}}\right)^2}, \qquad R_{x,y}(z) = z\left(1 + \left(z_{R_{x,y}}/z\right)^2\right),$$

$$z_{R_{x,y}} = \pi w_{0_{x,y}}^2/\lambda, \quad \text{and} \quad A = \frac{E_0}{\sqrt{2^{m+n}m!n!}}.$$

where $H$ are Hermite polynomials, $R_{x,y}(z)$ are the wavefront radii in the $x, y$ directions, $z_{R_{x,y}}$ are the Rayleigh lengths[1], $w_{0_{x,y}}$ are the beam radii at the focus ($z = 0$), and $w_{x,y}(z)$ are the beam radii at $z$. $A$ has been specifically chosen to normalise the peak intensity. $\Phi_{G_{m,n}}(z)$ is the Gouy phase shift,

$$\Phi_{G_{m,n}}(z) = \left(m + \frac{1}{2}\right) \tan^{-1}\left(\frac{z}{z_{R_x}}\right) + \left(n + \frac{1}{2}\right) \tan^{-1}\left(\frac{z}{z_{R_y}}\right), \tag{5.11}$$

which, for the $\text{TEM}_{00}$ mode, goes from $-\pi/2$ to $+\pi/2$ as $z$ passes the beam focus at $z = 0$. The Gouy phase shift is very important since it causes an additional mode-dependent phase shift per round-trip inside the cavity, giving rise to different sets of resonance frequencies for each mode. Pictures of TEM mode waists ($z = 0$) are plotted in Figure 5.3.

Since each TEM mode of the cavity has its own set of resonant frequencies, it is useful to use a series of lenses outside the cavity to shape the beam being used to probe the cavity into one specific mode prior to injection. This technique is known as mode-matching [81]. Also, even if the size and shape of the cavity probe beam is optimal, if the beam is not correctly aligned into the cavity, the beam will excite a number of higher-order TEM modes.

In Section 6.2.1, a technique is presented where the Gouy phase is used to accurately measure the length of the cavity, which is an essential measurement for deducing the cavity mode volume.

### 5.1.3 Phase Shifts Due to Mirror Reflections

In addition to the well-known Gouy phase, it is also important to consider the effect of phase shifts from mirror reflections inside the cavity [79, 82]. Figure 5.4 shows an example of a beam being reflected from a mirror.

It can be seen that upon reflecting from a mirror, the field is transformed by

$$E_{m,n}(x, y, z) \rightarrow E_{m,n}(-x, y, z),$$

[1]The Rayleigh length is the distance along $z$ required for the beam to expand from $w_0$ to $\sqrt{2}w_0$.

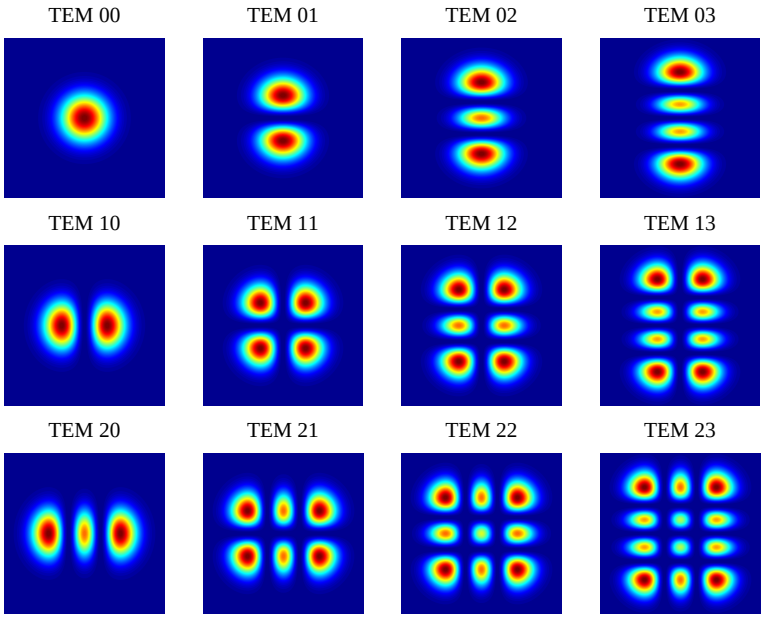


Figure 5.3: Intensity profile of theoretical Hermite-Gaussian $\text{TEM}_{n,m}$ mode waists.

From the Hermite-Gaussian representation in Equation 5.10, and noting that Hermite polynomials are symmetric for even orders and anti-symmetric for odd orders, $E_{m,n}(-x, y, z)$ can be written,

$$E_{m,n}(-x, y, z) = (-1)^m E_{m,n}(x, y, z),$$

This shows that the phase of modes with odd $m$ pick up a factor of $\pi$ upon reflection, whilst those with even $m$ remain unchanged. If there are $M$ mirrors in the cavity, after one round-trip the field will be transformed by

$$E_{m,n}(x, y, z) \rightarrow (-1)^{mM} E_{m,n}(x, y, z) e^{-i\delta_{RT}},$$

where $\delta_{RT}$ is the 'usual' round-trip phase shift due to propagation along the length of the cavity. Note that in Fabry-Pérot cavities, the number of mirrors $M$ is even, and so this factor will have no effect on the resonance condition and is usually completely ignored. In our triangular cavity however, $M$=3, and so this factor cannot be ignored.

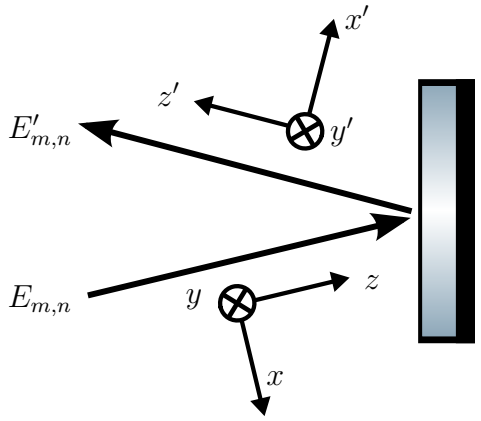


Figure 5.4: Reflection of $E_{m,n}(x, y, z)$ from a mirror becomes $E'_{m,n}(x, y, z) = E_{m,n}(-x, y, z)$.

In order to calculate the transverse mode spacings in the next section, it is useful to summarise that the change in phase per round-trip due to mirror reflections is given by

$$\phi_{mM} = \begin{cases} 0 & \text{if } (m \times M) \text{ is even,} \\ \pi & \text{if } (m \times M) \text{ is odd.} \end{cases} \tag{5.12}$$

### 5.1.4 ABCD Transformations

It can be seen in Equation 5.10 that the field is partially described by the focusing properties of the beam. ABCD transformations [83, 84] are a useful tool to interpret these properties, and will be treated in this section.

A beam in the $\mathrm{TEM}_{0,0}$ mode can be described by the complex beam parameter, which has the simplest form,

$$\mathcal{Q}(z) = z + iz_R\,. \tag{5.13}$$

This quantity is useful, since the distance to the beam waist is given by $z = \mathrm{Re}\{\mathcal{Q}(z)\}$, and the waist radius is given by $w_0 = \sqrt{\mathrm{Im}\{\mathcal{Q}(z)\}\,\lambda/\pi}$.

The complex beam parameter can be transformed with ABCD matrices, which are unimodular matrices used to represent optical transformations. The beam parameter $\mathcal{Q}$ after a transformation will become $\mathcal{Q}'$ like so,

$$\mathcal{Q}' = \frac{A\mathcal{Q} + B}{C\mathcal{Q} + D}\,. \tag{5.14}$$

Two ABCD matrices which were used extensively in this experiment are those which represent a lens of focal length $f$ (or in our case, a curved mirror of focal length $f = R/2$, where $R$ is the radius of curvature) and free-space propagation of a distance $d$ along $z$,

$$\begin{pmatrix} A & B \\ C & D \end{pmatrix}_{lens} = \begin{pmatrix} 1 & 0 \\ -1/f & 1 \end{pmatrix} \quad \text{and} \quad \begin{pmatrix} A & B \\ C & D \end{pmatrix}_{d} = \begin{pmatrix} 1 & d \\ 0 & 1 \end{pmatrix}. \tag{5.15}$$

Using these ABCD matrices for our cavity, the beam waist $w_0$ can be extracted from $\mathcal{Q}$, and is discussed further in Section 5.1.5. These ABCD matrices were also essential for mode-matching the cavity, discussed in Section 5.4.1.

### 5.1.5 Cavity Waist Calculation

Knowledge of the cavity mode waists is crucial for calculating the cavity mode volume which is instrumental when discerning the coupling strength between the atoms and the cavity. Inside a stable cavity, the field distribution is replicated after after each round-trip. This means that for an ABCD matrix representing a stable cavity, the pre-transformation complex beam parameter $\mathcal{Q}$ will be equal to the post-transformation complex beam parameter $\mathcal{Q}'$ in Equation 5.14. This gives,

$$\mathcal{Q} = \frac{A\mathcal{Q} + B}{C\mathcal{Q} + D}. \tag{5.16}$$

It is worth noting that this condition is only solvable for $\mathcal{Q}$ if the cavity is stable. The ABCD matrix for a stable cavity should satisfy [85]

$$|A + D| \leq 2. \tag{5.17}$$

It is useful to represent the cavity as a sequence of lenses, as shown in Figure 5.5. In our cavity, the central mirror is curved and the side mirrors are both flat, which leads to the ABCD matrix,

$$\begin{pmatrix} A & B \\ C & D \end{pmatrix} = \begin{pmatrix} 1 & d_1 \\ 0 & 1 \end{pmatrix} \begin{pmatrix} 1 & d_2 \\ 0 & 1 \end{pmatrix} \begin{pmatrix} 1 & 0 \\ -1/f & 1 \end{pmatrix} \begin{pmatrix} 1 & d_2 \\ 0 & 1 \end{pmatrix} \begin{pmatrix} 1 & d_1 \\ 0 & 1 \end{pmatrix}. \tag{5.18}$$

Since the beam is not at normal incidence to the curved mirror, astigmatism needs to be taken into account. For a curved mirror of radius $R$, the focal length $f$ will be $R/(2\cos\theta)$

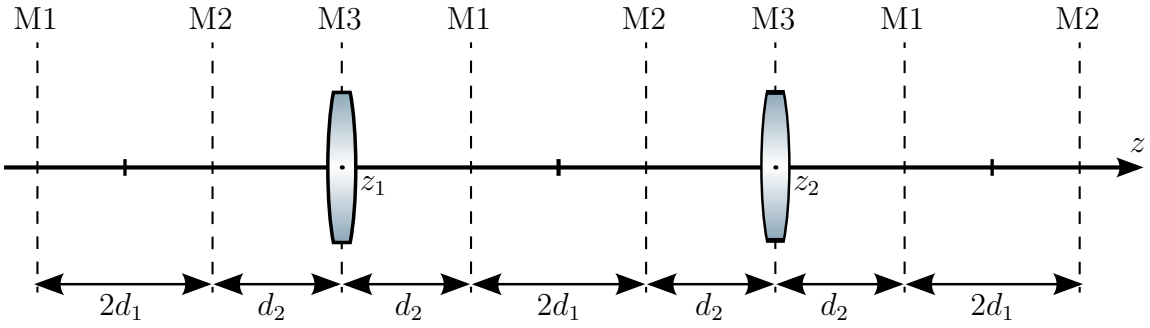


Figure 5.5: Here, the cavity is being represented as an 'unwrapped' sequence of lenses. M1 and M2 are the positions of the flat mirrors and do not transform the complex beam parameter $\mathcal{Q}$.

in the sagittal plane and $(R\cos\theta)/2$ in the tangential plane for angle of incidence $\theta$ to the normal axis.

Upon solving Equation 5.16 for $\mathcal{Q}$, the beam waist can be calculated with $w_{0_{x,y}} = \sqrt{\mathrm{Im}\left\{\mathcal{Q}_{x,y}(z)\right\}\lambda/\pi}$. Table 5.1 shows the results of this calculation.

| | |
|---|---|
| Distance 1 $d_1$ | 2 cm |
| Distance 2 $d2$ | $2\sqrt{2}$cm |
| Central Mirror Radius $R$ | 10 cm |
| Angle of Incidence $\theta$ | 45° |
| Probe Wavelength | 770 nm |
| Sagittal Waist | 128.2 µm |
| Tangential Waist | 89.8 µm |

Table 5.1: Nominal focal properties of the cavity.

### 5.1.6 Calculation of Transverse Mode Spacing

To calculate the frequency spacing of the transverse modes of the cavity, consider the phase of the field at the beginning and end of one round-trip, where the round-trip starts and ends at the central mirror. Using notation from the unwrapped picture shown in Figure 5.5 the round-trip phase shift will be,

$$\delta_{RT} = \phi(z_2) - \phi(z_1),$$

$$\delta_{RT} = k\left(z_2 - z_1\right) - \left(m + \frac{1}{2}\right) 2\tan^{-1}\left(\frac{L}{2z_{R_x}}\right) - \left(n + \frac{1}{2}\right) 2\tan^{-1}\left(\frac{L}{2z_{R_y}}\right) - \phi_{mM}, \quad (5.19)$$

where $z_{1,2}$ correspond to $\pm L/2$ and $\phi_{mM}$ is the phase shift incurred by mirror reflections given by Equation 5.12.

The resonance condition is that $\delta_{RT} = 2\pi q$ where $q$ is an integer, which leads to resonant frequencies,

$$2\pi \cdot \nu_{mnq} = \frac{c}{L}\left\{\left(m+\frac{1}{2}\right)2\tan^{-1}\left(\frac{L}{2z_{R_x}}\right)+\left(n+\frac{1}{2}\right)2\tan^{-1}\left(\frac{L}{2z_{R_y}}\right)+\phi_{mM}+2\pi q\right\}, \tag{5.20}$$

which simplifies somewhat to

$$2\pi \cdot \nu_{mnq} = \frac{c}{L}\left\{\left(m+\frac{1}{2}\right)\cos^{-1}\left(1-\frac{L}{\mathcal{R}_x}\right)+\left(n+\frac{1}{2}\right)\cos^{-1}\left(1-\frac{L}{\mathcal{R}_y}\right)+\phi_{mM}+2\pi q\right\}, \tag{5.21}$$

where $\mathcal{R}_{x,y}$ are the effective radii of curvature of the central mirror in the $x$ and $y$ directions. Since the light is incident on the curved central mirror at 45°, the cavity is astigmatic, resulting in $\mathcal{R}_x = \mathcal{R}/\cos(\pi/4)$ and $\mathcal{R}_y = \mathcal{R}\cos(\pi/4)$ for a mirror of radius $\mathcal{R}$.

## 5.2 Cavity Realisation

The purpose of this section is to describe the physical design and manufacture of the cavity, with the hopes that anyone designing their own cavity might find this information useful. Firstly, I will describe the problems we experienced with the first generation design and the necessity for a new design. I will then describe the gluing process for the mirrors, and finally I will describe the mechanical design of the flexure mount which is used to scan the cavity length.

### 5.2.1 Shortcomings of the First Generation of the Experiment

Unfortunately, the first generation of this experiment (shown in Figure 5.6) only showed atom-cavity interaction for the first few weeks of operation whereafter the cavity finesse dropped significantly and became unusable. It is believed that the cavity finesse dropped due to the mirrors being coated by either potassium or vacuum contaminants from the dispensers. To remedy this, the system was baked extensively and light-induced atomic

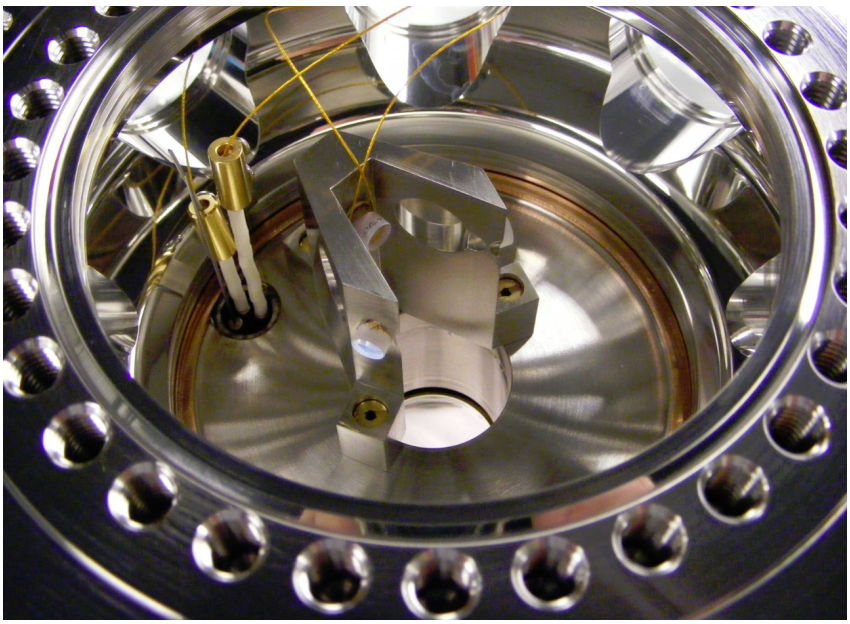

Figure 5.6: Photograph of first-generation cavity experiment.

desorption [86] (using 200 mW of 405 nm light) was attempted, but no improvements in finesse were seen.

Prior to dispenser usage, the cavity finesse was around 2000. After one month of dispenser usage, this had dropped to 551. After three months, the finesse continued to drop further to 103, indicating a round-trip loss of 19.2%. Upon finally removing the cavity from the vacuum system and wiping the central mirror with acetone and isopropanol, the round-trip losses were halved from 19.2% to 8.2%. The faces of the two flat mirrors were inaccessible for cleaning due to the design of the cavity frame and it was decided that a second generation of the experiment should be designed, with the principal intention of keeping the cavity mirrors clean for sustained experimental operation.

To keep the mirrors clean, the new experimental design criteria were to:

1. Keep the cavity chamber as clean as possible by loading the 3D MOT from a 'dirty' 2D MOT chamber.
2. Provide cleaning access to all mirror faces, should the cavity mirrors get dirty.

The round-trip losses for the old and new designs are shown in Figure 5.7. So far, the new design has been a success and the cavity finesse has been maintained for a year and a half of dispenser operation. It can be concluded that loading from an atomic beam removes the problem encountered by loading directly from the background pressure.

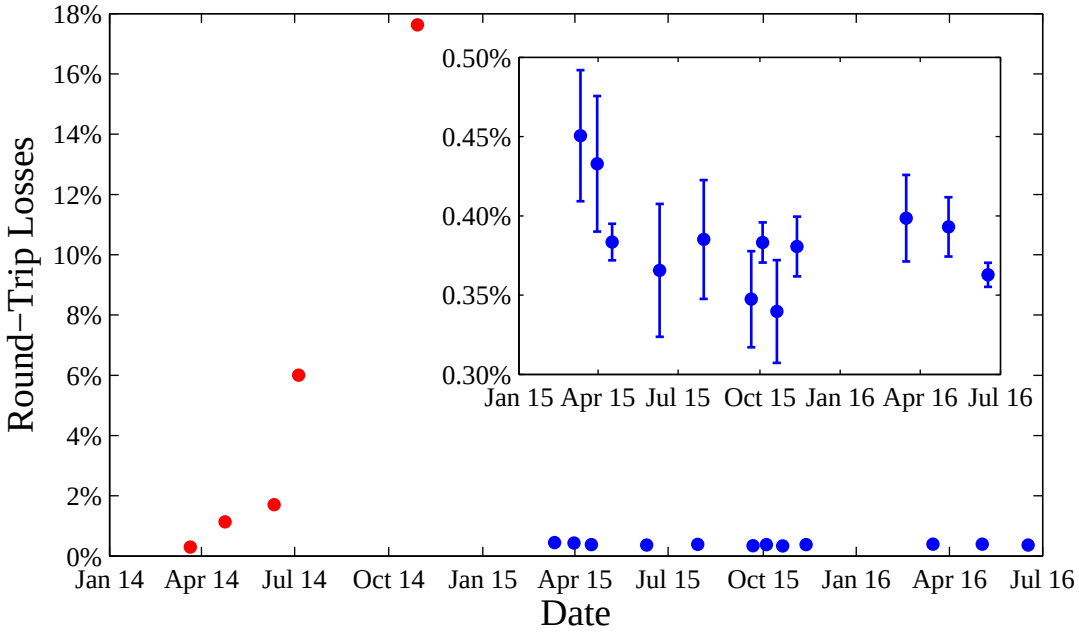


Figure 5.7: Round-tip losses (power) as a function of time. The red data show the previous generation of the experiment, where the MOT was being loaded from the background pressure. The blue data show the current generation of the experiment, where the MOT is being loaded from the newly installed 2D MOT. The inset shows a close-up of the current generation.

### 5.2.2 Designing the New Cavity

The cavity forms a right-angled triangle, consisting of two flat input and output mirrors and a curved central mirror. These mirrors are glued onto posts of a monolithic stainless steel cavity frame. The monolithic design was chosen to reduce the degrees of freedom for alignment and reduce the complexity of the vacuum assembly. The posts of the frame have been designed to hold the mirrors at the correct height without obscuring the MOT beams.

To allow the atomic beam from the 2D MOT to reach the 3D MOT, the cavity is tilted with respect to the 3D MOT beams using a 45° wedge piece. This wedge has a hole in to allow the atomic beam to pass underneath the cavity frame and reach the 3D MOT. Although this tilted design may seem flamboyant, it was chosen since it is the easiest way to keep all mirrors out of the path of the atomic beam, which we believe to be very important for keeping the mirrors clean.

Tilting the cavity at 45° comes with the added complication that the reflected beam from

the cavity is no longer aligned with a vacuum view port. To correct this, two additional 'steering' mirrors must be attached to the cavity frame, to steer the reflected beams out of the vacuum chamber parallel to the input beams.

To control the length of the cavity, a piezo actuator is used. The panel to which the central mirror is glued is flexure hinged, with a piezo actuator slotted behind. This hinge is discussed further in Section 5.2.5.

Since the cavity frame is monolithic, alignment of the cavity is done purely by careful positioning and gluing of the curved central mirror and is discussed further in Section 5.2.4. The two flat mirrors are glued onto V-grooves, which help restrict the degrees of freedom of the mirror placement, as well as leaving the faces of the mirrors accessible for cleaning.

### 5.2.3 Gluing the Mirrors

The gluing of the mirrors was not straightforward. The problem lies with the fact that the glue has to be heated in order to cure[2]; but as the glue is heated the glue can become very inviscid, causing movement to occur. Furthermore, even after the glue has been cured, heating the glue past its cure temperature can cause the glue to become inviscid again. To work around these problems, the mirrors were glued in a sequence with a combination of air-curing and heat-curing. Our gluing procedure is outlined here.

Firstly, the two flat input and output mirrors were glued with the cavity frame sitting horizontally. These mirrors sit in V-grooves and were straightforward to position. The glue was allowed to air-cure for one day, where the frame was then carefully transferred to an oven to heat-cure. The oven was heated slowly to 190°C, and the glue was cured for two hours. Since the cavity frame could not be easily cleaned after the mirrors had been attached, the cavity was kept as clean and dust-free as possible by covering it during the lengthy air-curing process.

After the frame was cooled to room temperature, the first steering mirror was glued. The frame was cooled to room temperature, mounted vertically using a mounting bracket and rotated to an angle of 22.5° so that the steering mirror mounting arm was horizontally flat, as shown in Figure 5.8. The first steering mirror was glued, and transferred to the curing oven immediately. The frame and bracket were then slowly heated and cured at 180°C for two hours. This temperature was chosen since it is slightly lower than the cure

[2]The glue used was Epo-Tek H74, which recommends curing at 150°C for one hour.

temperature for the flat mirrors. Using this method, the risk of any previously cured glue becoming inviscid again was minimised.

The second steering mirror was glued in a similar manner to the first, using the mounting bracket. For this mirror, the glue was cured at 170°C for two hours.

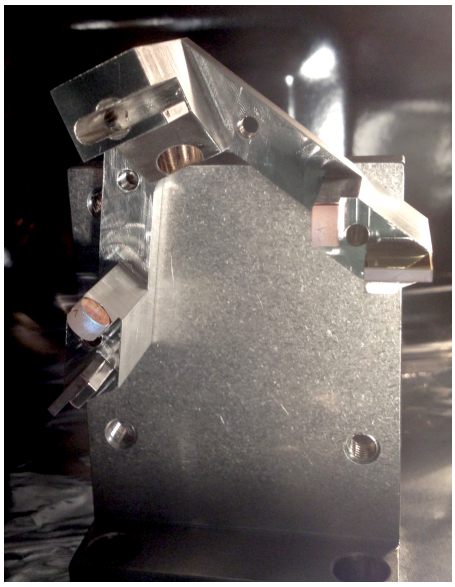

Figure 5.8: Photograph showing mounting bracket being used to glue the second steering mirror.

### 5.2.4 Gluing the Central Mirror

Since the cavity frame is monolithic, the alignment of the cavity mirrors was done by careful positioning of the central curved mirror. For this, the piezo was slotted into place and the cavity was mounted on the optical table such that the panel for the central mirror was horizontally flat so that the central mirror could be placed on it, as shown in Figure 5.9. Light was shone into the cavity, and with the aid of an infrared camera, the mirror was moved by hand until a stable cavity was formed and a transmission spectrum could be seen. At this stage, the piezo actuator and flexure mount could be tested for any faults.

With the mirror in a good position, glue was added and allowed to air-cure for two days. During these two days, the cavity remained part of the optical setup, so that any drift of the mirrors would be detected. No drift was seen, and after the air-cure the cavity frame and mounting bracket were transferred to the oven (with the piezo still in place)

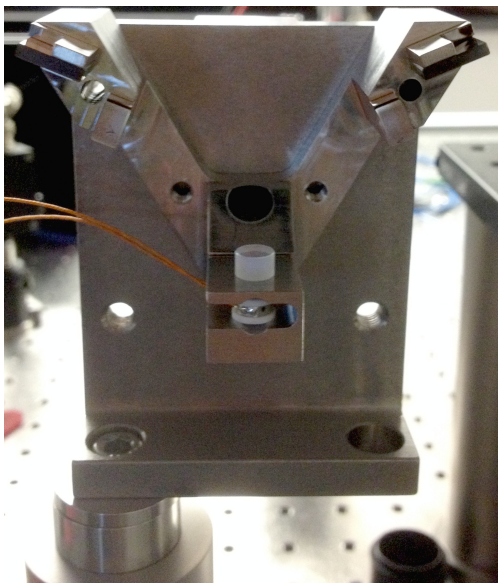

(a) Mounting the cavity ready to be probed

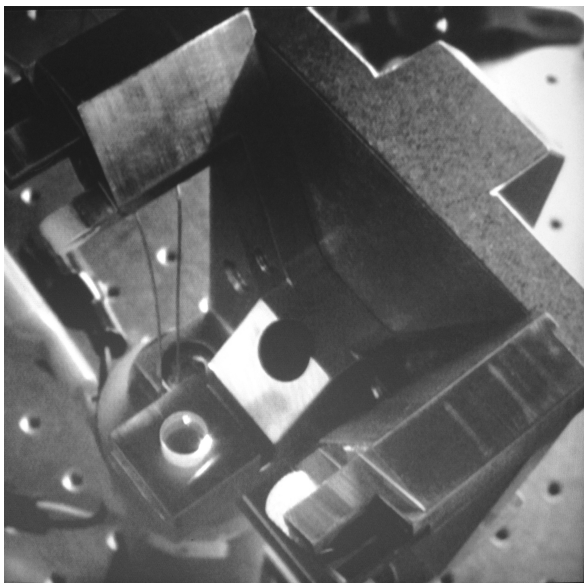

(b) Aligning cavity using an IR camera

Figure 5.9: This setup was used to correctly position the central (curved) mirror prior to gluing. Light is incident from the right hand side and a photodiode monitors the transmitted beam on the left hand side (off camera).

to heat-cure at 160°C for three hours. After curing, the cavity alignment was re-checked by transferring it back to the optical table.

At this stage, all the mirrors had been glued, and the cavity was ready to be transferred to the vacuum system where it would be baked at 150°C.

The gluing procedures are summarised in the Table 5.2.

| Step | Mirror(s) | Cure Temperature |
|---|---|---|
| 1 | Flat Mirrors | 190 °C |
| 2 | Steering Mirror 1 | 180 °C |
| 3 | Steering Mirror 1 | 170 °C |
| 4 | Curved Mirror | 160 °C |

Table 5.2: Summary of gluing and curing procedure.

### 5.2.5 Design of the Flexure Mount

In the previous cavity design, the central mirror was directly glued onto the piezo, which proved to be undesirable, since the central mirror could not be removed without de-

stroying the piezo. The new design removes this problem by using flexure mount for the central mirror, and is shown in Figure 5.10. The piezo is sandwiched between two macor ceramic spacers to electrically isolate the piezo from the cavity frame and is then slotted into grooves located behind the mirror mount. The gap in the frame is slightly smaller than the piezo-macor sandwich, and so tension holds the sandwich in place.

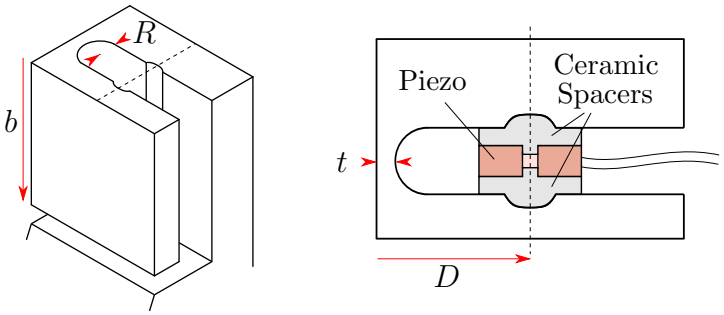


Figure 5.10: Orthographic projection of the flexure mount (left) and top-down view of flexure mount (right). The piezo and ceramic spacers are shown. The ceramic spacer discs are rounded on one side to slot into the grooves in the flexure mount, and have a knob on the other side which holds the ring-shaped piezo in place.

Initially, we were unsure whether this design would work, since we were unsure how much force was required to displace the flexure and whether the piezo was strong enough to meet this requirement. Using the simplified equations[3] from Reference [87] the ratio of angular displacement $\alpha_z$ to applied torque $M_z$ is given by,

$$\frac{\alpha_z}{M_z} = \frac{9\pi R^{1/2}}{2Ebt^{5/2}}, \tag{5.22}$$

where $R$ is the radius of curvature of the flexure groove, $E$ is the Young's modulus of the material, and $b$ and $t$ are length and minimum thickness of the hinge. If the piezo applies a force at a distance $D$ away from the hinge, this leads to a load stiffness of

$$k_L = \frac{(M_z/D)}{\alpha_z D} = \frac{2Ebt^{5/2}}{9\pi D^2 R^{1/2}}. \tag{5.23}$$

The maximum displacement $\Delta L$ for a preloaded piezo is given by

$$\Delta L = \frac{k_A \Delta L_0}{k_A + k_L} - \frac{k_L d}{k_A + k_L}, \tag{5.24}$$

where $k_A$ and $\Delta L_0$ are the actuator stiffness and free stroke for the piezo. As described earlier, the gap behind the flexure mount is slightly too small for the piezo-ceramic

[3]Note that this equation is for a hinge geometry slightly different to ours, in that this is for a hinge rounded on both sides, rather than rounded on one side and flat on the other.

sandwich. This tightness is encapsulated by the parameter $d$, which is the distance the flexure must be displaced from its natural position in order to accommodate the piezo-ceramic sandwich.

The hinge tightness $d$ was not machined into the hinge, but was set after machining by squeezing the mount and intentionally deforming the hinge until the hinge was tight enough to hold the piezo in place. As can be seen from Equation 5.24, tightening this hinge (increasing $d$) leads to a decrease in the maximum piezo extension. This tightening was performed prior to the gluing of the central mirror so that the flexure could be tested (as shown earlier in Figure 5.9).

The piezo driver used in this experiment can only supply 75% of the maximum specified voltage for the piezo, so the full piezo extension $\Delta L$ cannot be reached. For this reason, it is necessary to consider a limited maximum piezo extension $\Delta L'$, where $\Delta L' = 0.75 \times \Delta L$. From the geometry of our cavity, the maximum change in the cavity length $\Delta L'_c$ relates to our maximum piezo displacement $\Delta L'$ by

$$\Delta L'_c = \sqrt{2}\Delta L' \,. \tag{5.25}$$

Across the range of the piezo driver voltage, roughly 3.2 free spectral ranges are seen, which corresponds to a cavity length change of roughly 2.46 µm. From Equations 5.24 and 5.25, the hinge tightness $d$ can be estimated to be around 110 µm.

| Parameter | Symbol | Value |
|---|---|---|
| Young's Modulus | $E$ | $2 \times 10^5$ N mm$^{-2}$ |
| Flexure Groove Radius | $R$ | 2 mm |
| Flexure Length | $b$ | 15 mm |
| Flexure Width | $t$ | 1 mm |
| Lever Length | $D$ | 7.5 mm |
| Load Stiffness | $k_L$ | 2.7 N µm$^{-1}$ |
| Actuator Stiffness | $k_A$ | 321 N µm$^{-1}$ |
| Actuator Free Stroke | $\Delta L_0$ | 3.3 µm |

Table 5.3: Values of various parameters regarding the flexure mount.

## 5.3 Cavity Laser System

Whilst Section 3.2 detailed the laser system used for getting cold atoms into the cavity mode, this section describes the laser system concerned with probing the cavity and

inducing EIT in the atoms once they are inside cavity mode. To modify the group index using EIT, a probe beam and EIT coupling beam are needed. For these beams, a commercial Toptica DL Pro set to the $D_1$ line of $^{39}$K (770 nm) is used. A method of stabilising the cavity length is also required, for which a second Toptica DL Pro near to 852 nm is used. The wavelength of 852 nm was chosen since it is far from resonance with potassium. Also, 852 nm is commonly used in atomic physics since it is the wavelength of the $D_2$ line of cesium, meaning that reference cells and optics such as waveplates and colour filters are easily available.

The schematic for the laser system is shown in Figure 5.11. The frequencies generated by this system are related to the $^{39}$K $D_1$ line in Figure 5.12.

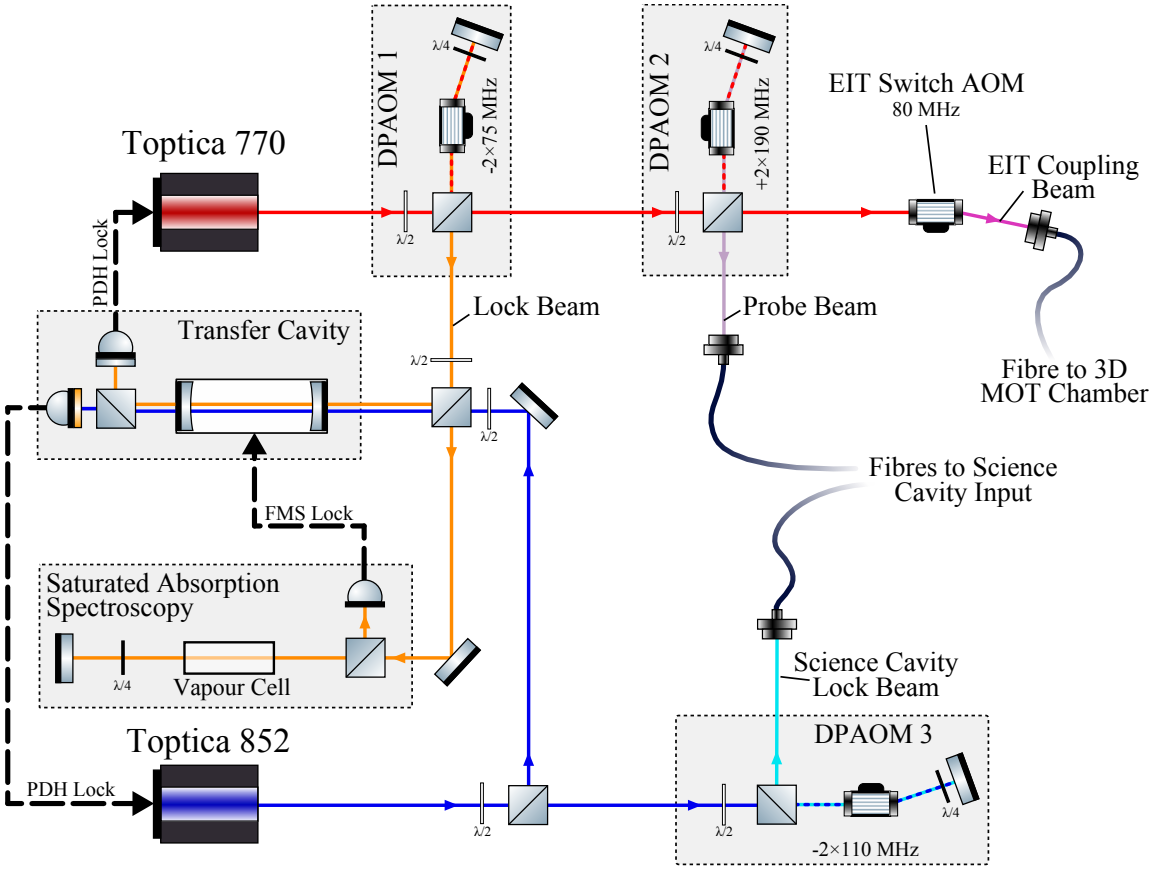


Figure 5.11: Simplified representation of the laser setup used for probing and stabilising the science cavity. Beams with different colours are at different frequencies and thick dashed black lines represent stabilisation electronics. Double-passed acousto-optical modulators (DPAOMs) 1, 2 and 3 are used to tune the frequencies of the EIT coupling beam, probe beam and science cavity locking beam respectively.

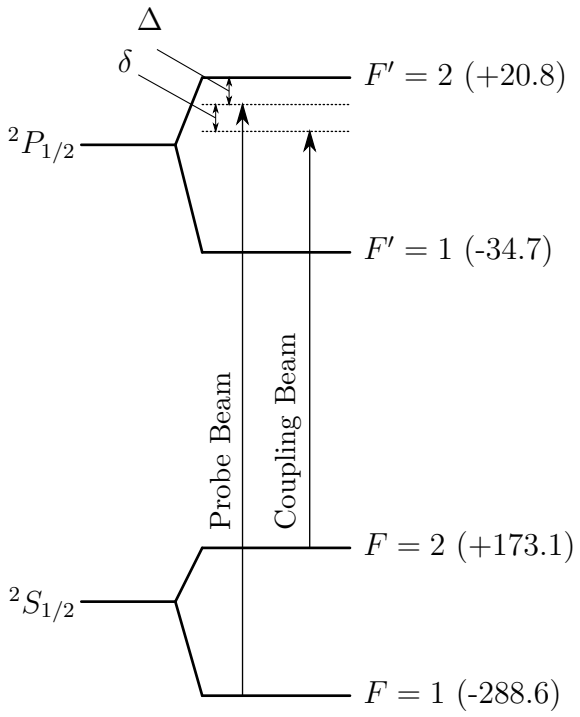


Figure 5.12: Transition diagram for the $D_1$ line of $^{39}$K. The detunings $\Delta$ and $\delta$ can be set using DPAOM1 and 2 from Figure 5.11.

### 5.3.1 Toptica 770 nm Laser

As can be seen from Figure 5.11, the 770 nm Toptica laser is used to produce three beams at different frequencies. These beams are the science cavity[4] probe beam, the EIT coupling beam, and a locking beam. Firstly, the locking beam is used to lock the 770 nm laser to the transfer cavity using a Pound-Drever Hall lock, and in turn, the transfer cavity is scanned and locked to the potassium spectroscopy via the locking beam using frequency modulation spectroscopy. These locks are detailed in the next sections.

Now that the 770 nm laser frequency is stabilised, the modulation frequency of DPAOM2 can be scanned to change the frequency of the probe beam, and the frequency of DPAOM1 can be used to shift the frequency of the EIT coupling beam and probe beam together.

The probe beam and EIT beams can be switched on and off quickly by changing the RF power to DPAOM2 and the EIT switch AOM respectively. To maintain as much optical power as possible in the EIT coupling beam, the EIT switch AOM is a single-passed AOM, operating at its central frequency.

[4]Since there is a more than one cavity in this setup, confusion can be avoided by referring to the cavity being used to interact with the atoms as the 'science' cavity.

### 5.3.2 Transfer Cavity and Pound-Drever-Hall Locking

At the heart of this laser system lies the transfer cavity. This cavity is a standard two mirror Fabry-Pérot cavity which allows us to create a correlation between the stabilities of the 770 nm and 852 nm laser systems in a way which wouldn't be available using a beat-offset lock, due to the large frequency difference. By locking both lasers to this transfer cavity, the coherence time between the two lasers can become very long, meaning that there is little relative jitter between the probe beam and the science cavity lock beam and thus the science cavity length.

To stabilise the lasers to the transfer cavity, the Pound-Drever-Hall (PDH) method [88, 89] is used. The PDH lock used in our system differs to that of a usual PDH lock in that we operate in transmission rather than reflection, which is possible due to the fairly low cavity finesse of $188 \pm 15$. An example of the cavity transmission with the PDH error signal for the 770 nm light is shown in Figure 5.13.

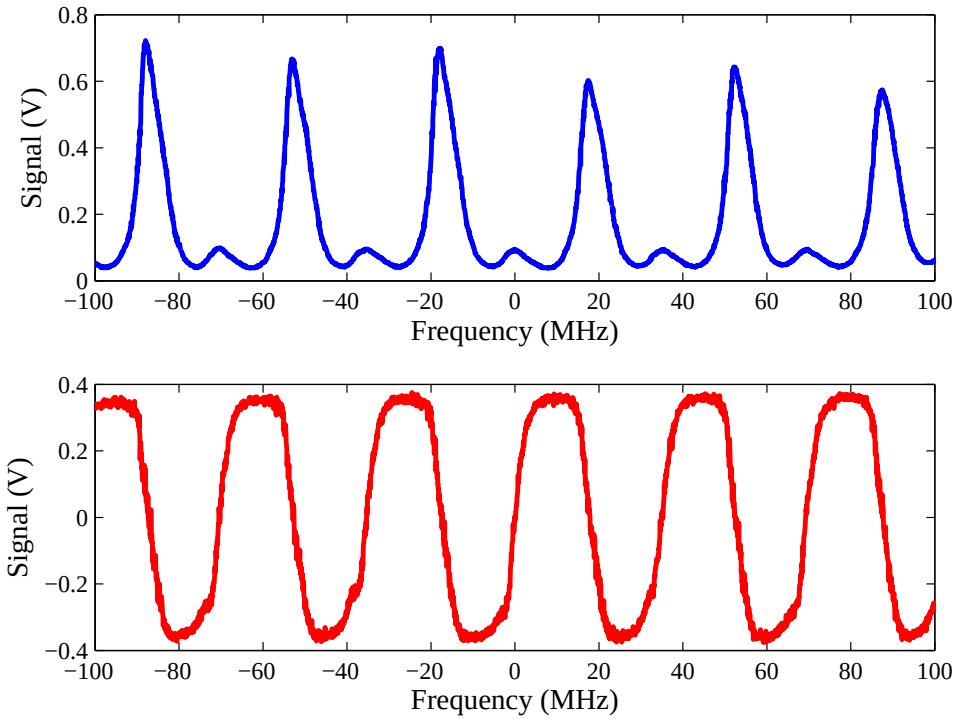


Figure 5.13: Example transmission signal (top) and Pound-Drever-Hall error signal (bottom) showing the high-density of lock points for the 770 nm lock beam.

An important feature of the transfer cavity is that the length has been set such that the transverse modes are degenerate [90], allowing a high density of lock-points. In addition

to this, the modulation frequency has been set to equal to half the transverse mode spacing, doubling the number of points available for locking. This is beneficial to our system because it provides us with high density of lock-points. In order to arbitrarily set the probe beam frequency and the resonance frequency of the science cavity, the spacing between these lock-points needs to be smaller than the bandwidth of the AOMs used for tuning the probe and science cavity length (DPAOMS 2 and 3).

The transfer cavity has linewidths $(7.5 \pm 0.3)$MHz and $(8.8 \pm 0.4)$MHz for 770 nm and 852 nm respectively. The mirror radius of curvature is 15 cm, and the length is roughly 19.1 cm. The degenerate transverse mode spacing is 34 MHz and the modulation for both lasers is performed by modulating the laser current at 17 MHz. The physical design of the transfer cavity is described in detail in Lawrence Mudarikwa's thesis [59]. There are future plans to improve the finesse of this cavity, since it is believed this linewidth may be too broad to really increase the coherence time between the two lasers. If the finesse is improved, the PDH lock will be set up to work with the reflected beams rather than the transmitted beam.

Since the frequency modulation is achieved by modulating the laser current (for both lasers), the modulation is present on all beams throughout this laser system. For the 770 nm light, the modulation is potentially problematic, because the modulation exists on the science cavity probe beam and EIT coupling beam. However, we believe this problem to be insignificant, since modulation frequency (17 MHz) is much narrower than the science cavity linewidth ($\sim 2$ MHz), and so the sidebands are far from resonant with the science cavity. For the EIT control beam, we believe this problem to be insignificant since the atoms in the MOT are cold and Doppler broadening is small (less than 1 MHz), thus the effective atomic linewidth should be close to the natural linewidth ($\sim 6$ MHz FWHM) which is far from resonant with the sidebands.

These locks provide a long-term lock stability of 0.84 MHz between the 770 nm laser and the transfer cavity and 0.93 MHz between the 852 nm laser and the transfer cavity.

### 5.3.3 Frequency Modulation Spectroscopy

Since the 770 nm laser is locked to the transfer cavity, the frequency of the laser can be scanned by scanning the transfer cavity length using the transfer cavity piezo. The transfer cavity can therefore be locked using frequency modulation spectroscopy (FMS) on the Doppler-free saturated absorption spectrum of the potassium $D_1$ line.

Since the laser frequency is already being current modulated for the PDH lock, that same modulation is used here to derive an error signal from the spectroscopy signal. Since the modulation comes from a Toptica PDH module, the only way to control the phase of the reference frequency for the FMS lock is to use a delay line between the PDH module and the FMS mixer. An example spectroscopy signal and FMS error signal is shown in Figure 5.14. This lock provides the transfer cavity with a long-term frequency stability of approximately 0.7 MHz.

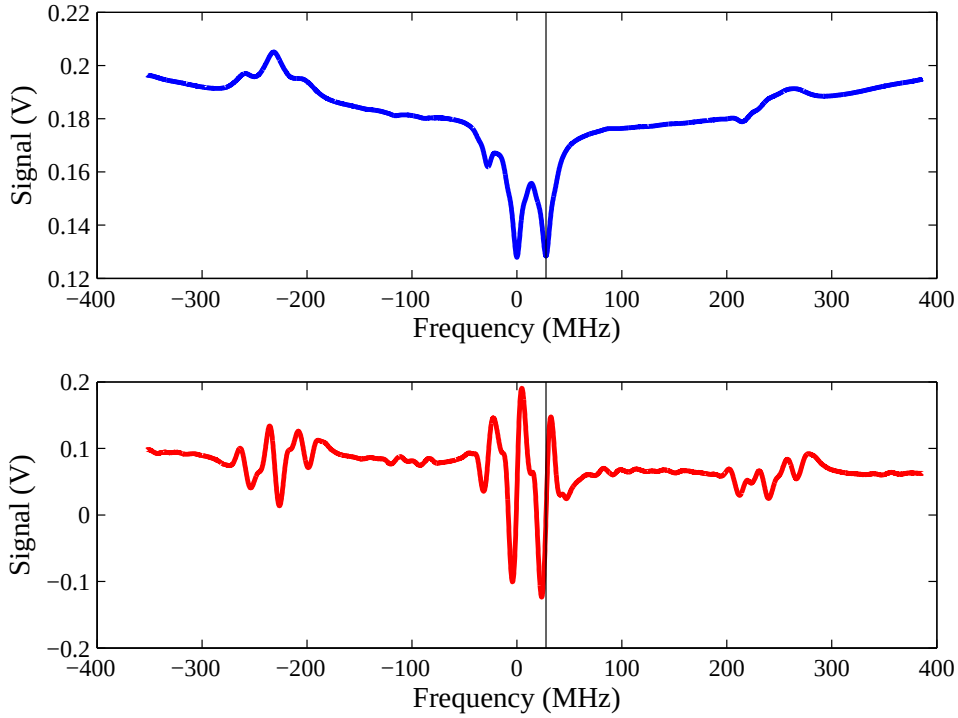


Figure 5.14: Potassium $D_1$ saturated absorption spectroscopy signal generated from scanning transfer cavity (top), and corresponding error signal generated from frequency modulation spectroscopy (bottom).

### 5.3.4 Locking the Science Cavity

The Toptica 852 nm laser is responsible for stabilising the length of the science cavity. Firstly, this laser is locked to the transfer cavity as previously described, creating a frequency-stablised beam for the science cavity to lock to. This lock beam is then sent to the science cavity, and the PDH technique is used in reflection to stabilise the science cavity length, using the existing 17MHz frequency modulation from the transfer cavity

PDH lock. As with the FMS lock, the phase of the reference frequency for the science cavity lock is controlled by adding a delay line, and the long-term lock stability between the 852 nm laser and science cavity is approximately 0.8 MHz. The modulation frequency of DPAOM3 can then be used to step the length of the science cavity.

## 5.4 Cavity Input, Output and Mode-Matching

The optical setup for the input and output for the science cavity is shown in Figure 5.15. The 770 nm probe beam and the 852 nm lock beam are brought in by separate polarisation-maintaining fibres and are combined on a polarising beam cube. The polarisation of each beam is corrected with a pair of narrow-band half-wave plates for each wavelength. Polarisation is important since, as described earlier, the cavity is astigmatic which causes a different cavity spectrum for each polarisation. The mirror reflectivity is also polarisation and wavelength dependent leading to different finesses for each polarisation and wavelength. The reflected beam is sent to a photodiode after passing through a long-pass chromatic filter which filters off the 770 nm light, leaving only the 852 nm light required for locking.

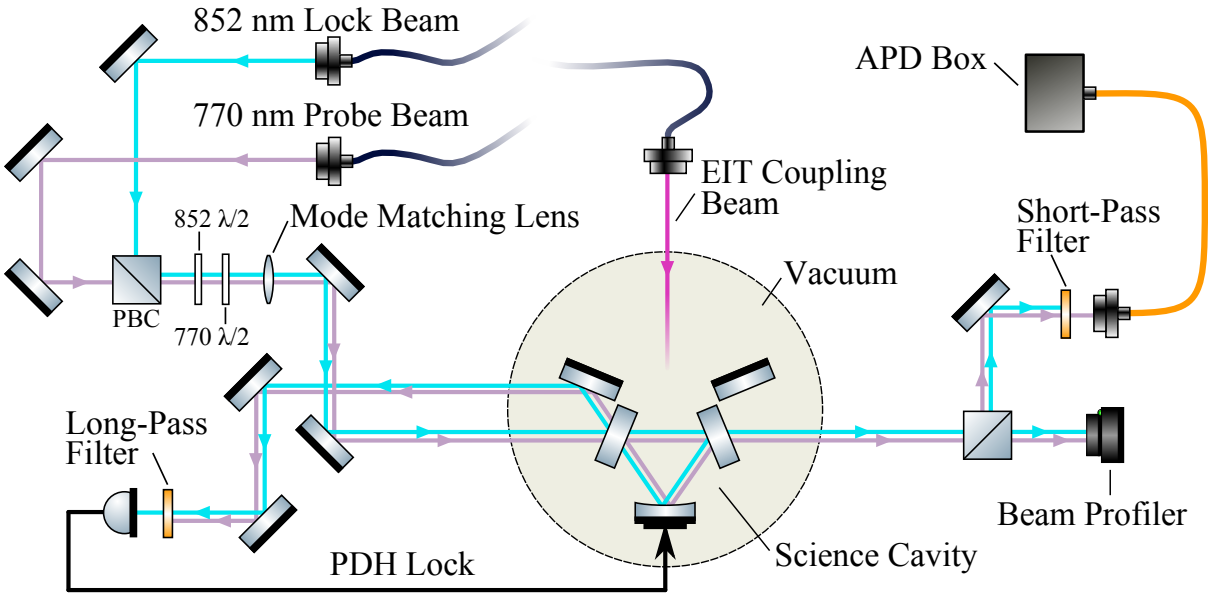


Figure 5.15: Optical setup for input and output of the cavity.

At the output, the transmitted beam passes through a short-pass chromatic filter, which filters off the 852 nm light. The transmitted beam is coupled into a single mode fibre, which takes the 770 nm light to a dark box containing a sensitive avalanche photodetector (Laser Components LCSA500-03 APD).

### 5.4.1 Mode-Matching Optics

Different TEM modes of the cavity will have different resonance frequencies and different atom-cavity coupling rates. Therefore, to know which cavity mode is being excited, the incident beam is matched to a single mode ($TEM_{00}$) of the cavity. This technique is known as mode-matching.

To achieve mode-matching, the size of the beam from the 770 nm fibre output was measured at two positions using a beam profiler. With these measurements the waist size and waist position were deduced, and a complex beam parameter $\mathcal{Q}$ for the initial beam was determined. With this measurement, the ABCD transformations for lenses and displacement (discussed in Section 5.1.4) were used to theoretically match the complex beam parameter $\mathcal{Q}$ for the input light with the complex beam parameter for the cavity $\mathcal{Q}_c$. Using Matlab, $\mathcal{Q}'$ could be found from Equation 5.14, and the positions of the lenses were varied to minimise the value of $|\mathcal{Q}' - \mathcal{Q}_c|$. A variety of setups were simulated using values for the lenses available. The simulations showed that a single biconvex lens with focal length 300 mm resulted in reasonable matching, and thus was implemented in the physical setup close to the position specified by Matlab.

### 5.4.2 Alignment into Correct Mode

Even with the mode-matching optics in place, the light will excite higher-order modes of the cavity if the beam is not correctly aligned into the mode. To correctly align the light into the $TEM_{00}$ mode, the cavity transmission was analysed using a photodiode and beam profiler simultaneously. By changing the cavity length, the $TEM_{00}$ mode can be identified using the beam profiler, as shown in Figure 5.16 and the photodiode can be used to maximise transmission into this mode using the input mirrors, as shown in Figure 5.17.

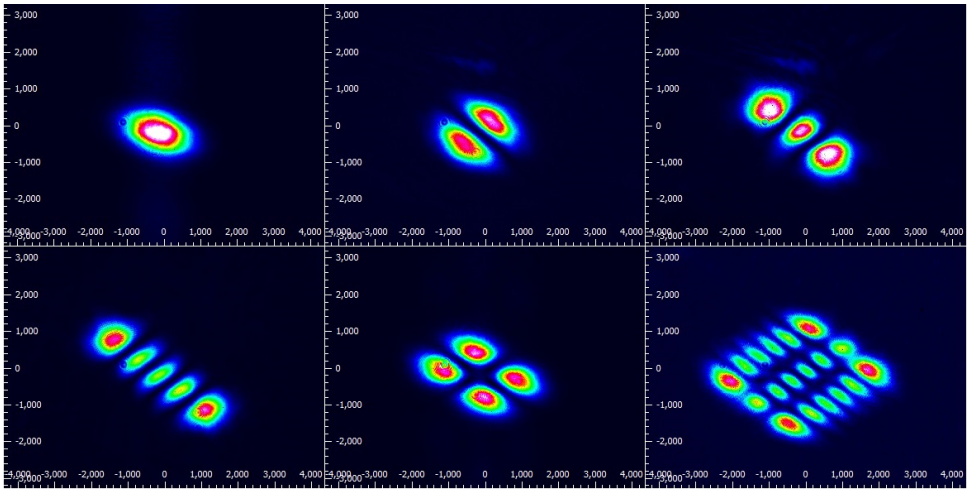

Figure 5.16: Beam profiler images of the cavity transmission.

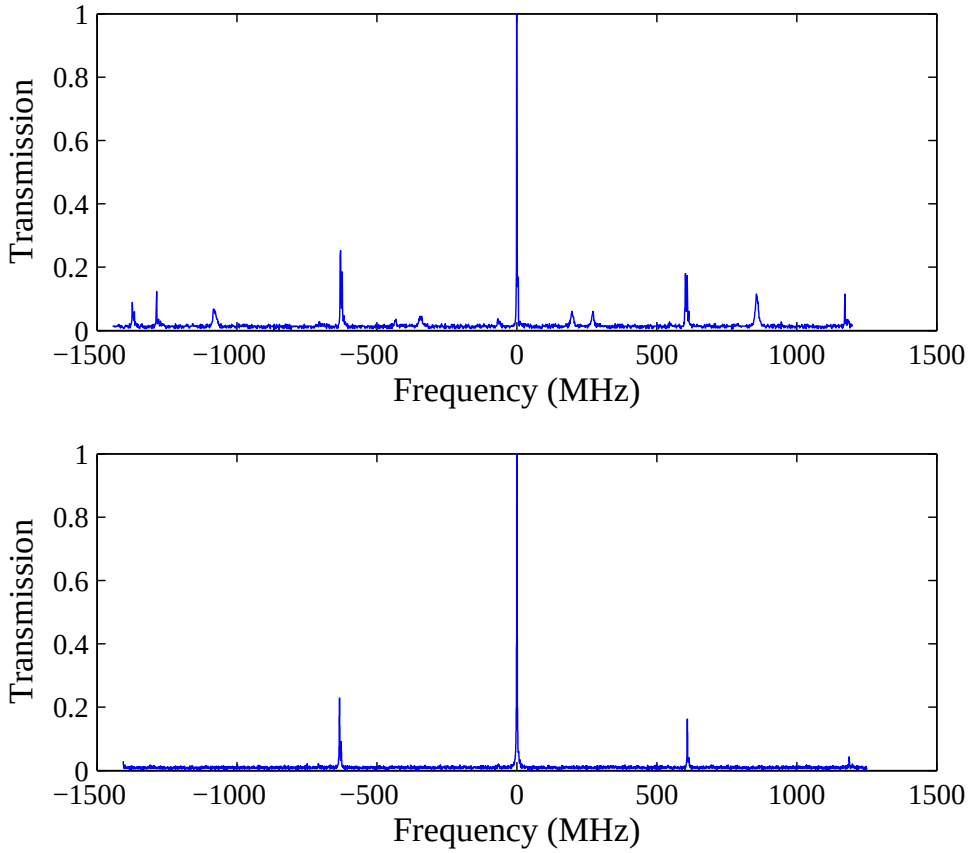


Figure 5.17: Transmission of the optical cavity before (top) and after (bottom) mode-matching.

CHAPTER 6

# Characterisation of the Optical Cavity

From Chapter 2, it was shown that the cavity parameters are important when it comes to understanding the physics of strong coupling. For this reason, this chapter focuses on experimentally measuring the values of the HWHM $\kappa$ (the cavity field decay rate), the cavity mode volume and the mirror reflectivity and transmission coefficients.

## 6.1 Measuring Cavity Linewidth

Here, two different methods are considered for measuring the linewidth of the optical cavity. The first method used is a sideband calibration method, whilst the second technique uses a measurement of the cavity intensity decay rate.

### 6.1.1 Linewidth from Cavity Spectroscopy

Due to the lack of experimental control available during the early stages of the experiment, the cavity linewidth was estimated by taking a transmission spectrum, and calibrating the time axis by modulating the laser current to add sidebands to the probe beam. This method has the benefit that no locking electronics or experimental control are required; however, it suffers from the drawback that the transmission spectrum measured is actually a convolution between the cavity and probe laser spectra, which will lead to a measured transmission spectrum with a larger linewidth than that of the cavity. This should not be an issue if the probe laser linewidth is significantly smaller than the cavity linewidth.

The 770 nm probe laser was scanned using the laser piezo, with a free-running cavity. The transmitted light was detected using the Laser Components LCSA500-03 APD with bandwidth of 3 MHz. The transmission spectrum is shown in Figure 6.1 (left). Sidebands

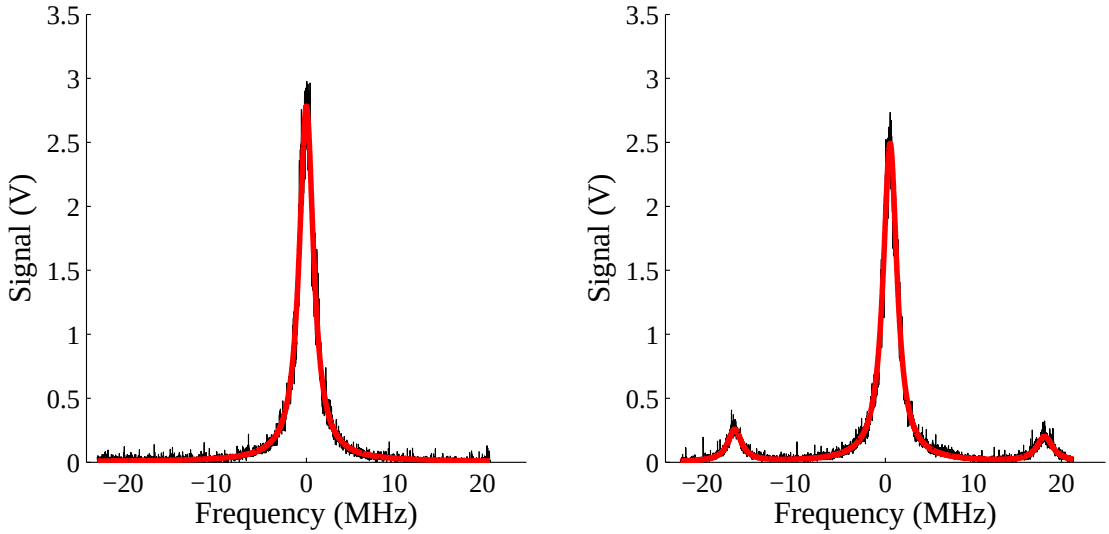


Figure 6.1: Linewidth measurement using sidebands. (Left) Cavity transmission signal. (Right) Modulation is added at 17.5 MHz. The data (black) are fit to Lorentzians (red), which is used to calibrate the x-axis and determine the cavity linewidth.

were then added to the probe laser by modulating the laser current at 17.5 MHz, which is shown in Figure 6.1 (right).

Matlab was used to fit these signals to Lorentzians,

$$S = \sum A \frac{\frac{1}{2}\Delta\nu}{(f - f_0)^2 + \left(\frac{1}{2}\Delta\nu\right)^2} + S_0,$$

where $f_0$ is the centroid and $\Delta\nu$ is the FWHM linewidth. For the calibration data, a sum of three Lorentzians was fitted, and the separation between centroids were used to calibrate the x-axis.

Several sets of data were taken (three here), and the results were averaged to give a cavity HWHM linewidth of $\kappa = 2\pi \cdot (979 \pm 74)$ kHz where the error is the standard error. This measurement has been conducted many times during the lifetime of the experiment in order to detect any degradation of cavity finesse over time due to dispenser usage (as discussed in Section 5.2.1).

Repeating this method for the low finesse polarisation yielded a HWHM linewidth of $\kappa = 2\pi \cdot (4.35 \pm 0.29)$MHz.

### 6.1.2 Linewidth from Cavity Ring-Down Time

The cavity ring-down method involves keeping the probe on resonance with the cavity, and subsequently abruptly shutting the probe light off as quickly as possible. Once the probe light has been switched off, it is possible to detect the decay of the intra-cavity power by monitoring the transmitted light. The cavity ring-down technique is mostly utilised in atomic physics to increase the sensitivity of absorption measurements on atomic samples inside a high finesse cavity[91, 92]; however, here we are only concerned with measuring absorption and losses from the cavity mirrors.

This method is superior to the direct spectroscopy sideband method described previously, since the ring-down time is independent of the probe laser linewidth. However, this method requires locking electronics and a sufficiently high cavity finesse (or a sufficiently high-bandwidth detection system) to capture the decay. Due to the lower finesse for the p-polarisation, it was only possible to take ring-down measurements for the s-polarisation. This technique also requires a fast method of light switching, which most mechanical shutters are much too slow for, and so AOM switching must be used.

The decay time of the transmitted intensity relates directly to the field decay rate $\kappa$,

$$I(t) = I_0 e^{-2t\kappa}, \tag{6.1}$$

where $\kappa$ has been written with units of angular frequency.

All locks in the cavity laser system were enabled, which maintained zero detuning between the cavity resonance and the 770 nm probe frequency. The probe light was pulsed on and off using the double-passed AOM (DPAOM2, Figure 5.11) which has a switching time of around 50 ns. Using a Thorlabs APD110A/M with bandwidth 50 MHz, the ring-down was measured and is shown in Figure 6.2. The data were fit, neglecting data close to the switch-off point, which was skewed due to the AOM switching. Note that an advantage of our laser system is that the system can remain locked whilst the 770 nm probe light is being switched.

A set of four decay curves were fit using Matlab, yielding an average measurement of $\kappa = 2\pi\cdot(920\pm30)$ kHz, where the error is the standard error. The linewidth measurement from this method is slightly narrower than the width measured from the cavity spectroscopy method, but both measurements are within error of one-another.

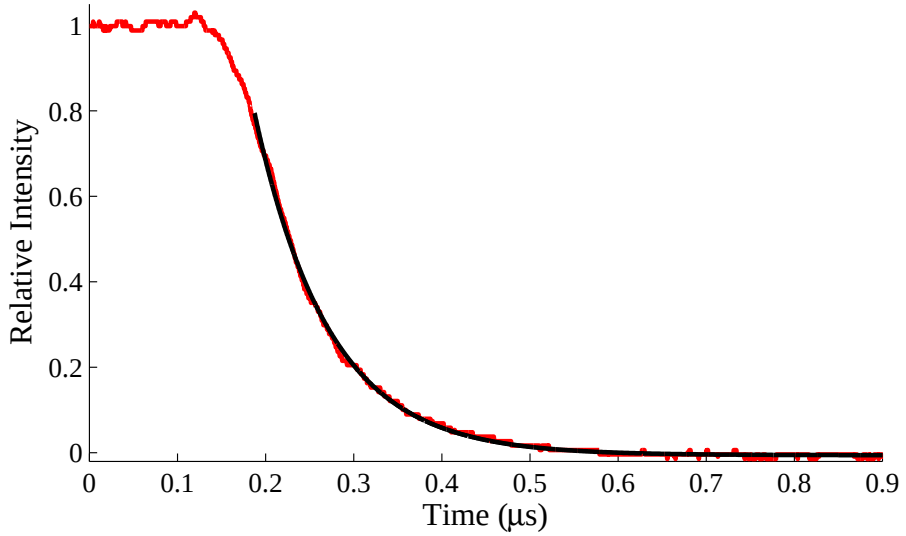


Figure 6.2: Cavity ring-down measurement. The light is switched off around 0.15 µs using the probe DPAOM. The black line shows the fit to decay curve. Data around the switch-off point has been ignored during the fit.

## 6.2 Cavity Mode Volume

From Equation 2.7, it can be seen that the coupling between the atoms and cavity depend on the volume of the cavity mode.

The mode volume can be calculated by

$$V = \int_{-\infty}^{\infty}\int_{-\infty}^{\infty}\int_{-L/2}^{L/2}\left|\frac{E_{m,n}(x,y,z)}{E_0}\right|^2 dx\,dy\,dz, \tag{6.2}$$

where $E_{m,n}$ is the Hermite-Gaussian electric field function from Equation 5.10 and $L$ is the round-trip cavity length. For the TEM (0,0) mode, this becomes,

$$V = \frac{1}{2}\int_{-\infty}^{\infty}\int_{-\infty}^{\infty}\int_{-L/2}^{L/2}\exp\left\{-2\left(\frac{x^2}{w_x^2(z)}+\frac{y^2}{w_y^2(z)}\right)\right\} dx\,dy\,dz, \tag{6.3}$$

where

$$w_{x,y}(z) = w_{0_{x,y}}\sqrt{1+\left(z/z_{R_{x,y}}\right)^2} \quad \text{and} \quad z_{R_{x,y}} = \pi w_{0_{x,y}}^2/\lambda\,.$$

It can be seen that in order to complete this calculation, a value of $L$ and the cavity waists $w_{0_{x,y}}$ are required.

The most straight-forward way to measure the cavity length would be to accurately measure the free spectral range (FSR) frequency, and deduce the length by taking the inverse multiplied by the speed of light. The precision of this method can be improved by using two different wavelengths [93, 94]. However, since the FSR is relatively large in this experiment, it is difficult to accurately measure the FSR without suffering from nonlinear effects from either the laser scan or the cavity scan. Instead, the transverse mode spacing was used to measure the length. From Equation 5.20, we saw that the frequencies of the transverse modes are dependent on the focal properties of the cavity. By measuring the frequency spacing between the transverse modes, the cavity length $L$ and mode waists $w_{0_{x,y}}$ were obtained.

### 6.2.1 Measurement of Transverse Mode Splitting

Using the 770 nm light in the s-polarisation, the cavity was deliberately misaligned in order to excite several high-order TEM modes. Using the beam profiler, several modes were identified. A close-up of a group of these modes is displayed in Figure 6.3, whilst the full free spectral range of the misaligned cavity is shown in Figure 6.4.

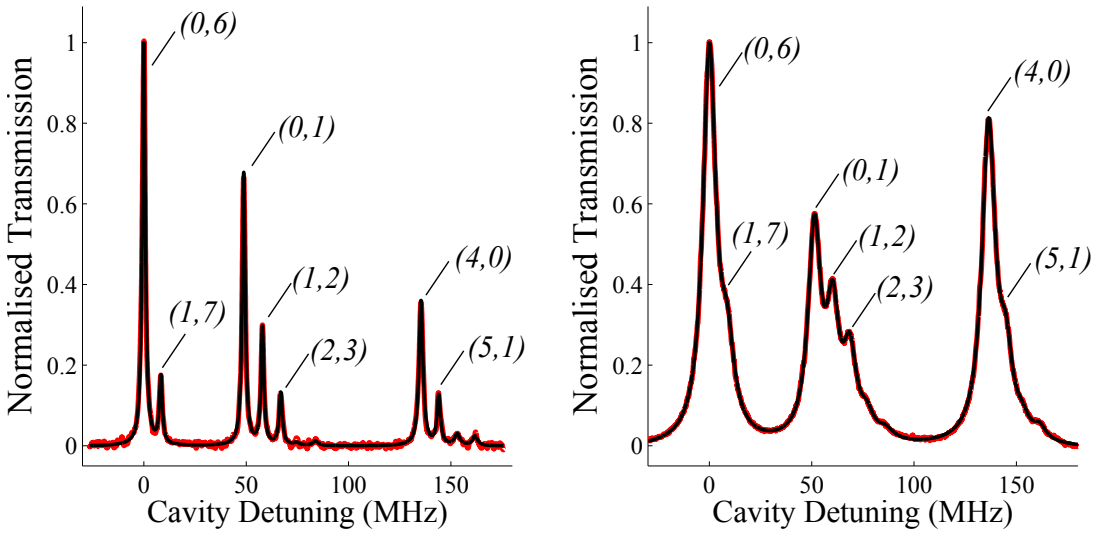


Figure 6.3: A group of closely-spaced TEM modes $(m, n)$ for s-polarisation (left) and p-polarisation (right) for 770 nm light. To deduce frequency splitting, the data (red lines) are fit to a sum of Lorentzians (black lines). Longitudinal mode numbers have been ignored.

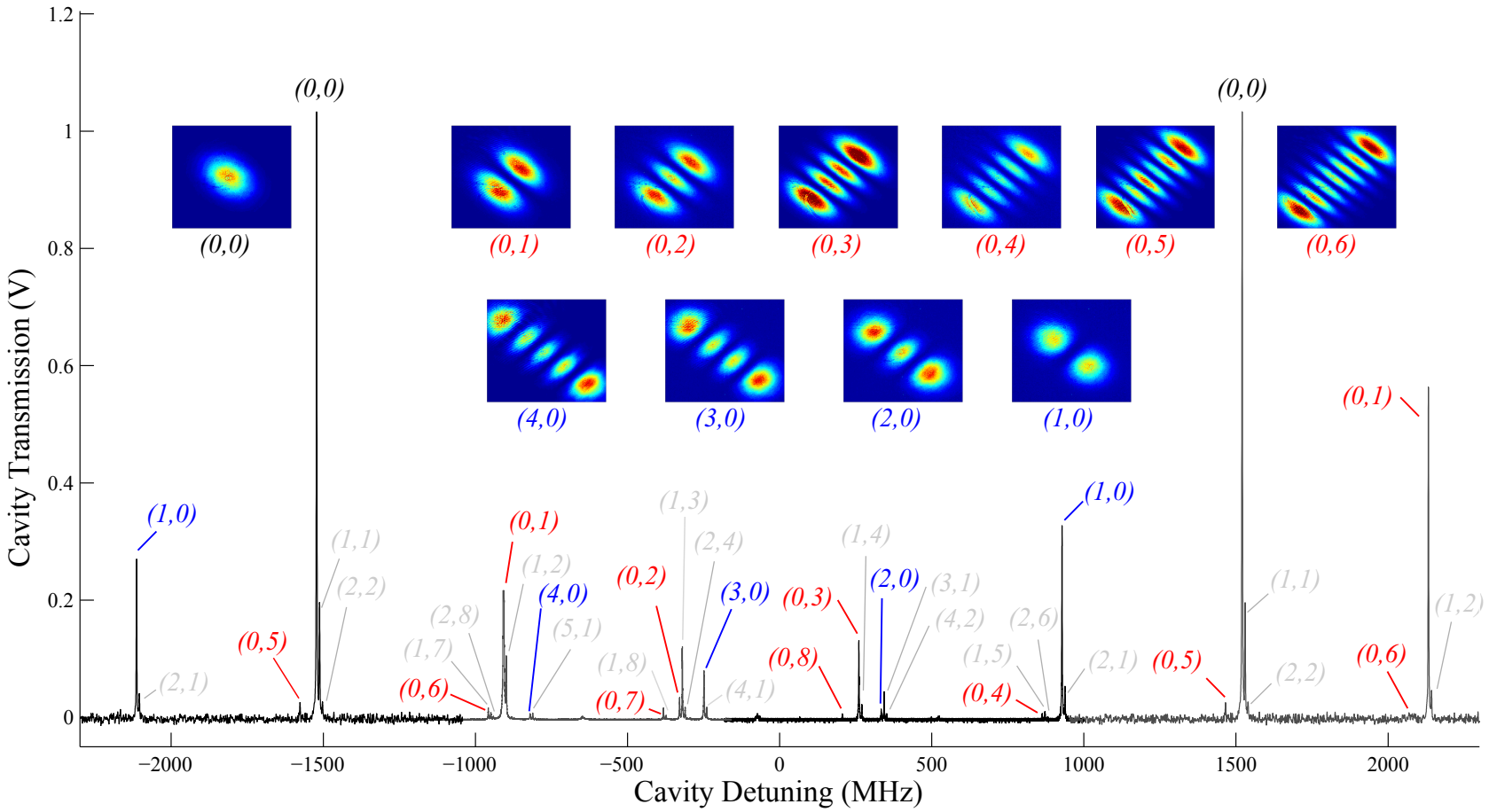


Figure 6.4: A free spectral range of the misaligned cavity, for the s-polarised light. Many high-order modes $(m, n)$ are visible, where $m, n$ are the transverse mode numbers. Inset are several beam profiler images. These images appear at 45° due to the angle of the cavity plane with respect to the optical table. To guide the eye, $(m, 0)$ modes have been highlighted in blue, and $(0, n)$ highlighted in red. Higher order modes are labeled in grey. Plotted data are from several scope traces (to maintain $x$-resolution), which have been stitched together.

It can be seen that the modes appear in groups of $(m, n)$, $(m+1, n+1)$, $(m+2, n+2)$. These modes are only spaced by around 10 MHz and are easy to measure without distortion arising due to nonlinear effects from the laser or cavity scan. It is possible to measure the spacing using the sideband method discussed in Section 6.1.1; however, if many modes are in the vicinity of interest, the sideband method becomes difficult due to the fitting of many overlapping Lorentzians. In this case, the $D_1$ spectroscopy (shown in Figure 5.14) can be used. The hyperfine splitting of the the $D_1$ line of $^{39}$K is 55 MHz [95] and is easily resolvable with the Doppler-free saturated absorption spectroscopy.

Using a combination of both measurement techniques, several consecutive spacings were measured, and are displayed on Table 6.1. Using these measurements with Equation 5.21, and using a radius of curvature of $(10.00 \pm 0.05)$cm (as specified by the manufacturer), $L$ was deduced to be $(9.51 \pm 0.12)$cm. This is slightly shorter than the intended design length of 9.66 cm, most likely due to errors when gluing the side mirrors onto the vee-grooves.

| Modes $(m, n)$ | Measured Spacing (MHz) |
|---|---|
| $(0, 0)$ to $(1, 1)$ | $10.4 \pm 0.3$ |
| $(0, 2)$ to $(1, 3)$ | $10.1 \pm 0.3$ |
| $(0, 5)$ to $(1, 6)$ | $10.5 \pm 0.3$ |
| $(0, 7)$ to $(1, 8)$ | $9.1 \pm 0.2$ |
| $(1, 1)$ to $(2, 2)$ | $9.1 \pm 0.3$ |
| $(1, 3)$ to $(2, 4)$ | $10.1 \pm 0.3$ |
| $(2, 2)$ to $(3, 3)$ | $10.1 \pm 0.3$ |
| $(3, 0)$ to $(4, 1)$ | $9.1 \pm 0.3$ |

Table 6.1: Measurements of frequency spacing between consecutive $(m, n)$ to $(m+1, n+1)$ modes.

After $L$ was obtained from the small spacings between the consecutive modes, measured values for larger mode spacings (with larger errors) were compared to the theoretical values and are shown in Table 6.2. It can be seen that there is good agreement, suggesting that the cavity length has been reliably estimated.

The spectra for the p-polarisation and 852 nm light were also partially analysed, and as expected, no differences in spacings were found between the different polarisations and wavelengths. Due to the narrower linewidth, it was much easier to resolve separate modes using the s-polarisation, and the 770 nm light was more useful due to the availability of the $D_1$ potassium spectrum.

| Modes $(m, n)$ | Measured Spacing (MHz) | Estimated Spacing (MHz) |
|---|---|---|
| $(0,0)$ to $(0,2)$ | $1237 \pm 37$ | 1241 |
| $(0,0)$ to $(0,1)$ | $613 \pm 6$ | 620 |
| $(0,2)$ to $(2,0)$ | $663 \pm 20$ | 688 |
| $(0,2)$ to $(3,0)$ | $83 \pm 3$ | 78 |
| $(0,4)$ to $(1,0)$ | $64 \pm 2$ | 58 |
| $(0,5)$ to $(0,0)$ | $64 \pm 2$ | 48 |
| $(0,6)$ to $(4,0)$ | $142 \pm 4$ | 135 |
| $(0,7)$ to $(0,2)$ | $55 \pm 2$ | 48 |
| $(1,0)$ to $(0,0)$ | $602 \pm 18$ | 611 |

Table 6.2: Measured values of frequency spacing between larger-spaced modes, compared to estimated spacings obtained using calculated cavity length.

### 6.2.2 Mode Structure of the Cavity Spectrum

From Section 5.1.6, the resonance condition was found to be

$$\nu_{m,n,q} = \frac{\nu_{\text{FSR}}}{2\pi}\left\{\left(m+\frac{1}{2}\right)\cos^{-1}\left(1-\frac{L}{\mathcal{R}_x}\right)+\left(n+\frac{1}{2}\right)\cos^{-1}\left(1-\frac{L}{\mathcal{R}_y}\right)+\phi_{mM}+2\pi q\right\}, \tag{6.4}$$

where $\nu_{\text{FSR}}$ is the free spectral range (in Hertz), $q$ is the longitudinal mode number, $\mathcal{R}_x$ and $\mathcal{R}_y$ are the effective radii of curvature of the central mirror in the $x$ and $y$ directions, and $\phi_{mM}$ is the phase shift due to the mirror reflections. As described in Section 5.1.3, $\phi_{mM}$ can be ignored for cavities with an even number of mirrors $M$, however it cannot be ignored for our cavity. This phase shift $\phi_{mM}$ is equal to 0 when the transverse mode number $m$ is even, and equal to $\pi$ when $m$ is odd. It should be noted that $\phi_{mM}$ does not depend on the transverse mode number $n$. This information will now be used to understand the mode structure of the cavity spectrum in Figure 6.4.

From Figure 6.4, it can be seen that that the $(0,n)$ modes increase in frequency from the $(0,0)$ mode. The spacing between $(0,n)$ and $(0,n+1)$ is a fixed amount corresponding to

$$\nu_{m,n+1,q} - \nu_{m,n,q} = \frac{\nu_{\text{FSR}}}{2\pi}\cos^{-1}\left(1-\frac{L}{\mathcal{R}_y}\right). \tag{6.5}$$

Now considering the $(m,0)$ modes, the spacing between $(m,0)$ and $(m+1,0)$ is

$$\nu_{m+1,n,q} - \nu_{m,n,q} = \frac{\nu_{\text{FSR}}}{2\pi}\cos^{-1}\left(1-\frac{L}{\mathcal{R}_x}\right) \pm \frac{\nu_{\text{FSR}}}{2}, \tag{6.6}$$

where the mode spacing $\nu_{m+1,n,q} - \nu_{m,n,q}$ is an additional $\nu_{\text{FSR}}/2$ when measuring from an odd value of $m+1$ to an even value $m$, but $\nu_{\text{FSR}}/2$ less when measuring from an even value of $m+1$ to an odd value of $m$. This is counter-intuitive and theoretical values of mode spacing between $(0,0)$ and the $(0,n)$ and $(m,0)$ modes are given in Table 6.3.

| $m$ | Shift/$\nu_{\text{FSR}}$ |
|---|---|
| 0 | 0.00 |
| 1 | 0.81 |
| 2 | 0.61 |
| 3 | 1.42 |
| 4 | 1.22 |
| 5 | 2.03 |
| 6 | 1.84 |

| $n$ | Shift/$\nu_{\text{FSR}}$ |
|---|---|
| 0 | 0.00 |
| 1 | 0.20 |
| 2 | 0.39 |
| 3 | 0.59 |
| 4 | 0.79 |
| 5 | 0.98 |
| 6 | 1.18 |

Table 6.3: Frequency shifts of $(m,0)$ and $(0,n)$ with respect to the $(0,0)$ mode.

Hence, whilst it may initially appear from Figure 6.4 that the $(m,0)$ modes decrease in frequency from the $(0,0)$ mode in fixed steps (in a manner which mirrors the behavior of the $(0,n)$ modes), this is definitely not the case. The phase shifts due to mirror reflections shuffle the order of the $(m,0,q)$ modes such that their order for each longitudinal mode $q$ becomes $m = 0,2,1,4,3$, and so on. Coincidentally, this appears as $4,3,2,1,0$ when overlapped with other longitudinal modes in the cavity transmission spectrum.

### 6.2.3 Deducing the Cavity Mode Volume

Using the ABCD matrix calculation from Section 5.1.5, and the cavity length measurement $L = (9.51 \pm 0.12)$cm obtained in the previous section, the waists were determined to be $w_{0_x} = (90.2 \pm 1.1)$µm and $w_{0_x} = (128.0 \pm 0.8)$µm. From Equation 6.3, this yields a cavity mode volume for the (0,0) mode of $V = (2.40 \pm 0.07)\text{mm}^3$.

Using these values to calculate $g$,

$$g = \sqrt{\frac{|\mu|^2 \omega_c}{2\hbar\epsilon_0 V}}, \tag{6.7}$$

the single atom, single photon atom-cavity coupling rate was calculated to be $g = 2\pi \cdot (91.5 \pm 1.2)$kHz.

## 6.3 Estimating the R and T Coefficients

It has been assumed repeatedly in the theory sections of this thesis that the cavity probe beam is 'weak'. In order to deduce the intra-cavity power, the transmission and reflectivity coefficients of the mirrors were deduced.

Using a photodiode placed before the APD fibre, the input light was mode-matched and aligned into the cavity as best as possible. The transmission spectrum was fit(shown in Figure 6.5), and by comparing peak intensities it was deduced that 80.2% of the 770 nm light was exciting the $TEM_{0,0}$ mode of the cavity.

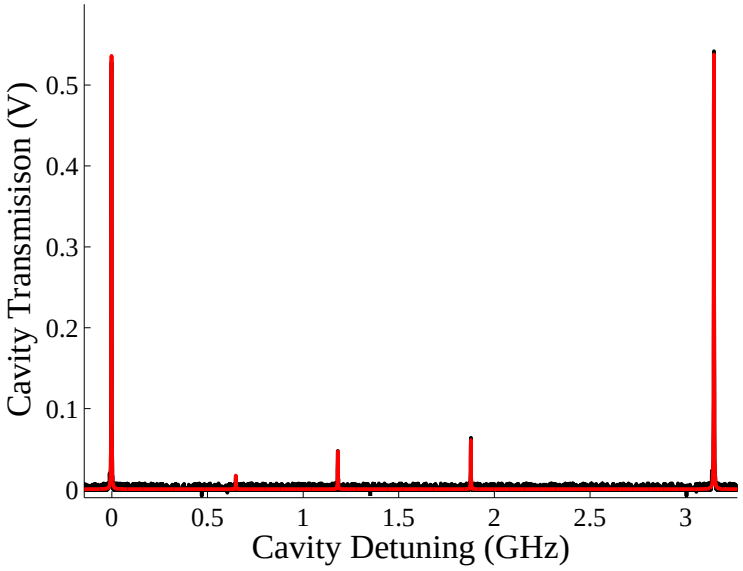


Figure 6.5: A mode-matched free spectral range of the cavity. The data (black line) were fit (red line) to deduce that 80.2% of the incident light excites the $TEM_{0,0}$ mode (large peaks at 0 and 3.15 GHz).

Prior to locking, the current modulation for the 770 nm was turned on, which reduced the carrier intensity to 82.8%, which was deduced by fitting. This intensity was further reduced to 88.1% due to the short-pass filter, placed after the cavity. Once the laser system and cavity were locked, the transmitted $TEM_{0,0}$ carrier power after the short-pass filter was 24.1% of the total incident power. Correcting for the reductions due to imperfect mode-matching, the modulation and the filter, the transmission becomes 41.1%. The total reflected power was deduced in a similar manner to be 2.29%.

Repeated measurements yielded reflected and transmitted fractions of $(2.8 \pm 0.7)\%$ and $(40.3 \pm 0.8)\%$. With the finesse from the ring-down measurement, there are a total of

three measurements. There are also three parameters we wish to deduce: the reflectivity coefficient of the side mirrors, the reflectivity coefficient of the central mirror, and the transmission coefficient of the side mirrors. The distribution of losses for the central mirror (between transmission or absorption) do not affect the three measurements made here. Since the side mirrors were coated in the same batch and are used with the same angle of incidence, it was assumed that the transmission and reflection coefficients for the side mirrors are identical. Using the theory outlined in Section 5.1.1, the parameters were deduced to be within the nominal ranges from the manufacturer (Layertek, batch no. C213A051), and are summarised in Table 6.4.

| Parameter | Measured Value (%) | Nominal Value (%) |
|---|---|---|
| $R_{1,2}$ (sides) | $99.848 \pm 0.003$ | $99.86 \pm 0.02$ |
| $R_3$ (central) | $99.938 \pm 0.007$ | $99.96 \pm 0.02$ |
| $T_{1,2}$ (sides) | $0.116 \pm 0.001$ | not specified |

Table 6.4: Transmission and reflection coefficients for the mirrors of the cavity.

Using these coefficients, it was estimated that for a cavity probe with incident power 1 nW, that the intra-cavity photon number is roughly 500.

# CHAPTER 7

# Collective Strong Coupling

In previous chapters, it has been shown how our system can be used to create a cloud of cold potassium atoms. The characterisation of the optical ring cavity has also been discussed, where the cavity loss rate and volume of the $TEM_{0,0}$ mode were deduced. In this chapter, we bring the two systems together and demonstrate that we have an atom-cavity system.

## 7.1 Predicting the Rabi Frequency

Using the techniques described earlier it was deduced that on the day the following results were taken, the total number of atoms in the 3D MOT was $(1.86 \pm 0.07) \times 10^6$ with an estimated $N = (2.30 \pm 0.04) \times 10^4$ atoms overlapping with the cavity mode. It should be noted that the following data were collected shortly after a period of hiatus for the experiment - the pressure in the vacuum chambers had dropped lower than their usual values and thus the number of atoms here are small compared to the usual atom numbers seen in this experiment. As will be discussed in the next chapter, this atom number has since returned to its usual values.

The effective number of atoms [96] is given by $N_{eff} = N \cdot (5/18)$ , where the factor of $5/18$ is the average relative strengths for all $F = 1 \leftrightarrow F' = 2$ transitions. The mode volume deduced in the previous section was found to be $(2.40 \pm 0.07)\text{mm}^3$ and the single atom Rabi frequency $g$ has been calculated to be $(91.5 \pm 1.2)$kHz. Bringing all of this together, the estimated Rabi frequency $G = \sqrt{N}g$ for this number of atoms is expected to be around $(7.31 \pm 0.16)$MHz.

## 7.2 Demonstration of Collective Strong Coupling

To detect normal-mode splitting and the avoided crossing due to the atom-cavity interaction, the resonant frequency of the cavity $\omega_c$ as well as the frequency of the cavity probe

beam $\omega_p$ must be swept across the atomic resonance $\omega_a$, and thus two parameters must be varied: the cavity-atom and probe-atom detunings, $\Delta_{ca} = \omega_c - \omega_a$ and $\Delta_{pa} = \omega_p - \omega_a$. As described in Section 5.3, our laser system has been designed to allow us to control both of these detunings.

Using the computer control system (described in Appendix A), the cavity length was set to a particular value of $\Delta_{ca}$, and a MOT was loaded into the cavity mode. Once the MOT was loaded, the repump beam was turned off for a period of 100 µs using the repump DPAOM, in order to pump the atoms into the $F = 1$ ground state. The cooling beam was then also turned off for a period of 100 µs. During this period, the cavity probe beam was turned on and scanned across a frequency range of $\Delta_{pa}$, and the cavity transmission was detected. Once the probe scan had completed, the MOT beams were turned back on and the MOT was reestablished. As described in Section 4.4.3, the change in line density along the cavity mode due to thermal expansion during this scan period is believed to be small.

Due to the low intensity of the probe beam (1 nW at the input), the cavity transmission signal is small with respect to the electrical noise, and so the probe scan was repeated eight times at (a rate of 5 Hz) and averaged to improve the clarity of the signal. The cavity detuning was then stepped to a different value of $\Delta_{ca}$, and the measurement was repeated. Using this sequence, normal-mode splitting was observed, and the data are shown and Figure 7.1. A single slice corresponding to $\Delta_{ca} = 0$ is shown in Figure 7.2.

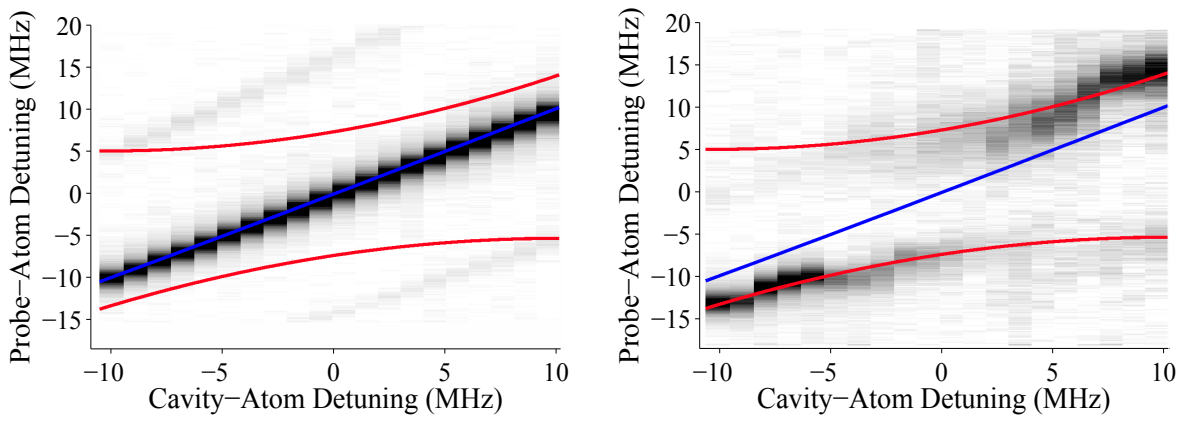


(a) Bare Cavity System

(b) Atom-Cavity System

Figure 7.1: Two-dimensional data showing the transmission of the cavity with and without atoms present. The black and white scale shows the intensity of the cavity transmission, the blue line shows the fit to the bare cavity, and the red lines show the fit to the atom-cavity system. The faint grey lines in (a) are the sidebands from the laser current modulation.

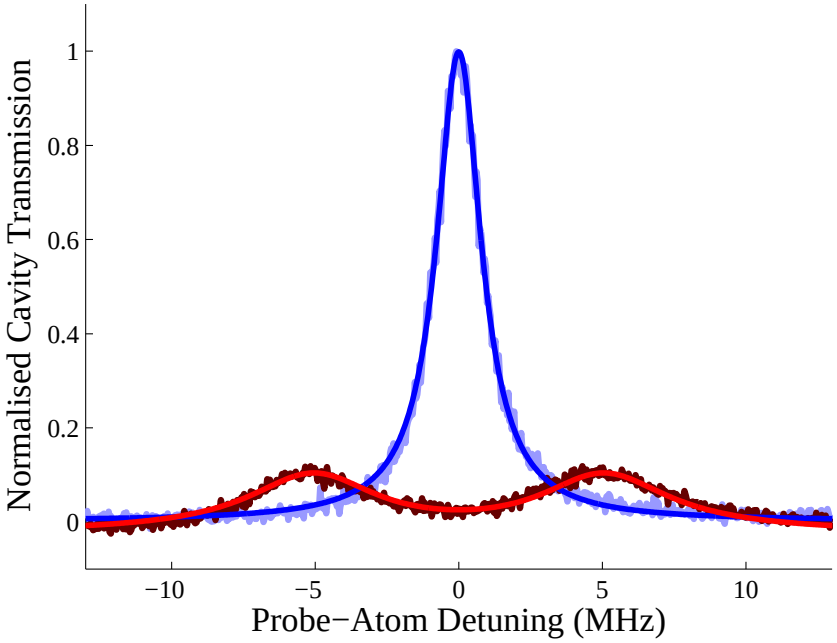


Figure 7.2: Normalised transmission of the cavity at $\Delta_{ca} = 0$ with and without atoms present. The light blue and bright blue lines show the data and fit for the bare cavity, and the dark red and bright red lines show the data and fit when atoms are present. In these traces, the oscilloscope was set to average over 64 shots.

Three sets of results were fit using Equation 2.20 to give a collective coupling rate of $G = (6.25 \pm 0.50)$MHz, where the error is given by the standard error. This is slightly smaller than the predicted rate of $(7.31 \pm 0.16)$MHz for this number of atoms. A likely reason for this discrepancy is incorrect overlap between the 3D MOT and the cavity mode. Although the 3D MOT position had been roughly optimised by moving the magnetic field zero, and by making small tweaks to the MOT beam alignment in order to maximise the splitting, it is possible that the MOT position required further optimisation.

## 7.3 Concluding Statements

Figures 7.1 and 7.2 show that collective strong coupling between the atoms and the optical ring cavity has been successfully achieved in this experiment. Although collective strong coupling between atoms and cavities has been demonstrated previously by many experiments, we believe this is the first experiment to demonstrate strong coupling using potassium [19]. Not only has this effect been seen, but the use of a 2D MOT as an

atom source has allowed us to maintain low pressure in the 3D MOT chamber and thus maintain a high cavity finesse for extended operation.

The next aim of this experiment is to modify the group refractive index of the atoms within the MOT using nonlinear optical techniques such as electromagnetically-induced transparency (EIT). As described earlier, such techniques require coherent control beams and hence this is where potassium is advantageous, since the narrow ground state splitting allows us to create coherent control beams easily using only acousto-optical modulators, allowing us to circumvent more complex injection-locking techniques.

Whilst other experiments have already demonstrated a controllable group index inside an optical cavity with cold atoms, the field remains relatively unexplored with applications in active atomic clocks and enhanced-sensitivity laser ring gyroscopes [12, 13, 97, 98]. Note that other experiments using standard linear cavities are unable to explore enhanced-sensitivity ring gyroscopes, and hence this is an attractive avenue of exploration in the long-term future of this experiment.

# CHAPTER 8

# Current Status and Outlook

This thesis has described the setup, optimisation and characterisation of a system which demonstrates collective strong coupling between potassium atoms and an optical ring cavity. Since my departure from the laboratory, the intra-cavity atom number has been increased from $4.7 \times 10^3$ to $4.9 \times 10^4$, and the collective Rabi frequency $G$ has been increased from $2\pi \times 6.25$MHz to $2\pi \times 20$MHz. This was achieved after replacing the elongated rectangular 3D MOT coils with a pair of circular anti-Helmholtz style coils.

The elongated coils were replaced for several reasons; partially due to the significant thermal damage incurred by two of the four coils, partially due to the more stringent cavity-MOT alignment requirements when working with an elongated MOT, and partially due to concerns that the cloud temperature was too high to observe electromagnetically-induced transparency (EIT, which is currently the next major goal in the experiment) due to thermal decoherence effects. Since my departure, the 3D MOT temperature has been reduced to around 150 µK by using the computer control to quickly jump the detuning of the MOT beams. This temperature is still above the Doppler temperature, and could still be reduced further using sub-Doppler cooling methods [99, 100, 101]. Although further reduction in temperature is possible, it is likely unnecessary, since the decoherence rate due to Doppler broadening at this temperature should small ($\sim 100$ kHz) and is unlikely to limit the EIT effect.

In search of the intra-cavity EIT, we can be confident that the laser system is operating correctly since we have observed EIT in a vapour cell [18]. In this case, the probe beam and coupling beam were co-propagating, and were therefore addressing the same atomic velocity class, removing the effects of Doppler shifts. In the atom-cavity setup however, the EIT coupling beam is perpendicular to the probe beam, and so this is not necessarily the case, although, as described in the previous paragraph, the Doppler shift should be negligibly small.

A more likely reason for the absence of the EIT effect is the presence of the magnetic field produced by the anti-Helmholtz coils. Across the cloud, the maximum Zeeman splitting is roughly estimated to be $\sim 0.4$ MHz, which could lead to significant decoherence and so the magnetic field may need to be turned off prior to the cavity probing interval. Turning off

the field introduces its own problems however, such as eddy currents, vibrations causing the cavity length to change, and since there is no proper Earth-field compensation system, atoms are blown out of the MOT region during the magnetic field switch-off.

Although the experiment is not currently demonstrating intra-cavity EIT, we can still consider the theoretical spectrum. In Figure 8.1, the cavity transmission is plotted with and without the EIT coupling beam using the parameters for this experiment where $G = 20\,\text{MHz}$. It can be seen that not only does the transparency window appear, but also the separation between the peaks from the normal-mode splitting is increased slightly. Preliminary experiments do indeed show an increase in the separation of these peaks when the coupling beam is turned on, however no EIT window has been seen.

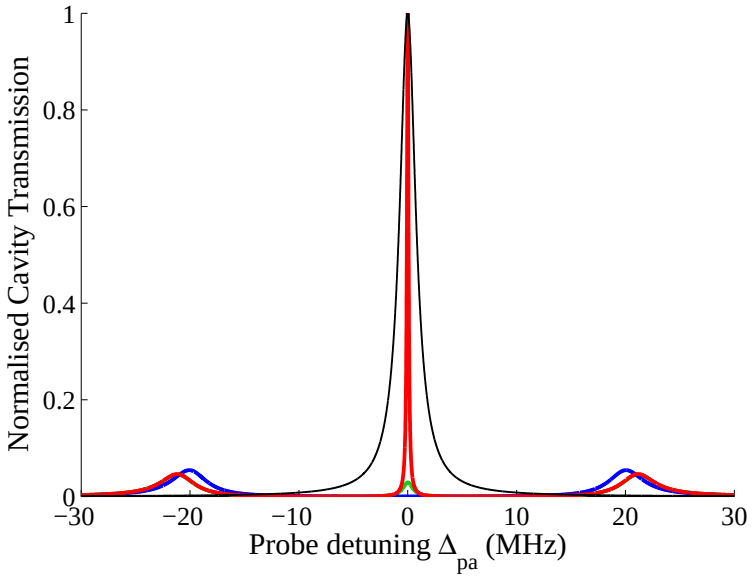


Figure 8.1: Theoretically predicted transmission of the cavity obtained from Equation 2.55. The black line shows the cavity transmission when no atoms are present ($G = 0$). The blue line shows the transmission for $G = 2\pi \times 20\,\text{MHz}$ and with no EIT coupling beam ($\Omega_c = 0$). The red and green lines then show the cavity transmission when the EIT coupling light is turned on ($\Omega_c = 2\pi \times 13.3\,\text{MHz}$), for decoherence rate $\gamma_{deph} = 0$ and $1\,\text{MHz}$ respectively. In all traces, $\kappa = 2\pi \times 0.92\,\text{MHz}$ and $\gamma = 2\pi \times 2.98\,\text{MHz}$.

Once the EIT transmission window is observed in the cavity, we wish to demonstrate the modification of the group index by measuring the modified cavity ring-down time [98, 102, 103].

# Acknowledgements

Firstly, I thank my supervisor Jon Goldwin and the rest of the Cold Atoms group for giving me the opportunity to work and study in such a fascinating and beautiful area of science. I would like to also thank Lawrence and Komal for being fantastic role models during my first two years in the group; even since your departure from the project, you guys have continued to inspire and motivate me. Mike, you were also a great help during your short stay in our lab.

I would also like to thank my excellent labmate Andreas for making this experience much more bearable. Not only has Andreas been indispensable to brainstorm ideas and discuss the physics with, he's been extremely helpful in the lab too - especially whenever a fibre tip needed polishing. Andreas, I hope your write-up goes smoothly and I wish you the best of luck with the future. To Balázs and Graeme, I hope you enjoy taking over from Andreas and me; I hope the mirrors stay clean for you guys.

A special thanks goes to Ruby for her loving encouragement and moral support at the end of every day, and my family for their unfaltering patience over the past few years.

# References


[1] E. M. Purcell. Spontaneous emission probabilities at radio frequencies. *Physical Review*, 69:681, 1946.

[2] P. Goy, J. M. Raimond, M. Gross, and S. Haroche. Observation of cavity-enhanced single-atom spontaneous emission. *Physical Review Letters*, 50:1903–1906, 1983.

[3] S. Haroche and D. Kleppner. Cavity quantum electrodynamics. *Physics Today*, 42(1):24, 1989.

[4] H. Walther, B. T. H. Varcoe, B. G. Englert, and T. Becker. Cavity quantum electrodynamics. *Reports on Progress in Physics*, 69(5):1325, 2006.

[5] J. I. Cirac, P. Zoller, H. J. Kimble, and H. Mabuchi. Quantum state transfer and entanglement distribution among distant nodes in a quantum network. *Physical Review Letters*, 78:3221–3224, 1997.

[6] M. Brune, S. Haroche, J. M. Raimond, L. Davidovich, and N. Zagury. Manipulation of photons in a cavity by dispersive atom-field coupling: Quantum-nondemolition measurements and generation of "Schrödinger cat" states. *Physical Review A*, 45:5193–5214, 1992.

[7] W. Lu, Y. Zhao, and P. F. Barker. Cooling molecules in optical cavities. *Physical Review A*, 76:013417, 2007.

[8] E. T. Jaynes and F. W. Cummings. Comparison of quantum and semiclassical radiation theories with application to the beam maser. *Proceedings of the IEEE*, 51(1):89–109, 1963.

[9] B. W. Shore and P. L. Knight. The Jaynes-Cummings model. *Journal of Modern Optics*, 40(7):1195–1238, 1993.

[10] M. Tavis and F. W. Cummings. Exact solution for an N-molecule radiation-field Hamiltonian. *Physical Review*, 170:379–384, 1968.

[11] R. W. Boyd. Slow and fast light: fundamentals and applications. *Journal of Modern Optics*, 56(18-19):1908–1915, 2009.

[12] M. A. Norcia and J. K. Thompson. Cold-strontium laser in the superradiant crossover regime. *Physical Review X*, 6:011025, 2016.

[13] J. G. Bohnet, Z. Chen, J. M. Weiner, D. Meiser, M. J. Holland, and J. K. Thompson. A steady-state superradiant laser with less than one intracavity photon. *Nature*, 484:78–81, 2012.

[14] M. S. Shahriar, G. S. Pati, R. Tripathi, V. Gopal, M. Messall, and K. Salit. Ultrahigh enhancement in absolute and relative rotation sensing using fast and slow light. *Physical Review A*, 75:053807, 2007.

[15] K. U. Schreiber and J. P. Wells. Invited review article: Large ring lasers for rotation sensing. *Review of Scientific Instruments*, 84(4), 2013.

[16] M. Fleischhauer, A. Imamoglu, and J. P. Marangos. Electromagnetically induced transparency: Optics in coherent media. *Reviews of Modern Physics*, 77:633–673, 2005.

[17] L. V. Hau, S. E. Harris, Z. Dutton, and C. H. Behroozi. Light speed reduction to 17 metres per second in an ultracold atomic gas. *Nature*, 425:594–598, 1998.

[18] A. Lampis, R. Culver, B. Megyeri, and J. Goldwin. Coherent control of group index and magneto-optical anisotropy in a multilevel atomic vapor. *Optics Express*, 24:15494–15505, 2016.

[19] R. Culver, A. Lampis, B. Megyeri, K. Pahwa, L. Mudarikwa, M. Holynski, P. W. Courteille, and J. Goldwin. Collective strong coupling of cold potassium atoms in a ring cavity. *New Journal of Physics*, 18(11):113043, 2016.

[20] C. Gerry and P. Knight. *Introductory Quantum Optics*. Cambridge University Press, Cambridge, 2004.

[21] P. Meystre and M. Sargent III. *Elements of Quantum Optics*. Springer, Berlin, 1999.

[22] C. Cohen-Tannoudji, J. Dupont-Roc, and G. Grynberg. *Atom-Photon Interactions*. Wiley, 2010.

[23] M. G. Raizen, R. J. Thompson, R. J. Brecha, H. J. Kimble, and H. J. Carmichael. Normal-mode splitting and linewidth averaging for two-state atoms in an optical cavity. *Physical Review Letters*, 63:240–243, 1989.

[24] Y. Zhu, D. J. Gauthier, S. E. Morin, Q. Wu, H. J. Carmichael, and T. W. Mossberg. Vacuum rabi splitting as a feature of linear-dispersion theory: Analysis and experimental observations. *Physical Review Letters*, 64:2499–2502, 1990.

[25] R. J. Thompson, G. Rempe, and H. J. Kimble. Observation of normal-mode splitting for an atom in an optical cavity. *Physical Review Letters*, 68:1132–1135, 1992.

[26] R. J. Brecha, L. A. Orozco, M. G. Raizen, M. Xiao, and H. J. Kimble. Observation of oscillatory energy exchange in a coupled-atom–cavity system. *Journal of the Optical Society of America B*, 12(12):2329–2339, 1995.

[27] M. Brune, F. Schmidt-Kaler, A. Maali, J. Dreyer, E. Hagley, J. M. Raimond, and S. Haroche. Quantum Rabi oscillation: A direct test of field quantization in a cavity. *Physical Review Letters*, 76:1800–1803, 1996.

[28] A. Kuhn and G. Rempe. Optical cavity QED: fundamentals and application as a single-photon light source,. In F. De Martini and C. Monroe, editors, *Summer School: Experimental Quantum Computation and Information*, pages 37–66, Amsterdam, IOS Press. 2002.

[29] A. Wickenbrock, P. Phoonthong, and F. Renzoni. Collective strong coupling in a lossy optical cavity. *Journal of Modern Optics*, 58(15):1310–1316, 2011.

[30] R. H. Dicke. Coherence in spontaneous radiation processes. *Physical Review*, 93:99–110, 1954.

[31] M. Tavis and F. W. Cummings. Approximate solutions for an N-molecule-radiation-field Hamiltonian. *Physical Review*, 188:692–695, 1969.

[32] G. S. Agarwal. Vacuum-field Rabi splittings in microwave absorption by Rydberg atoms in a cavity. *Physical Review Letters*, 53:1732–1734, 1984.

[33] B. M. Garraway. The dicke model in quantum optics: Dicke model revisited. *Philosophical Transactions of the Royal Society of London A: Mathematical, Physical and Engineering Sciences*, 369(1939):1137–1155, 2011.

[34] M. Trupke, J. Goldwin, B. Darquié, G. Dutier, S. Eriksson, J. Ashmore, and E. A. Hinds. Atom detection and photon production in a scalable, open, optical microcavity. *Physical Review Letters*, 99:063601, 2007.

[35] J. Bochmann, M. Mücke, G. Langfahl-Klabes, C. Erbel, B. Weber, H. P. Specht, D. L. Moehring, and G. Rempe. Fast excitation and photon emission of a single-atom-cavity system. *Physical Review Letters*, 101:223601, 2008.

[36] S. Haroche. Nobel lecture: Controlling photons in a box and exploring the quantum to classical boundary. *Reviews of Modern Physics*, 85:1083–1102, 2013.

[37] E. Hanamura, Y. Kawabe, and A. Yamanaka. *Quantum Nonlinear Optics*. Springer, Berlin, 2007.

[38] R. W. Boyd and D. J. Gauthier. Slow and fast light. In E. Wolf, editor, *Progress in Optics*, volume 43, chapter 6, pages 497–530. Elsevier, 2002.

[39] M. D. Stenner, D. J. Gauthier, and M. A. Neifeld. The speed of information in a fast-light optical medium. *Nature*, 425:695–698, 2003.

[40] A. Sommerfeld. Über die Fortpflanzung des Lichtes in dispergierenden Medien. *Annalen der Physik*, 349(10):177–202, 1914.

[41] L. Brillouin. Über die Fortpflanzung des Lichtes in dispergierenden Medien. *Annalen der Physik*, 349(10):203–240, 1914.

[42] E. Figueroa, F. Vewinger, J. Appel, and A. I. Lvovsky. Decoherence of electromagnetically induced transparency in atomic vapor. *Optics Letters*, 31(17):2625–2627, 2006.

[43] M. O. Scully and S. M. Zubairy. *Quantum Optics*. Cambridge University Press, Cambridge, 1997.

[44] H. Carmichael. *An Open System Approach to Quantum Optics*. Springer, Berlin, 1993.

[45] A. Pitchford, C. Grenade, A. Grimsmo, R. Johansson, and P. Nation. Qutip python module, *http://qutip.org*, 2013.

[46] T.W. Hänsch and A.L. Schawlow. Cooling of gases by laser radiation. *Optics Communications*, 13(1):68 – 69, 1975.

[47] D. J. Wineland and Wayne M. Itano. Laser cooling of atoms. *Physical Review A*, 20:1521–1540, 1979.

[48] J. Prodan, A. Migdall, W. D. Phillips, I. So, H. Metcalf, and J. Dalibard. Stopping atoms with laser light. *Physical Review Letters*, 54:992–995, 1985.

[49] V. I. Balykin, V. S. Letokhov, V. G. Minogin, Yu. V. Rozhdestvensky, and A. I. Sidorov. Radiative collimation of atomic beams through two-dimensional cooling of atoms by laser-radiation pressure. *Journal of the Optical Society of America B*, 2(11):1776–1783, 1985.

[50] S. Chu, L. Hollberg, J. E. Bjorkholm, A. Cable, and A. Ashkin. Three-dimensional viscous confinement and cooling of atoms by resinance radiation pressure. *Physical Review Letters*, 55, 1985.

[51] C. J. Foot. *Atomic Physics*. Oxford University Press, Oxford, 2005.

[52] H. J. Metcalf and P. van der Straten. *Laser Cooling and Trapping*. Springer, 1999.

[53] E. L. Raab, M. Prentiss, A. Cable, St. Chu, and D. E. Pritchard. Trapping of neutral sodium atoms with radiation pressure. *Physical Review Letters*, 59:2631–2634, 1987.

[54] S. Chu. Nobel lecture: The manipulation of neutral particles. *Reviews of Modern Physics*, 70:685–706, 1998.

[55] C. N. Cohen-Tannoudji. Nobel lecture: Manipulating atoms with photons. *Reviews of Modern Physics*, 70:707–719, 1998.

[56] W. D. Phillips. Nobel lecture: Laser cooling and trapping of neutral atoms. *Reviews of Modern Physics*, 70:721–741, 1998.

[57] K. Dieckmann, R. J. C. Spreeuw, M. Weidemüller, and J. T. M. Walraven. Two-dimensional magneto-optical trap as a source of slow atoms. *Physical Review A*, 58:3891–3895, 1998.

[58] H. Wang, P. L. Gould, and W. C. Stwalley. Long-range interaction of the $^{39}$K(4s)+ $^{39}$K(4p) asymptote by photoassociative spectroscopy. *Journal of Chemical Physics*, 106:7899, 1999.

[59] L. Mudarikwa. *Cold atoms in a ring cavity*. PhD thesis, University of Birmingham, 2015.

[60] K. Pahwa. *Magneto optical trapping of potassium-39 in a ring cavity*. PhD thesis, University of Birmingham, 2014.

[61] K. Pahwa, L. Mudarikwa, and J. Goldwin. Polarization spectroscopy and magnetically-induced dichroism of the potassium D2 lines. *Optics Express*, 20(16):17456–17466, 2012.

[62] G. Ritt, G. Cennini, C. Geckeler, and M. Weitz. Laser frequency offset locking using a side of filter technique. *Applied Physics B*, 79(3):363–365, 2004.

[63] C. Fort, A. Bambini, L. Cacciapuoti, F.S. Cataliotti, M. Prevedelli, G.M. Tino, and M. Inguscio. Cooling mechanisms in potassium magneto-optical traps. *The European Physical Journal D - Atomic, Molecular, Optical and Plasma Physics*, 3(2):113–118, 1998.

[64] J. H. Moore. *Building Scientific Apparatus*. Cambridge University Press, Cambridge, 2009.

[65] D. J. Hucknall and A. Morris. *Vacuum Technology: Calculations in Chemistry.* Royal Society of Chemistry, 2003.

[66] S. Zhang, J. F. Chen, C. Liu, S. Zhou, M. Loy, G. Wong, and S. Du. A dark-line two-dimensional magneto-optical trap of $^{85}$Rb atoms with high optical depth. *Review of Scientific Instruments*, 83(7), 2012.

[67] O. Chubar, P. Elleaume, and J. Chavanne. ESRF Radia software, 1997. *http://www.esrf.eu/Accelerators/Groups/InsertionDevices/Software/Radia.*

[68] R. Loudon. *The Quantum Theory of Light.* Oxford University Press, 1983.

[69] R. Sylvester Williamson III. *Magneto-optical trapping of potassium atoms.* PhD thesis, University of Wisconsin-Madison, 1997.

[70] J. Catani, P. Maioli, L. De Sarlo, F. Minardi, and M. Inguscio. Intense slow beams of bosonic potassium isotopes. *Physical Review A*, 73:033415, 2006.

[71] T. Opdam. Magneto-optical trap of $^{39}$K: setup and characterisation. Master's thesis, Faculteit der Natuurwetenschappen, Wiskunde en Informatica van der Waals-Zeeman Instituut, Universiteit van Amsterdam, 2012.

[72] T. Uehlinger. A 2D magneto-optical trap as a high-flux source of cold potassium atoms. Master's thesis, Institute for Quantum Electronics, Swiss Federal Institute of Technology Zurich, 2008.

[73] W. Müssel. Characterization of a two-dimensional mot for $^{39}$K. Master's thesis, Kirchhoff Institute for Physics, Heidelberg University, 2011.

[74] L. Russell, R. Kumar, V.B. Tiwari, and S. Nic Chormaic. Measurements on release–recapture of cold $^{85}$Rb atoms using an optical nanofibre in a magneto-optical trap. *Optics Communications*, 309:313–317, 2013.

[75] N. Ramsey. *Molecular Beams.* Oxford University Press, Oxford, 1956.

[76] S. Pradhan and B. N. Jagatap. Measurement of temperature of laser cooled atoms by one-dimensional expansion in a magneto-optical trap. *Review of Scientific Instruments*, 79(1):013101, 2008.

[77] B. S. Marangoni, C. R. Menegatti, and L. G. Marcassa. Loading a $^{39}$K crossed optical dipole trap from a magneto-optical trap. *Journal of Physics B: Atomic, Molecular and Optical Physics*, 45(17):175301, 2012.

[78] V. Gokhroo, G. Rajalakshmi, R. Kollengode Easwaran, and C. S. Unnikrishnan. Sub-Doppler deep-cooled bosonic and fermionic isotopes of potassium in a compact 2D and 3D mot set-up. *Journal of Physics B: Atomic, Molecular and Optical Physics*, 44(11):115307, 2011.

[79] D. A. Steck. Quantum and atom optics (lecture course notes). *http://atomoptics-nas.uoregon.edu/ dsteck/teaching/quantum-optics*, 2015.

[80] A. Yariv. *Optical Electronics*. Holt McDougal, 1984.

[81] W. Nagourney. *Quantum Electronics for Atomic Physicists*. Oxford University Press, 2010.

[82] M. Möller, L. M. Hoffer, G. L. Lippi, T. Ackemann, A. Gahl, and W. Lange. Fabry-Pérot and ring cavity configurations and transverse optical patterns. *Journal of Modern Optics*, 45(9):1913–1926, 1998.

[83] A. E. Siegmann. *Lasers*. University Science Books, 1990.

[84] A. Ogura. Classical and quantum ABCD -transformations and the propagation of coherent and gaussian beams. *Journal of Physics B: Atomic, Molecular and Optical Physics*, 42(14):145504, 2009.

[85] E. Hecht. *Optics*. Addison-Wesley, 2001.

[86] A. Burchianti, A. Bogi, C. Marinelli, E. Mariotti, and L. Moi. Light-induced atomic desorption and related phenomena. *Physica Scripta*, 2009(T135):014012, 2009.

[87] Y. K. Yong, T. Lu, and D. C. Handley. Review of circular flexure hinge design equations and derivation of empirical formulations. *Precision Engineering*, 32(2):63 – 70, 2008.

[88] R. W. P. Drever, J. L. Hall, F. V. Kowalski, J. Hough, G. M. Ford, A. J. Munley, and H. Ward. Laser phase and frequency stabilization using an optical resonator. *Applied Physics B*, 31(2):97–105, 1983.

[89] E. D. Black. An introduction to Pound–Drever–Hall laser frequency stabilization. *American Journal of Physics*, 69(1):79–87, 2001.

[90] D. Budker, S. M. Rochester, and V. V. Yashchuk. Obtaining frequency markers of variable separation with a spherical mirror Fabry-Perot interferometer. *Review of Scientific Instruments*, 71:2984, 2000.

[91] A. O'Keefe and D. A. G. Deacon. Cavity ring-down optical spectrometer for absorption measurements using pulsed laser sources. *Review of Scientific Instruments*, 59(12):2544–2551, 1988.

[92] R. T. Jongma, M. G. H. Boogaarts, I. Holleman, and G. Meijer. Trace gas detection with cavity ring down spectroscopy. *Review of Scientific Instruments*, 66(4):2821–2828, 1995.

[93] J. Kenner. *Atoms in Microcavities: Detection and Spectroscopy.* PhD thesis, Imperial College London, 2010.

[94] M. Trupke. *Microcavities for atom chips.* PhD thesis, Imperial College London, 2008.

[95] E. Arimondo, M. Inguscio, and P. Violino. Experimental determinations of the hyperfine structure in the alkali atoms. *Reviews of Modern Physics*, 49:31–75, 1977.

[96] H. J. Carmichael and B. C. Sanders. Multiatom effects in cavity qed with atomic beams. *Physical Review A*, 60:2497–2504, 1999.

[97] L. Hilico, C. Fabre, and E. Giacobino. Operation of a "cold-atom laser" in a magneto-optical trap. *Europhysics Letters*, 18(8):685, 1992.

[98] T. Lauprêtre, C. Proux, R. Ghosh, S. Schwartz, F. Goldfarb, and F. Bretenaker. Photon lifetime in a cavity containing a slow-light medium. *Optics Letters*, 36:1551–1553, 2011.

[99] M. Landini, S. Roy, L. Carcagní, D. Trypogeorgos, M. Fattori, M. Inguscio, and G. Modugno. Sub-doppler laser cooling of potassium atoms. *Physical Review A*, 84:043432, 2011.

[100] D. Nath, R. K. Easwaran, G. Rajalakshmi, and C. S. Unnikrishnan. Quantum-interference-enhanced deep sub-doppler cooling of $^{39}$K atoms in gray molasses. *Physical Review A*, 88:053407, 2013.

[101] G. Salomon, L. Fouche, P. Wang, A. Aspect, P. Bouyer, and T. Bourdel. Gray-molasses cooling of $^{39}$K to a high phase-space density. *Europhysics Letters*, 104(6):63002, 2013.

[102] W. Yang, A. Joshi, and M. Xiao. Enhancement of the cavity ringdown effect based on electromagnetically induced transparency. *Optics Letters*, 29(18):2133–2135, 2004.

[103] T. Lauprêtre, S. Schwartz, R. Ghosh, I. Carusotto, F. Goldfarb, and F. Bretenaker. Anomalous ring-down effects and breakdown of the decay rate concept in optical cavities with negative group delay. *New Journal of Physics*, 14(4):043012, 2012.

[104] C. Billington, P. Starkey, S. Johnstone, M. Jasperse, and R. Anderson. Labscript suite, *http://labscriptsuite.org*, 2014.